THE STRUCTURE AND EVOLUTION OF DARK MATTER HALOS AND THEIR IMPLICATIONS FOR COSMOLOGY

BY

SUSMITA ADHIKARI

DISSERTATION

Submitted in partial fulfillment of the requirements
for the degree of Doctor of Philosophy in Astronomy
in the Graduate College of the
University of Illinois at Urbana-Champaign, 2017

Urbana, Illinois

Doctoral Committee:

Assistant Professor Neal Dalal, Chair and Director of Research
Professor Paul Ricker
Professor Brian Fields
Assistant Professor Joaquin Vieira

Abstract

This is a study of how the properties of dark matter halos can be used to probe fundamental questions in cosmology. Similar to the inner regions of a halo the outer density profiles of the dark matter halo carry a wealth of information regarding its formation epoch, accretion history and environment. I study how the splashback feature, which is a steepening of the slope of the density profile in a narrow, localized region near the outskirts of the halo, is in reality a powerful physical length scale within the halo that naturally demarcates the actual boundary of its virialized region. This feature can also be used to probe cosmology and fundamental physical processes like dynamical friction. Apart from the density profile I also study the shapes of halos and how to measure them using three-point galaxy statistics and finally I study the evolution of substructure in dark matter halos and its implication for galaxy evolution in clustered environments.

To my mother and father... for believing in me, always.

Acknowledgments

At the outset I would like to acknowledge those without whose support and company this journey would not have been nearly as enriching.

Fistly, I would like to thank my advisor, Neal Dalal, for his patience, constant support, and confidence in me. I was his first graduate student at the University of Illinois and greatly value his knowledge, opinion, and fervor for science and am glad to have met him during my formative years as a researcher. He has been an invaluable mentor; always available for advise and discussion from subjects ranging from research, academia, the stock market to the state of world politics. I hope to collaborate with him both personally and professionally in years to come.

Secondly, I thank Arka, my partner and fellow cosmologist, for being a constant companion, shrewd critic and a friend. I thank him for sharing the highs and lows that comprise the last few years of my life, for reminding me to look at the larger picture and never forgetting to appreciate the simple pleasures in life. I thank him for making life happier and more beautiful everyday.

Mani, Ben and Ricky for being good friends and colleagues and lightening up the long and dreary hours spent debugging unyielding codes.

I also take this opportunity to thank two wonderful scientists who were my mentors, Prof. Andrey Kravtsov and Prof. Bhuvnesh Jain, for their valuable advice both in science and career.

I would also like thank wholeheartedly the Department of Astronomy at UIUC and the support I have received from them throughout my stay in UIUC. I must especially mention

Jeri, Judy, Rebecca and Bryan for their calming presence that makes the department as welcoming as it is.

Lastly but importantly I would like to thank and acknowledge this country and its people for making this place a home away from home. Nothing creative can be accomplished in an environment that is inhospitable to diversity. I am glad to have met the beautiful people in this Department and outside that have made my stay here memorable and worthy of cherishing for a lifetime.

Table of Contents

List of Figures

Chapter 1

Introduction

Understanding the formation and evolution of dark matter halos can give us insights into some of the fundamental questions in cosmology. Dark Matter halos are the endpoints of structure formation. Quantum fluctuations in the energy density of the early universe are amplified after a period of rapid exponential expansion known as inflation. Inflation lays down a gaussian, scale-invariant spectrum of adiabatic perturbations in all the energy fields in the universe, namely, radiation, curvature and matter. The perturbations in matter grow gravitationally to collapse and form bound and virialized structures that are known as dark matter halos. These highly non-linear bound structures evolve independently of the background expansion. The average overdensity of the matter field within these halos is almost 200 times greater than the mean matter density of the universe, making them the strong gravitational potential wells within which all known structure in the universe, like galaxies, stars, solar systems, planets form and evolve.

1.1 Halo collapse and density profiles

A standard way to understand the formation of the halos is using the spherical collapse model. This model follows the evolution of a shell enclosing a top hat density perturbation in a spatially flat, matter dominated Einstein de-Sitter universe that is expanding according to the Friedmann equations given by,

$$\frac{1}{a_{bg}}\frac{da_{bg}}{dt} = H_0 a_{bg}^{-3/2}, \tag{1.1}$$

where a_{bg} is scale factor of the background universe and H_0 is the Hubble expansion factor today. The top hat density perturbation evolves independently as a closed universe with the mass enclosed within the shell surrounding the perturbation given by, $M = \frac{4\pi}{3} r_0^3 \Omega_m \rho_c$ where r_0 is the inital radius of the shell, Ω_m is the fractional matter overdensity of the closed universe. We can also write down the equation of motion of the shell. From Gauss's law, the force on shell enclosing a spherically symmetric density depends only on the mass enclosed within it and therefore,

$$\frac{d^2 r(t)}{dt^2} = -\frac{GM(< r(t))}{r(t)^2} \tag{1.2}$$

Integrating these equations, the solution in its parametric form is given by,

$$R = A(1 - \cos\theta) \tag{1.3}$$

$$t = B(\theta - \sin\theta) \tag{1.4}$$

$$A^3 = GMB^2 \tag{1.5}$$

where θ is called the developmental angle that goes from 0 to 2π and is related to the scaled conformal time η by $\theta = H_0 \eta (\Omega_m - 1)^{1/2}$. Equations 1.3 and 1.4 define a cycloid. The Fig 1.1 shows the solution of the spherical collapse model. The figure demonstrates that initially the perturbation expands with the Hubble flow, after some time it detaches from the Hubble flow and begins to deviate significantly. At $\theta \to 0$ the leading order terms of the solution give, $r(\theta \to 0) = A\theta^2/2$ and $t(\theta \to 0) = B\theta^3/6$, rearranging this we get a relation between r and t as $r(t) = A/2(6t^2/B)^{1/3}$. Therefore, initially $r \propto t^{2/3}$, which is similar to the evolution of a matter dominated universe with $\Omega_m = 1$.

We can expand the solutions to higher order to follow the evolution further,

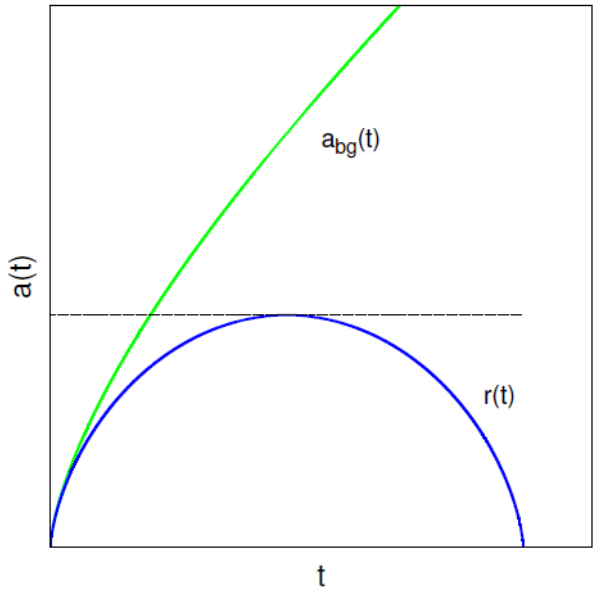

Figure 1.1: The solution of the spherical collapse model in a matter dominated universe. The Blue curve shows the evolution of the background universe and the green curve shows the evolution of a shell enclosing a top hat density perturbation.

$$r(\theta) = A\left[\frac{\theta^2}{2} - \frac{\theta^4}{24}\right] \tag{1.6}$$

$$t(\theta) = B\left[\frac{\theta^3}{6} - \frac{\theta^6}{120}\right] \tag{1.7}$$

$$A^3 = GMB^2 \tag{1.8}$$

Manipulating these equations by reiterating solutions for r and t, we get

$$r(t) = \frac{1}{2}(6t)^{2/3}(GM)^{1/3}\left[1 - \frac{1}{20}\left(\frac{6t}{B}\right)^{2/3}\right] \tag{1.9}$$

The initial mass of the system is given by, $M_f = 4\pi/3\ r_0^3\ \bar{\rho_m}$, spherical collapse conserves the mass inside the shell and therefore if the overdensity increases by an amount δ, the radius must have shrinked by an amount Δr. giving $M_f = 4\pi/3 r_0^3 \bar{\rho_m}(1+\delta)(1+\Delta r)^3$. Equating the two masses we get $(1+\delta)(1+\Delta r)^3 = 1$. Taylor expanding to find δ in terms of Δr and substituting the expression of Δr from eqn 1.9 we find that the overdensity at a given time

t is given by,

$$\delta = -3\Delta r = \frac{3}{20}\left(\frac{6t}{B}\right)^{2/3} \tag{1.10}$$

Describing some of the key epochs of evolution using eqn.1.10, turnaround occurs when $\theta = \pi$, $t = \pi B$ and collapse occurs when $\theta = 2\pi$ and $t = 2\pi B$ giving,

$$\delta_{turnaround} = 1.06 \tag{1.11}$$

$$\delta_{collapse} = 1.69 \tag{1.12}$$

In this simple model collapse is homologous, there is no shell crossing, all shells collapse at the same time creating an infinite overdensity at collapse. In reality however, the shells never proceed to collapse to 0 radius. Nearby structure imparts angular momentum to the shells that will cause the particles to avoid the singularity at 0, processes like dynamical friction eventually leads to equipartition of energy resulting in a pressure supported halo. Energy arguments can help us evaluate the non-linear overdensity at this epoch which is known as "virialization".

Virial theorem tells us that the final equilibrium state of a system has energy such that $U = -2T$, where U is the potential energy and T is the kinetic energy. At turnaround the kinetic energy of a shell is 0. Therefore invoking the virial theorem along with conservation of energy we find $U(r_{ta}) = U(r_{vir})/2$. Since $U \propto r^{-1}$, $r_{vir} = r_{max}/2$ and $\theta_{vir} = 3\pi/2$. Therefore the overdensity at virialization can be evaluated giving,

$$\Delta_v = \frac{\rho_m(\theta = 3\pi/2)}{\bar{\rho}(\theta = 2\pi)} = 18\pi^2 = 178 \tag{1.13}$$

Although simple in its construction the spherical collapse model is a powerful intuitive tool. One of the key insights obtained from this model is the fact that the overdensity at

virialization is independent of the initial size and amplitude of the density perturbation. A shell is said to have "collapsed" when the overdensity within it reaches about 200 times the background matter density. This overdensity is therefore abundantly used in literature to define the boundary of a halo. A halo is defined as the interior of the radius enclosing a matter overdensity of $\Delta_{vir} = 200$.

In reality however some of the assumptions of the spherical collapse model break down. It is rare to find a top hat, spherical density perturbation. Moreover the halos are not formed by a monolithic collapse of a density perturbation independent of its local environment. During formation their rate of collapse is affected by tidal forces from nearby structure which intimately depends on the shape of the density perturbation itself. Also, once shells of particles collapse into the halo and begin to orbit in its potential they start crossing each other as a result of which the mass inside them does not remain constant. The halo potential grows with time as more matter is accreted on to the halo. The spherical collapse model predicts that virialization occurs at half the turnaround radius, in N-body simulations it has been found that this is often not the case. Objects orbiting in the halo can extend anywhere from 0.4-0.9 r_{ta} [6, 7], therefore matter near the virial overdensity of 178 has not usually undergone a collapse by a factor of 2 as predicted by the spherical collapse model. As spherical overdensities are easy to measure, the conventional definitions of halo use the spherical collapse model, while in a matter dominated universe this overdensity is $178\rho_m$, in a cosmological constant dominated universe this is closer to $300\rho_m$. However, as we will see these definitions of boundaries may often underestimate the mass, and in some cases even overestimate it.

In general the growth of structure in the universe is hierarchical. In the power spectrum of perturbations laid down by inflation, the smallest wavelengths collapse first forming the smallest halos. Larger structures form subsequently either by accreting these small halos, merging with pre-existing similar mass halos (major mergers) and by accreting diffuse dark matter, i.e dark matter that hasn't been part of any other structure. Halos typically form

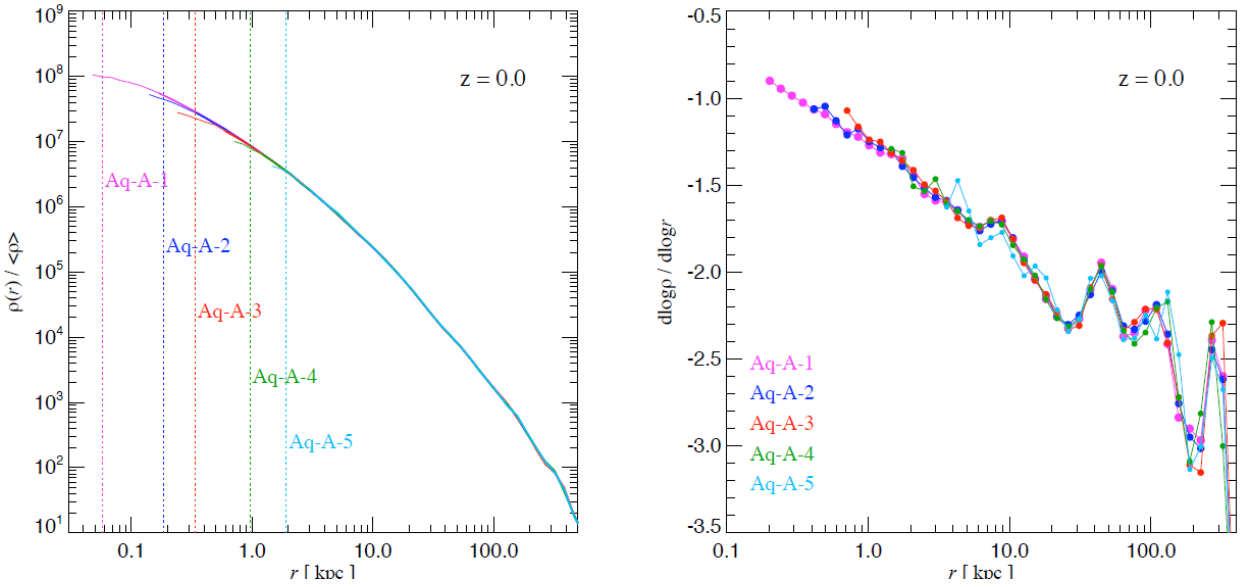

Figure 1.2: Left panel shows the NFW density profile of dark matter halos in the aquarius simulations. The right panel shows the logarithmic slope of the local density. [1]

with a strongly bound core at first and then eventually accrete loosely bound matter in the outskirts. The complete mixing of old and new material occurs rarely and only in the case of major mergers. This is known as inside out formation. For Gaussian initial conditions where the spectrum of perturbations increases monotonically, such hierarchical growth is natural.

Due to the complicated nature of halo formation, dark matter halos have been studied extensively in simulations. The purely gravtiational interaction of dark matter particles is studied with the N-body interaction methods. Modern high resolution simulations, that have mass resolutions down to $10^5 M_\odot h^{-1}$ have been used to gain a statistical understanding of the growth and structure of halos themselves in addition to the statistics of halo mergers, formation times and their spatial distributions.

One of the most remarkable findings in simulations of dark matter halos was that their density profiles are nearly universal and are well explained by the NFW fitting (Fig 1.2). This is basically a two parameter density model, which is composed of two broken power laws. In the inner regions of the halo the density profile has a slope of -1 and as we move outwards the slope rolls over to -3. The expression for the density at a given radius r is,

$$\rho(r) = \frac{\rho_s}{\frac{r}{r_s}\left(1+\frac{r}{r_s}\right)^2} \quad , \tag{1.14}$$

here r_s and ρ_s are known as the scale radius and scale density respectively and are simply related to the radius, r_{-2}, and density, ρ_{-2}, where the slope of the density profile is -2. The total mass of the halo is defined to be the virial mass. And the concentration of the halo is defined as the ratio of the scale radius to the virial radius, i.e. $c_{vir} = r_{vir}/r_s$. The concentration is a measure of how quickly the slope of the density profile rolls over from -1 to -3.

Many attempts have been made to study and analyze this apparent universality of the dark matter halo density profile [8, 9, 10, 11, 12, 13]. Even though halo formation is an apparently complicated and violent process the final profiles of dark matter halos are strikingly similar. In reality NFW like profiles are known to arise even in the absence of complicated hierarchical structure formation. Calculations of smooth, monolithic collapse of halos also predict NFW like profiles [14] moreover in cosmologies with hot dark matter where there is very little or no substructure the same final profiles are recovered given there is a sharp cut off in the power spectrum at small scales[15] .

It must be noted however that universal density profiles are not a generic outcome of cold, dissipationless, gravitational collapse of a density perturbation in an expanding universe. [2, 16, 3] study self-simiar collapse of scale-free density perturbations described by a power law profile in an expanding universe. They find that the final profile of the halo is not universal but depends on the index of the power-law of the of the initial perturbation profile. Triaxial collapse produces inner cusps whose shapes again depend on the slope of the initial perturbation. However based on some simple arguments which are explained in [8] it can be shown that as halo growth slows down, the outer profiles of halos naturally approaches $\rho \propto r^{-3}$.

Let us consider a spherical overdensity in the early universe with a powerlaw radial

profile for the average enclosed density within a shell given by $\delta(r_L) \propto r_L^{-\gamma}$, where r_L is the Lagrangian radius of the shell. At early times in a matter dominated universe the density perturbation grows as the linear growth factor, $D(a) \propto a$. At any time the enclosed overdensity profile is therefore given by, $\delta \equiv \delta(r_L, a) \propto a r_L^{-\gamma}$. From sphercical collapse a shell turnaround is said to occur when the linear over density, $\delta \sim 1$. Therefore at a given time the Lagrangian scale that is turning around has $r_L \propto a^{1/\gamma}$. The physical scale associated with turn around at a is given by $r \propto a r_L \propto a^{1+1/\gamma}$.

Let us now also suppose the halo is accreting mass at a constant rate which is given by $M \propto a^s$, where s is defined as the accretion rate of the halo. At any time the mass enclosed within a Lagrangian radius is $M \propto r_L^3$. Therefore the shell that is turning around at scale factor a has $M \propto a^{3/\gamma} \propto a^s$. Hence the mass accretion rate and the slope of the density profile are related as $s = 3/\gamma$, implying that a steep initial profile leads to a slow growth where as a shallow initial density profile leads to fast accretion. This simple argument explains why concentration of the halo density profile is correlated with the formation time or age of a halo, as can be seen the shape of the halo profile determines how fast it will grow.

Further to understand how the initial density profile effects the shape of the final profile, let us consider that we freeze the shells in their positions post turn around and artificially stop shell crossing. The distribution of turn around radii is simply given by,

$$r \propto r_L^{1+\frac{1}{\gamma}} \propto r_L^{\frac{3+s}{s}} \propto M^{\frac{3+s}{3s}} \tag{1.15}$$

therefore the mass $M \propto r^{\frac{3s}{3+s}}$. The density profile can now be evaluated giving,

$$\rho(r) = 4\pi r^2 \frac{dM}{dr} \propto r^{-\frac{9}{3+s}} \propto r^{-\frac{3\gamma}{1+\gamma}} \tag{1.16}$$

This slope of the density profile,s $g = -3\gamma/(1+\gamma)$ is known as the Fillmore Goldreich slope which arises from the self-similar collapse of power law density perturbations. If $\gamma \sim 0$, i.e

the initial perturbation is shallow the final slope is also shallow. On the other hand if $\gamma \infty$ or alternatively if the accretion rate $s = 3/\gamma \to 0$, the final collapsed slope of the density profile approaches -3. This explains some of the behavior of dark matter halos. If halo growth stops or slows down with time, the outer slope of the density profiles naturally approach -3 as is seen in NFW profiles. Infact as time goes forward the r^{-3} region of the halo simply expands.

To get the complete picture of halo formation one must extend beyond the frozen approximation and follow the orbits of individual shells. It can be shown that for a spherical potential, each shell lays down a time averaged density profile which is nearly isothermal inside of its apocenter. The final collapsed profile of the dark matter halo can be thought of as the sum of these indivdual shell profiles. Considering smooth spherical accretion onto the halo, as the mass of the halo grows by accumulating matter around itsel each shell responds to the slowly changing potential adiabatically. In other words the shells contract conservinig the adiabatic invariants which in this case is given by the product Mr, where M is the mass enclosed within the shell at radius r. The profile of adiabatic invariants is set by the initial density perturbation and it is elegantly shown in [8] that the final profile of halos derived under these assumptions closely resemble those found in N-body simulations.

The NFW profile has been largely successful in fitting most halos formed in N-body simulation. It should however be noted that it has been seen that the NFW is a better fit to halos that are of low mass. The density profile of large cluster sized halos are often better approximated by isothermal profiles in their outskirts.

Dark matter halo profiles not only tells us about the gravitational field within which galaxies form and evolve it also tells us about the history and evolution of the universe in general. The shape or concentration of the halo profile is related to the accretion rate of the halo, which in turn is related to the formation time of a halo and its local environment. The post collapse density profile inside the halo and in it's immediate neighbourhood can arguably be derived from the pre collapse initial density perturbations. Therefore measuring

profiles of dark matter halos today can also act as a probes to study the nature of fluctuations in the initial density field.

Understanding the shape and structure of dark matter halos has been the focus of my dissertation. One aspect of halo formation that had previously received somewhat less attention were the density caustics that form during halo formation. As shells of matter turn around in their orbits at their apocenters their radial velocities approach 0 as a result of which subsequent shells of matter pile up against each other forming density caustic. These are basically narrow, localized regions of enhanced densities. The outer most density caustic in a dark matter halo corresponds to the first apocenter after infall of a shell into the halo potenitial and acts as the boundary of the virialized region of the halo. This is a characteristic scale inside a halo beyond which there is only the infall stream. The outskirts of the halo and their implications for cosmology have been the focus of my study during these past few years. The following 2 chapters of this document elaborate on this very subject.

1.2 Shapes of dark matter halos

Dark matter halos are in general not spherical. Halos in N-body simulations are known to be triaxial. They are usually prolate with the average axis ratios of the longest to the shortest axis close to 2:1. Typically high mass halos are more spherical than low mass ones that are of the order of the milky way halo mass, $10^{12} M_{\odot} h^{-1}$, and halos also tend to be slightly more aspherical in the inner regions compared to the outskirts [17, 18]. The mean angle between the major axis of the inner and outer region is close to 20° with a fairly large scatter. The final shape of the collapsed halo is effected by several factors, the initial density perturbation that collapses to form the halo may be triaxial itself apart from this the final asphericity of a halo also reflects its growth by large mergers, accretion of substructues which creates tidal torques disrupting smooth spherical collapse. The matter within halos end up in shells that are triaxial ellipsoids that are fairly well aligned with each other.In some cases they may also

show evidence for a slight twisting of the principal axes with radius. Halos also show strong alignments with matter well beyond the virial radius, especially high mass halos may even show alignments out to almost $10Mpc\ h^{-1}$. As cold dark matter is dissipationless it can retain signatures of anisotropy during its formation. However, alternative models of DM like self interacting dark matter or warm dark matter, where particles can dissipate momentum through non-gravitational interactions, or MOND theories which do not invoke particle dark matter are known to produce halos that are rounder. Therefore measuring the shapes of dark matter halos can help probe the fundamental nature of dark matter itself.

Weak gravitational lensing is a powerful tool to study the structure of halos. Two point cross-correlations between foreground galaxies and the tangential shear in galaxies behind them give high precision measurements of the radial profile of halos. Inferring the shape of galactic halos, however, requires measuring the shear as a function of angle from the principal axes of the halo. One of the challenges to measure the angular dependence of shear is the fact that we do not, a priori, know the orientation of halos in the sky, the general practice has been to measure shear as function of the angle from the principal axis of the galaxy light profile. However, in simulations galaxy halo misalignments of the order of $\sim 38^{\circ}$ are quite typical, complicating the interpretation of these measurements. In [19] we propose a novel method to measure halo anisotropy independent of galaxy-halo misalignment, using the lens-shear-shear three-point correlation functions. As our method provides an independent way to measure ellipticities, combined with the two-point galaxy-shear correlation function, it can also be used to measure the average degree of galaxy-halo misalignments. Large scale imaging surveys are making higher order correlations measurable. We show that current and ongoing imaging surveys like DES, PanSTARRS and HSC can detect halo ellipticities at 2σ level, while future surveys like LSST should have sufficient sensitivity for a significant ($> 3\sigma$) detection.

1.3 Halo substructure and galaxies

While N-body simulations are an excellent tools to study the growth of structure and evolution of the universe, in reality we cannot "see" dark matter or the collapsed structures they form. We can only infer their existence and properties with their gravitational interaction with the baryonic content of the universe either by gravitational lensing or from the clustering and dynamics of galaxies in the sky. Following recombination when baryons and photons decouple from each other baryons begin to fall into the potential wells of dark matter halos and condense dissipatively to form galaxies in the central region of these halos. Isolated halos along with their central galaxies are often accreted on to larger structures in their vicinity and reside in their potential as subhalos. As mentioned previously cold dark matter halos are not smooth and hierarchical structure formation predicts an abundance of such substructure. Significant fraction of a halo's mass is tied up in the form of subhalos. Prior to infall these subhalos have NFW-like profiles. However once they fall in to their host, processes like tidal stripping alter their profiles and they are less likely to resemble halos in the field. '

Just like diffuse dark matter particles subhalos are tracers of the gravitational potential of the host dark matter halo. Therefore apart from from gravitational lensing which is a direct probe of the matter density in the universe the dynamics and spatial distribution of galaxies that reside in these subhalos help us probe the large scale structure of the halo. Part of my dissertation has been to study the behaviour of subhalos to probe fundamental physical processes like dynamical friction and to understand the galaxy evolution in cluster environments.

Recently More et al. detected the aforementioned splashback feature in the projected number density profile of galaxies around in clusters identified in the SDSS galaxy survey using the RedMaPPer algorithm. Unlike diffuse dark matter particles massive structures experience extra forces due to dynamical friction, therefore their splashback position, which

is the position of the first apocenter after accretion on to a halo, should depend on the ratio of the subhalo mass to the halo mass. The decceleration due to friction makes massive objects moving in an ambient field of diffuse matter lose energy and the timescales for such effects depend on the ratio of the subhalo to the host halo mass. In [20] we for the first time see direct evidence for dynamical friction in action in galaxy clusters. We find that the splashback radius for subhalos shrinks as a function of their mass. This is the subject of chapter 3.

Currently we are also looking at the correlation between galaxy colors and clustering. It has been known that galaxies that reside in clustered environment tend to be red with quenched star formation. Large over densities therefore somehow suppress star formation. Two competing theories try to explain the increased red fraction in galaxy clusters, the first claims that intracluster astrophysical processes strip gas off galaxies rendering them quenched and the other say that galaxies that reside in clusters are simply older and therefore if all galaxies turn off starformation at some point in their evolution we can reproduce the observed statistics of quenched galaxies. In Chapter 6 I discuss an independent probe to test the two theories based on satellite kinematics.

Chapter 2

Splashback in accreting dark matter halos

Recent work has shown that density profiles in the outskirts of dark matter halos can become extremely steep over a narrow range of radius. This behavior is produced by splashback material on its first apocentric passage after accretion. We show that the location of this splashback feature may be understood quite simply, from first principles. We present a simple model, based on spherical collapse, that accurately predicts the location of splashback without any free parameters. The important quantities that determine the splashback radius are accretion rate and redshift. [1]

2.1 Introduction

The structure of dark matter halos has attracted both theoretical and observational interest over several decades. Beginning with the pioneering work of [21], numerous papers have investigated the formation of bound virialized structures that gravitationally collapse in an expanding universe. A key breakthrough was provided by [2], who studied the self-similar collapse of scale-free perturbations, and identified several key physical processes that determine halo profiles. As numerical simulations of halo formation have progressed [22, 23, 24, 25], producing increasingly precise calculations of halo structure, the ideas presented in [2] have proven fundamental towards understanding the simulation results [3, 8].

Much of this theoretical work has focused on the interior structure of halos, while the

[1] This chapter was previously published in the Journal of Cosmology and Astroparticle Physics as S. Adhikari, N. Dalal and R. T. Chamberlain, Splashback in accreting dark matter halos, Journal of Cosmology and Astroparticle Physics 11 (Nov., 2014) 019, [1409.4482].This chapter matches the published version.

outer profiles of halos have received somewhat less attention. Recently, however, [26] studied the outskirts of simulated halos and discovered that the outer density profiles of halos exhibit steep logarithmic slopes, $d(\log\rho)/d(\log r) \lesssim -4$, over a narrow range of radii. This behavior is inconsistent with standard fitting functions used to characterize halo shapes, like the NFW profile [27, 28] or the Einasto profile [29, 30]. [26] found that the location of this sharp feature depends principally on the accretion rate $s = d(\log M)/d(\log a)$ of the halos, and they provided a fitting function for its location as a function of s.

As argued by [26], the local steepening that they observed is produced by a caustic, associated with the splashback of material that has been recently accreted by the halo. Caustics arise when the orbits of different particles pile up at similar locations, frequently near the apocenters of the orbits. For example, the spherically symmetric similarity solutions of [2] exhibit pronounced caustics. Similar features arise in 3D similarity solutions of the collapse of triaxial peaks [3], although the features are not as prominent in the spherically averaged density profile, because the caustics are not spherically symmetric in general (see §2.3). In dark matter halos from cosmological N-body simulations, the density enhancements associated with caustics are difficult to detect, not only because of triaxiality, but also because of the effects of small-scale substructure, both of which act to smear out caustics spatially [31, 32]. In real galaxies, these caustics are observed as radial shells with sharp edges [33].

As noted above, radial caustics are associated with the pileup of orbits near apoapse. The outermost caustic is associated with the first apoapse after collapse, termed splashback. Figure 2.1 illustrates that the local steepening discussed by [26] coincides with the splashback radius. The figure plots the phase space structure of the particles near dark matter halos taken from the publicly available MultiDark Simulation[2], along with the radial dependence of the local logarithmic slope of the density $d(\log\rho)/d(\log r)$. The location where $d(\log\rho)/d(\log r) < -3$ coincides with splashback, the outermost radius attained by

[2] http://www.multidark.org/MultiDark

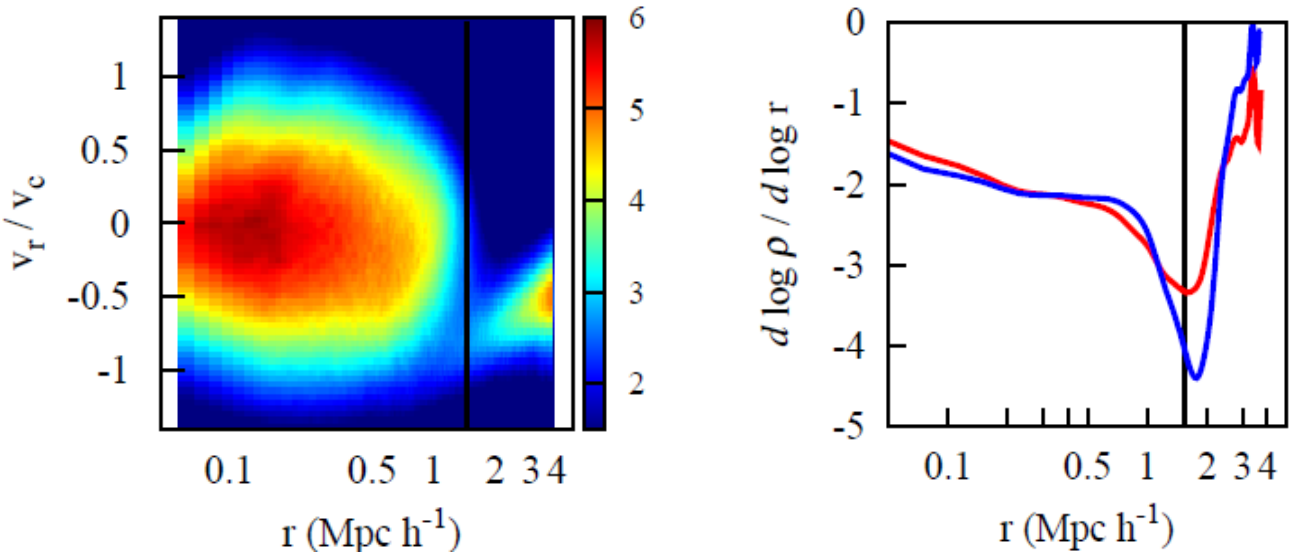

Figure 2.1: Top: The phase space diagram for halos from the MDR1 simulation in the mass range $M = 1-4\times10^{14}h^{-1}M_{\odot}$. The colorbar shows the number of particles within each phase space pixel. The pixel spacing is linear in both r and v, so the number is proportional to $r^2\rho$. Bottom: The local slope of the density of all particles (red) and particles with $|v_r| < 0.4\,v_{\rm circ}$ (blue), as a function of radius r. The location of the feature in the local slope coincides with the outer caustic at the splashback radius.

particles following their collapse into halos. As the phase-space diagram illustrates, the splashback radius is near the location of a radial caustic, where the slope of the phase space sheet becomes vertical. To further illustrate this point, the figure plots the density slope of only the particles near splashback, i.e. those with $|v_r| < 0.4\,v_{\rm circ}$. Among the particles near splashback, the steepening of the density slope becomes even more pronounced.

The steepening feature in the outer profile is therefore determined by the splashback radius of recently accreted material. Since splashback occurs only half an orbit after collapse, a relatively simple treatment of the orbital dynamics should suffice to capture the physics setting the splashback radius. In this paper, we show that this is indeed the case. We construct an extremely simple model for splashback, based largely on the spherical collapse model of [21]. We then compare the predictions of our model with N-body simulations, and

show that it accurately predicts the location of the steepening feature for a variety of halos with different mass, redshift, and accretion rate.

2.2 Toy model for splashback

As noted above, the steepening feature occurs near the splashback radius. To predict the location of this feature, we therefore must predict where splashback occurs following collapse. One estimate for the location of the splashback radius may be constructed from the spherical collapse model [21]. This model computes the nonlinear evolution of a spherical shell, assuming that the mass interior to the shell is overdense, and that the interior mass is a constant (i.e., the model neglects shell crossing). The equation of motion is therefore quite simple,

$$\ddot{r} = -\frac{GM}{r^2} + \frac{\Lambda c^2}{3} r, \tag{2.1}$$

where M is a constant. For $\Omega_M = 1$ and $\Lambda = 0$, this model predicts that turnaround occurs at the time when the linearly evolved density reaches $\delta_l \approx 1.06$, and collapse to $r = 0$ occurs at the time when $\delta_l \approx 1.69$. Once the infalling shell enters the virialized region, the assumption of constant interior mass becomes invalid. Estimating virialization as the time when $2\,\mathrm{KE} + \mathrm{PE} = \dot{r}^2 - GM/r = 0$ gives $r_{\rm vir} \approx r_{\rm ta}/2$, corresponding to a nonlinear overdensity of $\Delta_{\rm vir} = 18\pi^2$. For $\Omega_M \neq 1$, these expressions are somewhat modified [34].

Following entry into the halo, the shell begins to orbit in the halo potential. If we continue to assume spherical symmetry, then we can still use Eqn. (4.2) to compute the motion; the only change is that now the mass M interior to the shell is not constant, but instead depends on radius r and time t. The time dependence of the mass profile is determined by the accretion rate of the halo. Let us suppose that the halo mass grows as $M_{\rm tot} \propto a^s$, where $s = d(\log M_{\rm tot})/d(\log a)$. Then the halo radius scales as $R \propto a^{1+s/3}$. We

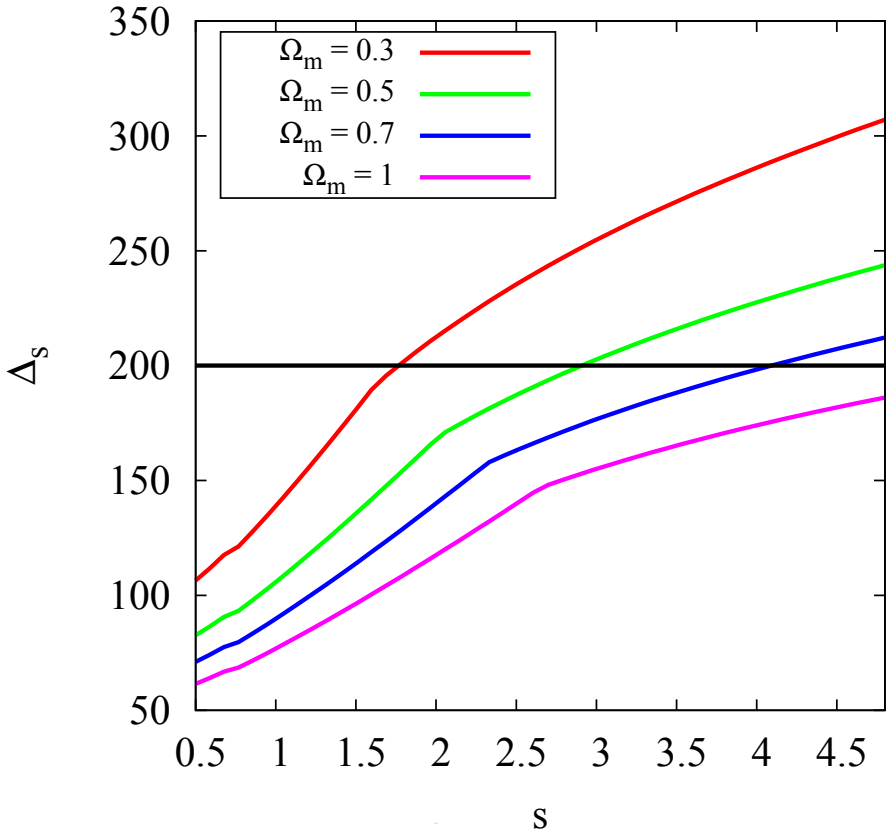

Figure 2.2: Overdensity enclosed within the splashback radius as a function of accretion rate $s = d\log M/d\log a$. Large Δ corresponds to small radius within the halo. For reference, the horizontal line at $\Delta = 200$ indicates the usual definition of the halo boundary. Halos with high accretion rate have a larger enclosed overdensity within the splashback radius than halos with low accretion rates, corresponding to a smaller splashback radius for rapidly accreting halos. Additionally, the enclosed overdensity increases as Ω_m becomes smaller, meaning that at low redshift, the splashback occurs at a smaller fraction of r_{200m}.

assume that the halo mass distribution is given by the NFW profile [28],

$$M(r) = M_{\rm tot}\frac{f_{\rm NFW}(r/r_s)}{f_{\rm NFW}(R/r_s)}, \tag{2.2}$$

where r_s is the NFW scale radius, and $f_{\rm NFW}(x) = \log(1+x) - x/(1+x)$. The NFW concentration $c \equiv R/r_s$ sets the slope of the mass profile at the halo boundary, and we choose c such that the outer slope is given by $d\log M/d\log r = 3s/(3+s)$ at $r = R$ [2, 3, 8].

Equations (4.2)-(4.16) fully specify our model. We use spherical collapse with constant

enclosed mass M until the shell radius reaches $r_i = r_{\rm ta}/2$. Thereafter, we assume the mass profile is given by Eqn. (4.16). We integrate the motion of the shell in this potential until splashback, when $\dot{r} = 0$. From the radius and time of splashback, r_s and t_s, we can determine the enclosed mass, the enclosed density, and the background mean density, allowing us to determine the enclosed overdensity inside the splashback radius, Δ_s. Our results do not strongly depend on our assumed mass profile inside the halo. For example, using an isothermal profile instead of NFW gives results that are consistent at the $\sim 10\%$ level. Figure 4.1 shows the predicted values of the enclosed overdensity. Throughout this paper, we define overdensities relative to the mean matter density, not the critical density. In our model, Δ_s depends only on the halo's accretion rate s, along with the values of the background cosmological parameters Ω_M and Ω_Λ at the time the halo is observed. The behavior we find is unsurprising. As the accretion rate is increased (larger s), the potential deepens more quickly in time, resulting in splashback occuring at a smaller radius, or equivalently, at a larger enclosed overdensity Δ_s. Similarly, at low redshift when Ω_M diminishes and Ω_Λ increases, the mean background density of the universe $\bar{\rho}_m$ decreases more during the time between turnaround and splashback, again resulting in a larger Δ_s.

Finally, although the model presented here is extremely simple to evaluate, we also provide a very rough fitting function to approximate the location of splashback:

$$\Delta_s \approx A\,\Omega_M^{-b-c\,s} e^{d\Omega_M + e\,s^{3/4}}, \tag{2.3}$$

with fitted parameters $A = 38$, $b = 0.57$, $c = 0.02$, $d = 0.2$, $e = 0.52$. This fitting function has $\sim 5\%$ accuracy over the range $0.5 < s < 4$, $0.1 < \Omega_M < 1$. The results shown in this paper do not use this fitting function, since it is equally simple to evaluate the spherical toy model.

2.3 Comparison with simulations

In this section, we compare the predictions of the toy model described in the previous section with results of numerical simulations. First, we compare our model with the similarity solutions that arise from the collapse of scale-free perturbations [2, 3]. Fig. 2.3 shows one example, for accretion rate $s = 3$. In all cases, we find good agreement between the caustic location obtained in the similarity solution and that predicted by the toy model. This even holds true for collapse of highly triaxial perturbations: the main effect of the triaxiality is to make the splashback surface nonspherical, reducing the maximal depth of the slope of the spherically averaged profile, while preserving the mean radial location of splashback.

Our toy model also predicts a significant dependence on redshift (or equivalently, a dependence on the value of Ω_M). We cannot test that prediction using similarity solutions, because they assume $\Omega_M = 1$. To test this prediction, we therefore ran 1-dimensional N-body simulations of the collapse of isolated overdensities. The simulations evolve the motion of spherical shells following Eqn. (4.2). The initial linear overdensity profiles are chosen to produce $M \propto a^s$ for various values of s. Figure 2.4 shows an example, for $s = 3$. The solid curves in the figure show the results of the 1-D simulations, while for comparison, the dashed curve shows the similarity solution for $s = 3$. Note that for $\Omega_M = 1$, the 1-D simulation does not exactly match the similarity solution. This is because the dynamics, even in spherical symmetry, are ubject to a slew of instabilities that are not present in the similarity solution [35, 36, 32]. To suppress these instabilities, we follow [32] and soften the force law in Eqn. (4.2) near $r = 0$. As Fig. 2.4 shows, the halo profile for $\Omega_M = 1$ is similar to the similarity solution. The level of agreement or disagreement between the two curves illustrates the extent to which the 1-D N-body simulations may be trusted. Note in particular that the location of the splashback radius is similar in the two cases. The figure also shows results for $\Omega_M = 0.3$, in the solid red curve. For comparison, the vertical dotted lines show the toy model's predictions for the splashback radius for these values of Ω_M. Overall, we find good

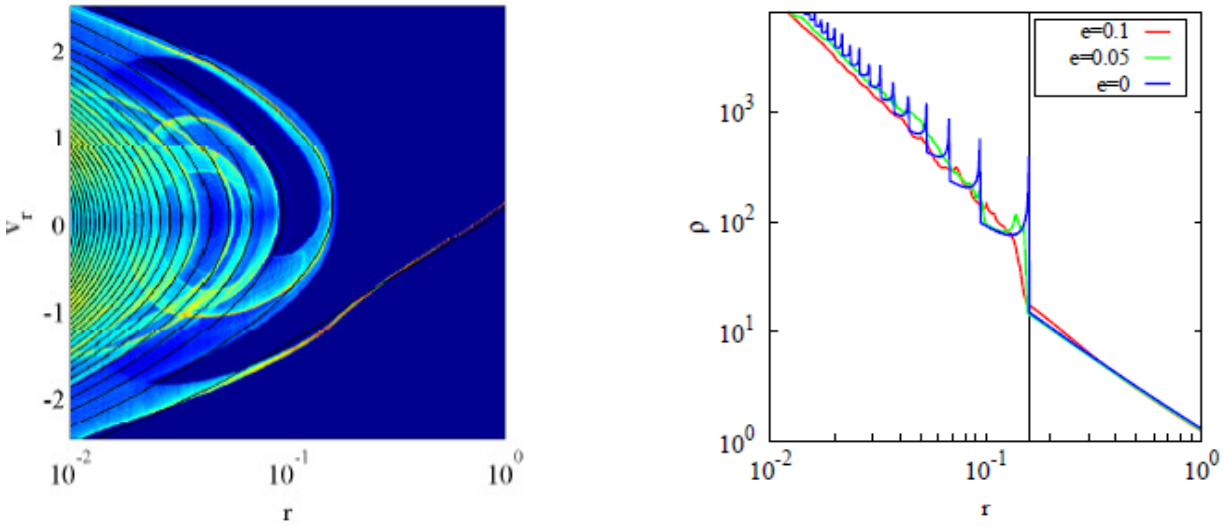

Figure 2.3: Caustics for self-similar halos [2, 3] with accretion rate $s = 3$. The top panel shows the phase space diagram for spherically symmetric collapse (solid black curve) and for 3D collapse with $e = 0.05$ (colormap), while the bottom panel shows the density vs. radius. The vertical line in the bottom panel indicates the splashback radius predicted by the spherical collapse model for this value of s. As the density profiles demonstrate, the caustic location depends mainly on accretion rate, with little if any dependence on the initial ellipticity e. However, the caustic width does depend on e, apparently because the shape of the splashback surface is related to the initial ellipticity.

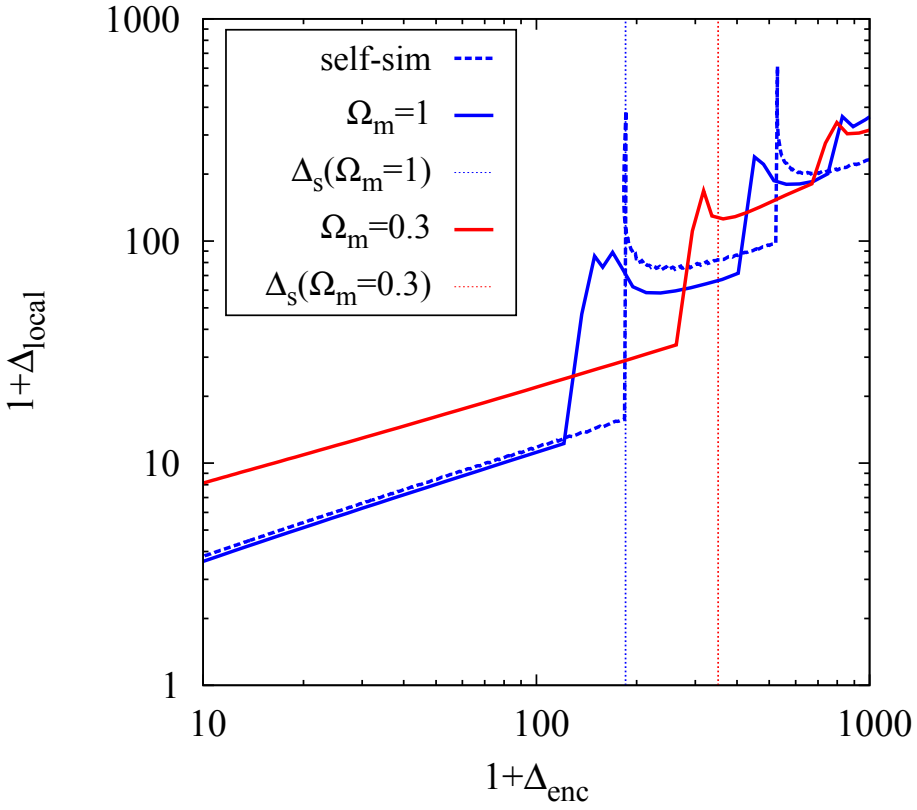

Figure 2.4: Halo profiles for 1-D spherical collapse with accretion rate $s = 3$. The x-axis shows the averaged enclosed overdensity inside each radius, while the y-axis shows the local overdensity at that radius. The blue curves correspond to $\Omega_M = 1$. The solid curve shows the profile obtained from the 1-D N-body simulation, while the dashed curve shows the similarity solution. The red curve shows the profile for $\Omega_M = 0.3$. The dotted vertical lines show the location of splashback predicted by our toy model for $\Omega_M = 1$ (blue) and $\Omega_M = 0.3$ (red) respectively.

agreement, demonstrating that the location of splashback does indeed depend on cosmology and redshift.

Finally we compare with cosmological N-body simulations from the publicly available MultiDark Database. The MDR1 simulation [37, 38] contains 2048^3 particles in a box of side length $L = 1\,h^{-1}$Gpc, giving a particle mass of $M_p = 8.7 \times 10^9 h^{-1} M_\odot$, while the Bolshoi simulation [39] contains 2048^3 particles in a box of side length $L = 250\,h^{-1}$Mpc, giving a particle mass of $M_p = 1.3 \times 10^8 h^{-1} M_\odot$. We extracted halos of mass $M_{\rm vir} \lesssim 10^{14} h^{-1} M_\odot$ from the Bolshoi simulation, and used MDR1 to obtain halos of mass $M \gtrsim 10^{14} h^{-1} M_\odot$. For both

simulations, we used the publicly available Rockstar [40] catalogs and merger trees [41] [3] to measure halo mass accretion histories. For each halo, we walked the main branch of the merger tree to determine the mass accretion history (MAH) over a narrow redshift range, typically from $(0.67-1)\times a_{\rm obs}$. Then we fit the MAH to the form $M_{\rm vir}\propto e^{-\alpha z}$ [42] over the narrow redshift range, and used the fitted value of α to determine $\Gamma = d(\log M_{\rm vir})/d(\log a)$ at $a = a_{\rm obs}$. We then stacked halos in bins of mass, redshift, and Γ.

One point to note is that $\Gamma = d(\log M_{\rm vir})/d(\log a)$ need not be equal to the mass accretion rate $s = d(\log M)/d(\log a)$. This is because $M_{\rm vir}$ does not represent the total amount of mass that has collapsed into a halo. Instead, $M_{\rm vir}$ is the mass within a radius of average density $\Delta_{\rm vir}$. As Fig. 4.1 shows, the splashback radius (which does encompass the collapsed mass) occurs at various overdensity levels depending on redshift and accretion rate, meaning that sometimes $M_{\rm vir}$ will exceed $M_{\rm collapsed}$, sometimes $M_{\rm vir}$ will be less than $M_{\rm collapsed}$, and in general, the two will not evolve in the same way. This difference in behavior has been termed pseudo-evolution by [43], who point out that even in cases where there is no mass accretion and the halo mass profile is constant in physical units, the virial mass can still grow over time. Because of pseudo-evolution, in general $\Gamma \neq s$. This complicates the comparison of our model with cosmological N-body simulations. Instead of stacking halos based on virial mass, we should stack halos based on the mass within their splashback radius, however it is difficult to determine the splashback radius for any individual halo. We therefore stack the profiles of halos in bins of $M_{\rm vir}$ and Γ. From the stacked profiles, we can determine the location of splashback and the average enclosed mass, $\langle M_{\rm collapsed}\rangle$. By repeating this procedure for the progenitors of the stacked halos, we can determine $\langle M_{\rm collapsed}\rangle$ as a function of time, and thereby measure a typical accretion rate s for each bin of $M_{\rm vir}$ and Γ. We find that for $\Gamma \gtrsim 0.5$, the difference between the reconstructed s and Γ is small, typically of order $\Gamma - s \sim 0.1$. We therefore use Γ as a proxy for s, valid for $\Gamma > 0.5$.

With that caveat in mind, we now move on to the comparison of our model with cosmo-

[3] http://hipacc.ucsc.edu/Bolshoi/MergerTrees.html

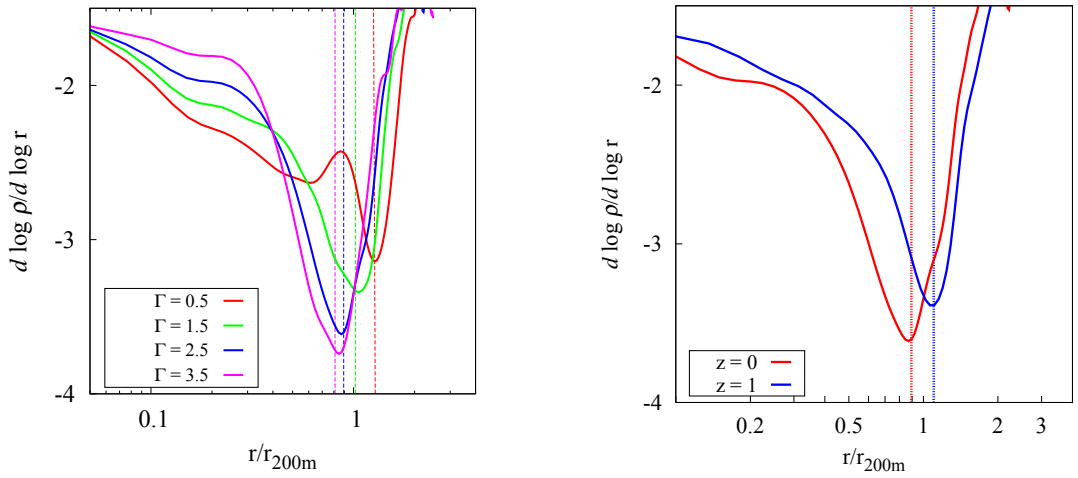

Figure 2.5: (Left) Dependence of splashback location on growth rate Γ. Here we show the comparison between the model predictions and the simulation results for $z = 0$ and $\Omega_M = 0.27$. The dashed vertical lines are at the predicted position of splashback as a function of $s \approx \Gamma$. The curves correspond to halos of mass $M_{\rm vir} = 1 - 4 \times 10^{14} h^{-1} M_\odot$, binned according to growth rate Γ.(Right) Redshift dependence of splashback location. The blue curve shows $z = 1$ halos of mass $M_{\rm vir} = 3 - 6 \times 10^{13} h^{-1} M_\odot$, while the red curve shows $z = 0$ halos of mass $M_{\rm vir} = 1 - 4 \times 10^{14} h^{-1} M_\odot$. Both samples have accretion rates $\Gamma = 2.5$. The vertical lines indicate the expected splashback radii.

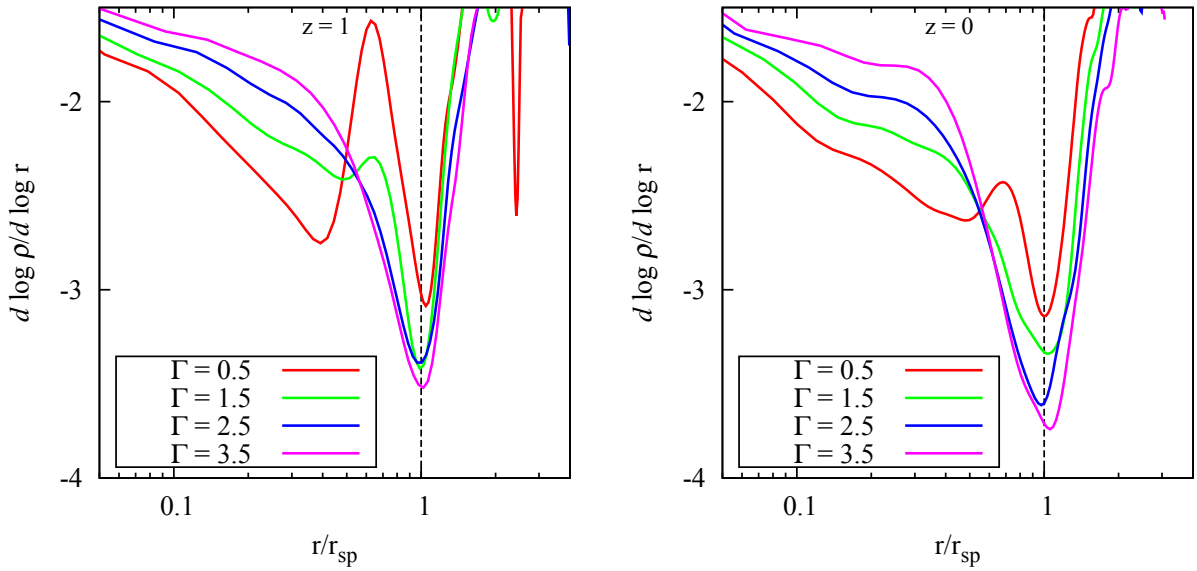

Figure 2.6: (Left) Local density slope as a function of $r/r_{\rm sp}$ for stacked N-body halos at $z = 1$ with mass $M_{\rm vir} = 3 - 6 \times 10^{13} h^{-1} M_\odot$, where $r_{\rm sp}$ is the predicted splashback radius computed using the spherical collapse model of §2.2. Different colors correspond to different accretion rates as indicated. The vertical black dashed line shows the expected position of splashback. (Right) Similar, but for halos with $M_{\rm vir} = 1 - 4 \times 10^{14} h^{-1} M_\odot$ at $z = 0$.

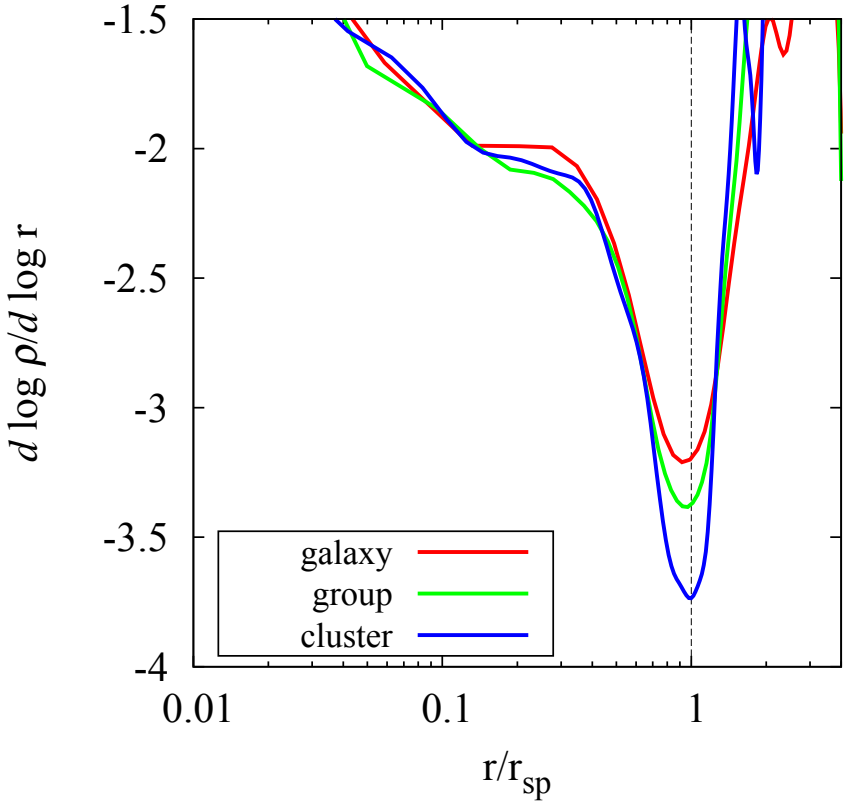

Figure 2.7: Local density slope for halos with accretion rate $\Gamma = 2$ and $z = 0$, as a function of halo mass or ν. The various curves correspond to $M_{\rm vir} = 1 - 3 \times 10^{12} h^{-1} M_\odot$ (red), $M_{\rm vir} = 3 - 5 \times 10^{13} h^{-1} M_\odot$ (green), and $M_{\rm vir} = 3 - 4 \times 10^{14} h^{-1} M_\odot$ (blue). These mass bins correspond to $\nu \sim 0.9$, 1.5, and 2.5, respectively. The location of the splashback feature remains the same, independent of mass, although the depth of the feature depends on M (or equivalently ν).

logical N-body simulations. Our results are shown in Figs. 2.5-2.7. The left panel of Figure 2.5 shows the dependence of the splashback radius on the accretion rate, Γ. As shown by [26], splashback occurs at a higher density (smaller r/r_{200m}) for higher accretion rates. Our model's prediction for $r_{\rm sp}$ agrees quite well with the observed dependence on accretion rate, across the entire range we have checked ($0.5 < \Gamma < 3.5$). We also confirm the model's predicted redshift dependence of splashback (Fig.2.5 right column). Since these figures have many overlapping curves at different radii, it may be difficult to see how well the observed splashback radius agrees with the model prediction. Therefore, in Fig. 2.6 we scale r by

the predicted splashback radius $r_{\rm sp}$, and show that splashback occurs where predicted, at all accretion rates and redshifts. Similarly, as predicted by the model, the location of splashback does not depend on halo mass M (or equivalently, $\nu \equiv \delta_c/\sigma(M)$), as illustrated in figure 2.7.

One possibly interesting feature shown in Fig. 2.7, and also noted by [26], is that although the location of the steepening feature is independent of M or ν, the *depth* of the feature does depend systematically on ν. As shown in the figure, the lower mass halos, which correspond to peaks of smaller ν, have systematically shallower caustics. The behavior is reminiscent of that shown in Fig. 2.3, which showed that similarity solutions with stronger initial triaxiality produce caustics that are progressively more non-spherical, producing shallower features in the spherically averaged profile. Similar behavior could also explain the ν dependence of the N-body halos. It is well known from the statistics of peaks of Gaussian random fields that peaks of larger height ν are systematically more spherical, with a smaller range of ellipticity e, than peaks of low ν [44]. Based on the behavior shown in the similarity solutions shown in Fig. 2.3, we might therefore expect that N-body halos of larger ν will have smaller initial ellipticity, and therefore have deeper caustics, than halos with lower ν, exactly as found in Fig. 2.7. We have not investigated this topic in this paper, but it may be worth exploring in future work.

At low accretion rates, $\Gamma < 1$, the stacked profiles begin to exhibit additional features besides the steepening at $r_{\rm sp}$. The most pronounced example of this is the stacked profile for $\Gamma \approx 0.5$, shown in Fig. 2.6. Instead of monotonically becoming more shallow at $r < r_{\rm sp}$, the slope of the density profile oscillates. The origin of this behavior may be understood by examining the ensemble phase space diagram for these halos, shown in Figure 2.8. The phase space structure for low accretion rate is distinct from the other Γ bins, in that the stream of splashback material is noticeably separated from the rest of the virialized matter in the halo. This behavior is similar to the phase space structure seen in spherical self-similar collapse [2], in which each separate stream produces a separate caustic (see Fig. 2.3).

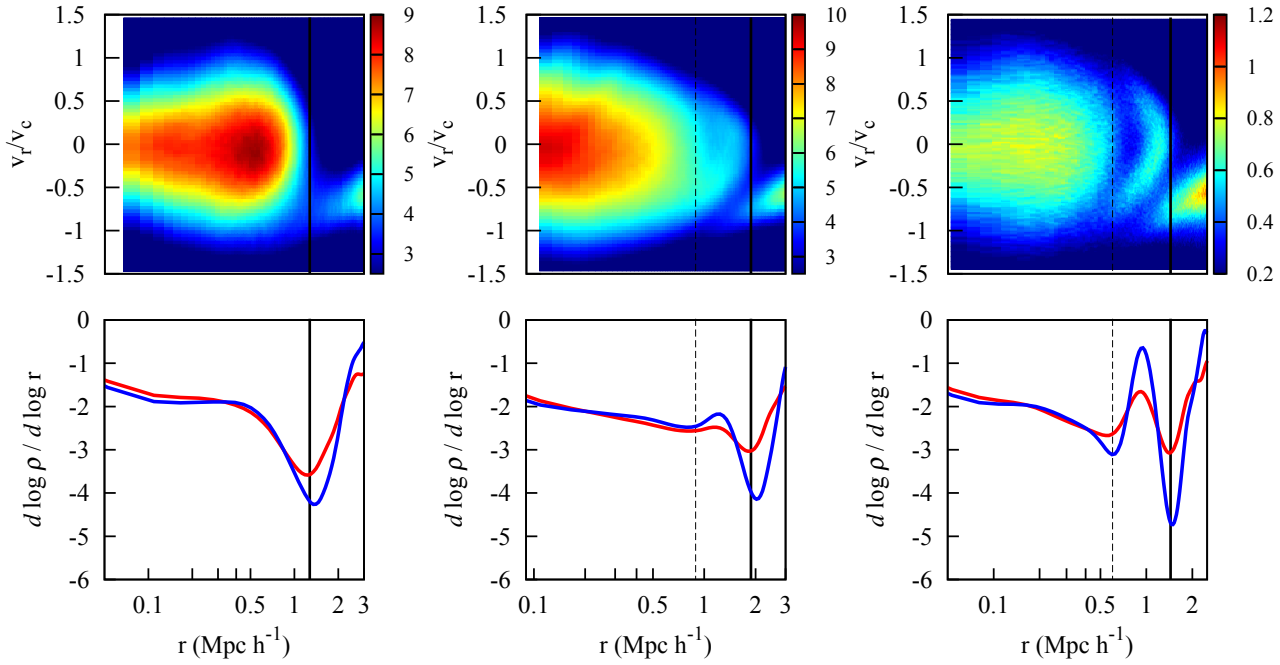

Figure 2.8: Phase space diagram for different accretion rates. The left panel shows halos in the mass range $M_{\rm vir} = 1 - 4 \times 10^{14} h^{-1} M_\odot$ at $z = 0$ for accretion rates $\Gamma \approx 3$. The middle panel shows halos of the same mass and redshift, but with $\Gamma \approx 0.5$. The right panel shows halos with $M_{\rm vir} = 3 - 6 \times 10^{13} h^{-1} M_\odot$ at $z = 1$, also with $\Gamma \approx 0.5$. The bottom panels show the slope of the local density profile of all mass in red, and for particles with $|v_r| < 0.4 v_c$ in blue. This is similar to Fig. 2.1, which showed results for an intermediate growth rate $\Gamma \approx 1.5$. Note that at low accretion rates, the splashback material forms a distinct stream, which leads to multiple minima in the run of density slope vs. radius, indicated by the vertical dashed lines.

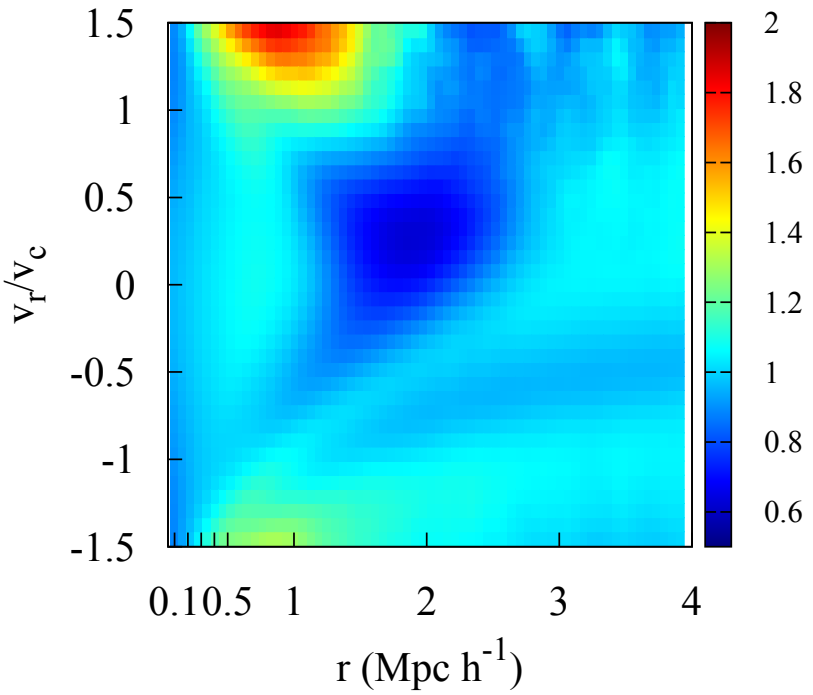

Figure 2.9: Map of accretion rate Γ as a function of phase space coordinates r and v_r for halos in the mass range $M_{\rm vir} = 1-2\times10^{14}h^{-1}M_\odot$ at $z = 0$. For these halos, $R_{\rm vir} \approx 1h^{-1}$Mpc. Note that at large radii, $r \sim 2h^{-1}$Mpc, most of the outgoing material ($v_r > 0$) is associated with slowly accreting halos with $\Gamma \approx 0.5$.

2.4 Implications of detection of the Splashback radius

Depending on the accretion rate and redshift, the overdensity at the splashback radius, Δ_s, can be much larger or much smaller than either $\Delta = 200$ or $\Delta_{\rm vir}$, the nominal 'virial' overdensity, which is typically in the range 200-300 [34]. Since the splashback radius encompasses the multi-streaming region, this means that the virialized region surrounding a halo can extend far beyond $R_{\rm vir}$. This fact is not surprising: numerous simulations have found that material which has passed inside $R_{\rm vir}$ can later be found at large distance, e.g. $\sim 2-3R_{\rm vir}$ [45, 31, 46, 47, 48, 49]. As we have seen, recently accreted material can splash back to such large distances, when the accretion rate in the halo is low. Our expectation, therefore, would be that much of the halo material found at large distances ($\sim 2-3R_{\rm vir}$) is associated with slowly accreting halos. To demonstrate this, we plot in Figure 2.9 the average halo accretion rate for material around halos of mass $M_{\rm vir} = 1-4\times10^{14}h^{-1}M_\odot$ at $z = 0$ as a function

of phase space coordinates r and v_r. Outgoing material (i.e. $v_r > 0$) at $r \approx 2R_{\rm vir}$ (which is $r \sim 2h^{-1}$Mpc for this mass bin) is typically found around halos with the lowest accretion rates, $\Gamma \approx 0.5$.

In principle, the steepening associated with splashback could be observable. The projected surface density of dark matter halos shows a similar steepening at the same location at the 3D steepening feature [26], implying that this feature may be observable in the stacked lensing profiles of ensembles of halos [50]. As we have seen, the steepening feature associated with splashback is most prominent for massive (high ν) objects with high accretion rates. This suggests focusing on galaxy clusters, rather than lower-mass objects like galaxies whose lower accretion rates would produce weak splashback features possibly in the 2-halo region. In practice, it is often difficult to predict halo masses from observable quantities like cluster richness or SZ decrement, meaning that stacked profiles will typically average over wide mass bins. This will not necessarily wash out the steepening signature, however. In our analysis of stacked profiles, we found that stacking rather wide bins of mass (such as a factor of 4 in $M_{\rm vir}$) does not wash out the steepening feature, e.g. Fig. 2.6. Therefore, realistic uncertainties in the mass-observable relation should not wash out the steepening feature entirely. If the steepening feature is measured with high significance, then it may be interesting to stack halos as a function of various observable properties like concentration. Measuring how the splashback radius depends on those observable properties immediately translates into a measurement of how well the mass accretion rate correlates with those properties, which can test the predicted behavior for CDM cosmologies [42, 51].

Similar steepening features could also arise in the baryonic components of halos. Unlike the dark matter, however, the baryons are not collisionless, which means that splashback need not occur at the same location as the dark matter. Hydrodynamic simulations of galaxy cluster outskirts can quantify whether gas splashback occurs near dark matter splashback [52]. Stars, unlike gas, are effectively collisionless at the densities found in halo outskirts, so the stacked starlight profiles of ensembles of halos could in principle exhibit similar behavior

as the dark matter. Dynamical friction could potentially slow down stars in galaxies relative to unbound dark matter, though, so it may be worthwhile performing simulations with star formation to check if stars produce similar caustics as the dark matter. In the next section I will elaborate on the effects of dynamical friction on subhalo splashback.

Chapter 3

Observing Dynamical friction in Galaxy Clusters

We present a novel method to detect the effects of dynamical friction in observed galaxy clusters. Following accretion into clusters, massive satellite galaxies will backsplash to systematically smaller radii than less massive satellites, an effect that may be detected by stacking the number density profiles of galaxies around clusters. We show that this effect may be understood using a simple toy model which reproduces the trends with halo properties observed in simulations. We search for this effect using SDSS redMaPPer clusters with richness $10 < \lambda < 20$, and find that bright ($M_i < -21.5$) satellites have smaller splashback radii than fainter ($M_i > -20$) satellites at 99% confidence. [1]

3.1 Introduction

In the standard cosmological model, cosmic structures form hierarchically. Short wavelength perturbations collapse to generate low-mass halos, which subsequently merge to create larger halos, which themselves merge to form even larger structures, and so on. Every macroscopic structure in the dark matter field is believed to have assembled out of constituent structure on smaller scales. Much of that substructure survives within halos, however a considerable amount of substructure is dynamically erased, through processes like tidal stripping and dynamical friction. In this paper, we focus on the latter process.

Dynamical friction is an effective gravitational drag experienced by massive bodies mov-

[1]This chapter was previously published in the Journal of Cosmology and Astroparticle Physics as S. Adhikari, N. Dalal and J. Clampitt, Observing dynamical friction in galaxy clusters, JCAP 1607 (2016) 022, [1605.06688].This chapter matches the published version.

ing through a population of lower mass bodies [53, 54]. A dark matter subhalo orbiting inside a larger halo will experience dynamical friction due to the density of dark matter particles in the host halo, with a rate

$$\frac{d\boldsymbol{v}}{dt} \propto -\frac{G^2 M \rho}{v^3} \boldsymbol{v} f(v, \sigma), \tag{3.1}$$

where M is the mass of the subhalo, $\boldsymbol{v}$ is its velocity relative to its host, and ρ is the density through which it moves. The proportionality constant depends on the distribution function of the particles, as well as the internal structure of the subhalo. The drag is largest for the most massive subhalos with large M.

The effects of dynamical friction are manifest in simulations of nonlinear cosmological structure formation. Dynamically young halos, like massive galaxy clusters, contain copious amounts of massive substructure that comprise significant fractions of the cluster's total mass. For example, it is not uncommon to find massive subhalos within clusters, containing $\sim 1 - 10\%$ of the cluster mass [55]. In contrast, massive substructure is rare in dynamically older halos, like those hosting galaxies similar to the Milky Way. In galactic halos, it is uncommon to find individual subhalos comprising more than $\gtrsim 3\%$ of the host mass [1]. Dynamical friction is believed to be the origin of this difference: in the older systems, drag from dynamical friction had sufficient time to cause the orbits of massive subhalos to decay to small radii, where mass loss from tidal stripping and disruption becomes most effective [56]. The proportion of substructure in real galaxies and clusters is presumably affected by the same processes that arise in simulations.

Therefore, considerable indirect evidence exists that dynamical friction should operate in actual halos. It is difficult, however, to directly observe dynamical friction in action, since the relevant timescales are cosmological in duration. In this paper, we propose a novel method to directly observe the deceleration produced by dynamical friction acting on massive galaxies within galaxy clusters. The basic idea is that drag from dynamical friction

reduces the orbital energy of galaxies within subhalos, which reduces the apocentric radius. Recent work has shown that a steepening feature in the density profiles of halos occurs near the apocenters of material on its first orbit within halos, termed the splashback feature [26, 4, 57]. In the context of the halo model [58, 59], this feature may be thought of as the boundary of the 1-halo region. For massive cluster-sized halos, where the 1-halo term is large compared to the 2-halo term, the sharp edge to the 1-halo term produces a steep falloff in the total density profile at the splashback radius $r_{\rm sp}$, and therefore the location of the steepest slope of the density profile occurs close to $r_{\rm sp}$. Dynamical friction reduces $r_{\rm sp}$, and because friction is more effective for more massive subhalos, high-mass satellites should therefore have a smaller splashback radius than low-mass satellites. For the lowest mass subhalos, the dynamical friction timescale greatly exceeds the orbital timescale, and therefore for these satellites the splashback radius coincides with that of the dark matter particles.

3.2 Dynamical friction in simulated clusters

Figure 3.1 illustrates this effect, using results from the MDPL2 simulation from the CosmoSim database [37, 60]. The figure shows the density slope $d\log n/d\log r$ as a function of radius for subhalos of varying $M_{\rm peak}$, the largest mass attained by each subhalo throughout its history. Halos and subhalos were selected from the Rockstar [61, 62] catalogs publicly available at `http://cosmosim.org`. The splashback radius for low-mass subhalos is indistinguishable from the splashback radius of dark matter particles, but as $M_{\rm peak}$ increases, the splashback radius steadily decreases. This effect appears to be caused by dynamical friction, rather than selection effects or other physical processes which affect the spatial distribution of substructure. For example, it has long been known that subhalos orbiting at small radii tend to have earlier accretion redshifts than subhalos orbiting at large radii within their hosts [63, 64, 65, 56]. One might therefore imagine that the difference in splashback radii

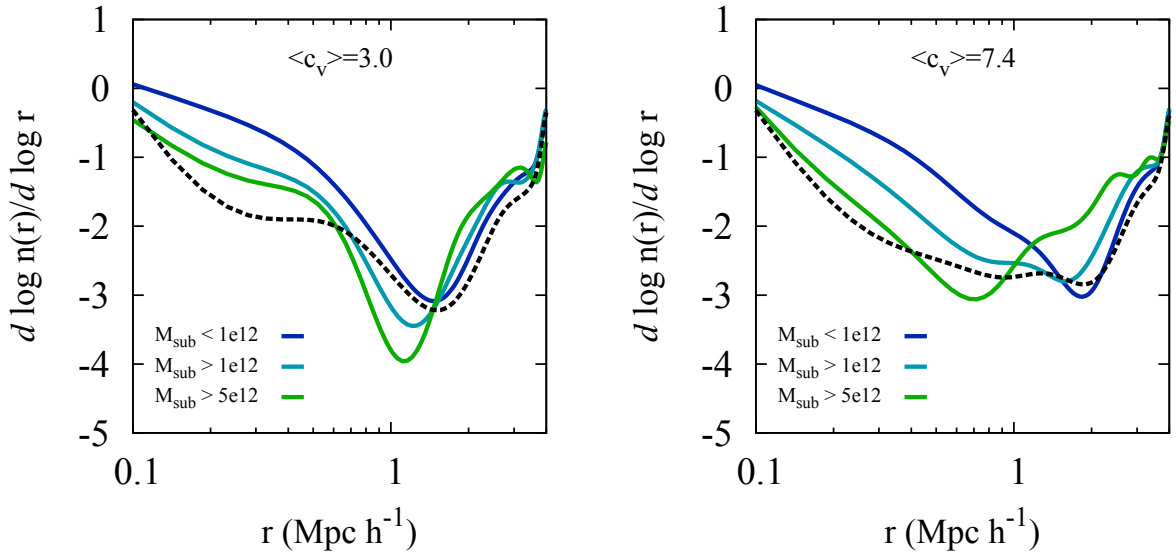

Figure 3.1: In both panels, the different curves show the logarithmic slope of the number density profile $d\log n/d\log r$ as a function of radius r within cluster-sized halos of virial mass $M_{\rm host} = 1 - 4 \times 10^{14} h^{-1} M_\odot$ from the MDPL2 simulation, for various populations within the host halos. The dashed line corresponds to all dark matter particles, while the solid lines show subhalos of different mass, as denoted in the legend. The splashback radius occurs at the location of the steepening feature in these profiles. Subhalos with less than 1% of the host mass have similar splashback radii as the full set of DM particles, while more massive subhalos have smaller splashback radii, consistent with the effects of dynamical friction. The left panel shows host halos with $c_{\rm vir} < 4$, while the right panel shows host halos with $c_{\rm vir} > 6$, illustrating the significant dependence of dynamical friction effects on host concentrations. Subhalo masses are expressed in units of $h^{-1} M_\odot$.

between high-mass and low-mass subhalos might be due to systematic differences in the accretion times for those subhalo samples (caused by resolution effects, for example), but we have checked that the distribution of accretion redshifts as defined in the Rockstar catalog is nearly identical for low-mass and high-mass subhalos. This precludes the difference in $r_{\rm sp}$ from arising from mass-dependent selection effects which can convert the radial dependence of mean accretion redshift into an apparent radial dependence of subhalo mass. Another line of evidence for dynamical friction as the explanation for the trend of $r_{\rm sp}$ with mass is the concentration dependence of the effect. As Fig. 3.1 shows, the decrease in $r_{\rm sp}$ is stronger for hosts with higher concentration $c_{\rm vir}$. This is expected for dynamical friction, since increasing $c_{\rm vir}$ raises the central density, which increases the drag rate as seen in Eqn. (3.1).

The splashback feature therefore offers a direct method to observe the effects of dynamical friction. It is straightforward to estimate how dynamical friction will affect the splashback radius, using the spherical collapse model of [4]. We modify their model somewhat, adding an extra term to the equation of motion to account for dynamical friction,

$$\frac{dv_r}{dt} = -\frac{GM(r)}{r^2} - \eta\frac{G^2 M_{\rm sub}\rho(r)}{|v_r|^3}v_r f(v_r/\sigma). \tag{3.2}$$

Here, $M_{\rm sub}$ is the mass of the subhalo (we neglect tidal stripping), v_r is its radial velocity, $M(r)$ is the host halo mass enclosed within radius r, $\rho(r)$ is the local density at radius r, the phase space factor is taken to be that for a Maxwellian distribution, $f(x) = \mathrm{erf}(x) - 2\pi^{-1/2}x\,e^{-x^2/2}$ [54], and η is the unknown proportionality constant from Eqn. (3.1). Since we do not have a first principles calculation of η, we treat it as a free parameter that is fit to the simulation data. We find that $\eta \approx 1.4$ provides a reasonable fit for the cluster-sized host masses we have considered. For simplicity, in this toy model we assume radial orbits for subhalos, which is unphysical but reduces the number of dynamical variables. Because radial orbits pass through the host center $r = 0$ where the NFW profile diverges, we instead approximate the host profile using a cored isothermal profile, with $r_{\rm core} = 0.1 \times r_{\rm vir}$. Figure

3.1 shows this is a reasonable approximation to the host profile well inside the splashback radius, since at about $0.1\,r_{\rm sp}$ the density profile slope (black dashed line) rapidly transitions from -2 to 0. The splashback location for the particles are in good agreement with predictions from the previous model and with simulations.

This simple toy model reasonably reproduces the location of the splashback feature for different subhalo mass bins and for different host accretion rates $\Gamma = d\log M_{\rm vir}/d\log a$, as shown in Fig. 3.2. In particular, low-mass subhalos comprising $\lesssim 1\%$ of their host halo's mass do not appear to experience significant drag from dynamical friction. However, it might be interesting to construct a more realistic model that more accurately describes the structure of the host halo, since the MDPL2 results suggest that dynamical friction effects on the splashback radius depend significantly on the concentration of the host halo (see Fig. 3.1).

In principle, therefore, measurement of the splashback radius for different galaxy masses could be used to constrain the amount of dynamical friction experienced by those galaxies, which in turn constrains the initial masses (at infall) of the subhalos hosting those galaxies. A comparison of those infall masses to the present-day masses, inferred from galaxy-galaxy lensing of satellites [66, 67], then reveals the mass loss from tidal stripping suffered by satellites. Such a measurement would not only help inform our understanding of dynamics within galaxy clusters, but would also provide new insights on the halo occupation of satellites, directly testing models like subhalo abundance matching [68].

3.3 Dynamical friction in observed clusters

[69] recently observed the splashback feature in SDSS redMaPPer clusters [70, 71]. Building on that work, we conduct a similar measurement to search for signatures of dynamical friction in clusters. We use redMaPPer clusters with richness $10 < \lambda < 20$ in the redshift range $0.15 < z < 0.33$, and compute the projected number density $n(R)$ of SDSS galaxies

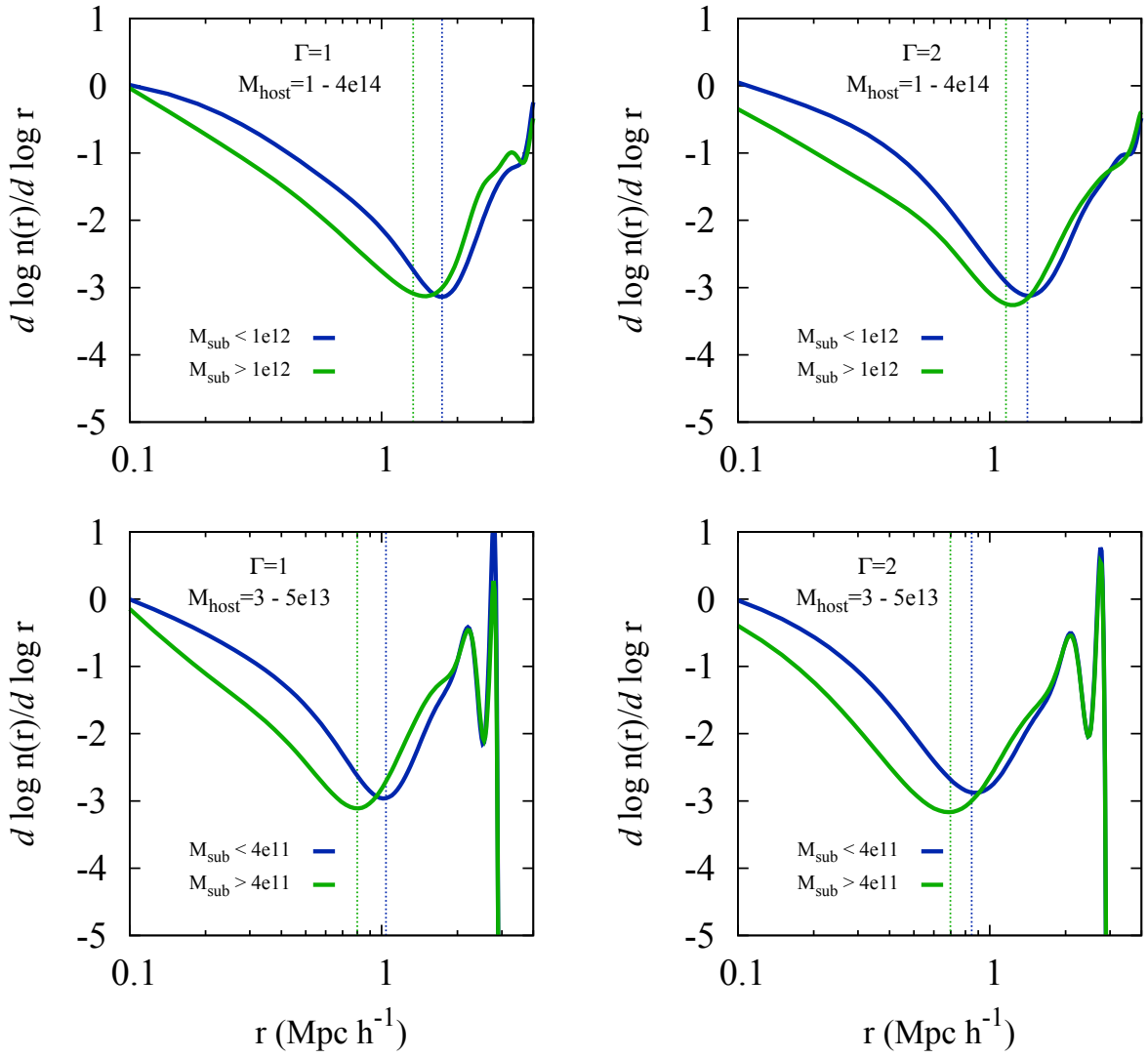

Figure 3.2: Shift in the location of splashback due to dynamical friction in subhalos with $M_{\rm sub} > 0.01 M_{\rm host}$ in bins of different accretion rate $\Gamma = d\log M_{\rm host}/d\log a$ (left vs. right) and for bins of different host mass $M_{\rm host}$ (top vs. bottom). Halo masses are expressed in units of $h^{-1}M_\odot$. The vertical lines show the prediction from the toy model Eqn. (3.2). The blue vertical line shows the predicted location in a model without dynamical friction [4], which agrees well with the splashback radius $r_{\rm sp}$ for low mass subhalos where dynamical friction is unimportant. The green vertical line shows the predicted position of splashback from the collapse model with dynamical friction where $\eta = 1.4$, evaluated at the mean subhalo mass of the sample with $M_{\rm sub} > 0.01 M_{\rm host}$.

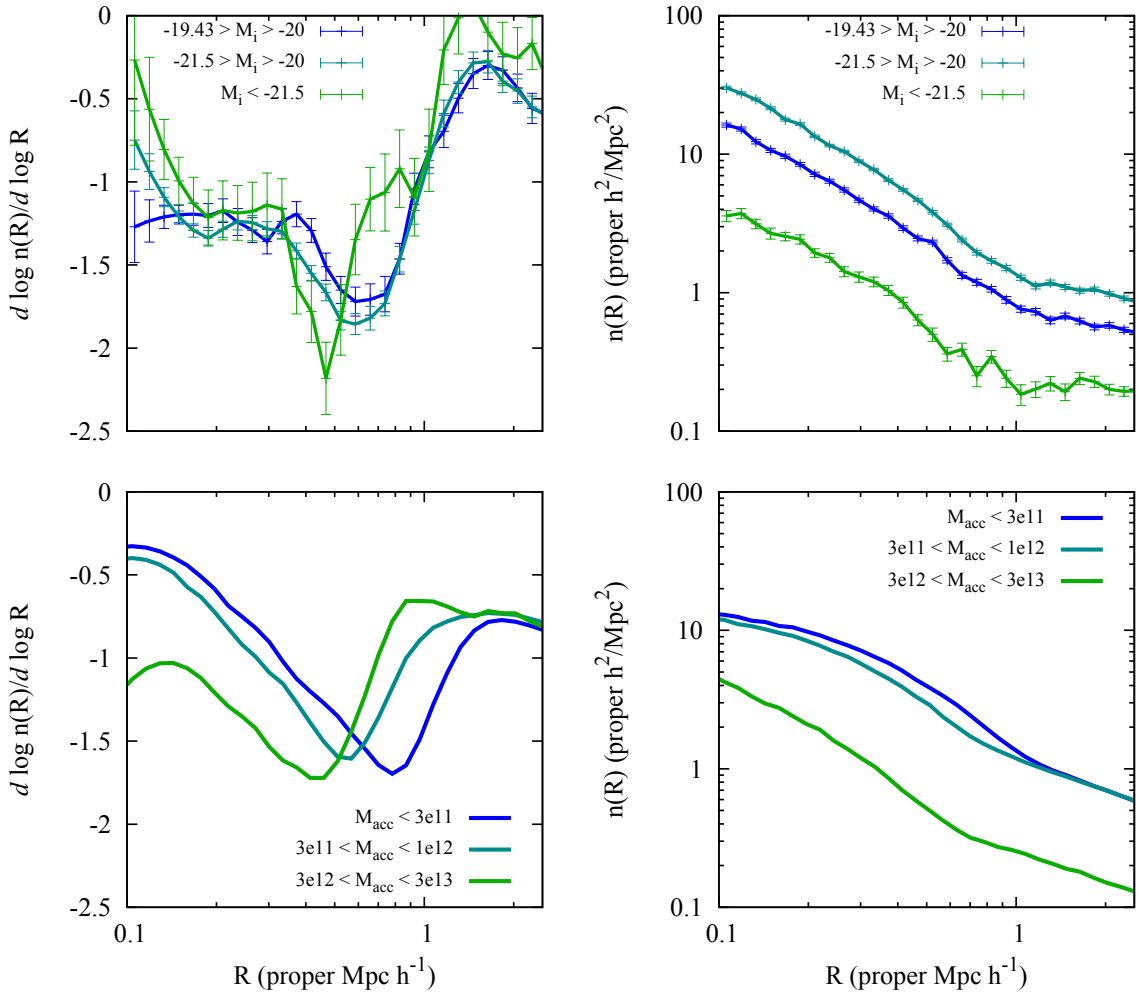

Figure 3.3: (Top) Observations of splashback in clusters from the redMaPPer catalog of galaxy clusters with $0.15 < z_c < 0.33$ and $10 < \lambda < 20$. The left panel shows the logarithmic slope of the projected number density of galaxies as a function of cluster-centric radius, the projected number density profile is plotted on the right. (Bottom) Corresponding profiles for subhalos in host halos with $M_{200\mathrm{m}} = 3 - 9 \times 10^{13} h^{-1} M_\odot$ at $z = 0.25$ from the MDPL2 simulation. This host mass range was chosen to match the richness range from the top panel. Both panels show the slope and magnitude of the projected density, not the 3D space density, in contrast to the previous figures.

with measured photometric redshifts. In Fig. 3.3 we plot the logarithmic derivative of the projected number density, $d\log n/d\log R$, for galaxies in various bins of absolute magnitude in the i band, M_i. To determine the absolute magnitude, we ignore the measured photometric redshift for each galaxy, and instead assume the galaxy is at the redshift of the redMaPPer cluster when converting the observed apparent magnitude to absolute magnitude [69]. We also use the angular diameter distance at the cluster redshift to translate angular separation into projected physical separation. We count galaxies in bins of projected separation R, and then compute the logarithmic slope $d\log n/d\log R$ using a cubic Savitzky-Golay filter over 11 points [72], accounting for the covariance of the bins. We have used a lower richness cluster sample than [69], since for a given galaxy population, dynamical friction is expected to be stronger for hosts of lower mass. We have confirmed, however, the result of [69] that host clusters with $\lambda > 20$ do not exhibit signficant evidence for dynamical friction, since there is no significant trend of $r_{\rm sp}$ with satellite galaxy luminosity in their sample.

For the lower richness sample used here, Fig. 3.3 shows that the brightest galaxies with $M_i < -21.5$ have a significantly smaller splashback radius than fainter galaxies. If we assume that $r_{\rm sp}$ is given by the location of the steepest slope of the projected profile (which can somewhat underestimate the value of the 3D splashback radius), we can determine $r_{\rm sp}$ from the Savitzky-Golay fit. The probability that radius r is the location of the steepest slope, $P(r)$, may straightforwardly be determined by integrating over the probability distribution of the Savitzky-Golay coefficients,

$$\begin{aligned} P(r) &= \int P(a_0, a_1, \ldots, a_n) \\ &\quad \times\delta\left(\frac{d^2\log n}{d(\log R)^2}\right)\Theta\left(\frac{d^3\log n}{d(\log R)^3}\right) d^{n+1}\boldsymbol{a}, \end{aligned} \tag{3.3}$$

where $a_0, a_1, \ldots, a_n$ are the $n+1$ Savitzsky-Golay coefficients at location r, whose posterior distribution $P(a_0, \ldots)$ is assumed to be a Gaussian distribution with covariance determined from the data covariance as in [69]. This expression states that the probability that radius r

is the splashback radius is given by the probability that the derivative of the slope vanishes, $d^2 \log n/d(\log R)^2 = 0$, enforced by the Dirac δ-function, and the 2nd-derivative of the slope is positive, enforced by the Heaviside function $\Theta(d^3 \log n/d(\log R)^3)$. We find that $r_{\rm sp} = 0.42 \pm 0.04\,h^{-1}\,{\rm Mpc}$ (proper, not comoving) for the $M_i < -21.5$ sample, while $r_{\rm sp} = 0.55 \pm 0.04\,h^{-1}\,{\rm Mpc}$ for the $-19.43 < M_i < -20$ sample. The probability that $r_{\rm sp}$ is smaller for the bright sample than the faint sample is readily determined from the probality distributions for the splashback radii for the two luminosity bins, $P(r_{-21.5})$ and $P(r_{-20})$, each computed from Eqn. (3.3). We find that $\int P(r_{-21.5})P(r_{-20})\Theta(r_{-20}-r_{-21.5})dr_{-21.5}dr_{-20} = 99.3\%$, giving nearly 3σ confidence that brighter satellites have smaller $r_{\rm sp}$ than fainter satellites in the same clusters. This trend qualitatively agrees with our analytical and numerical predictions. A quantitative comparison with theoretical predictions would require constructing a mock galaxy catalog from simulations and running the redMaPPer algorithm to find clusters and their member galaxies, which is beyond the scope of the present work. However, we can perform a very crude comparison as follows. [73] find that the mean halo mass for richness λ is $M_{\rm 200m} = 10^{14.3}h^{-1}M_\odot(\lambda/40)^{1.33}$, while [74] find a mean relation $M_{\rm 200c} = 10^{14.19}M_\odot(\lambda/30)^{1.31}$, although the scatter about the mean relation appears quite large, ~ 0.7 dex at $\lambda \approx 20$. Assuming this mean relation of [73], our sample with $10 < \lambda < 20$ should roughly correspond to halos with $M_{\rm 200m} = 3 - 9 \times 10^{13}h^{-1}M_\odot$. We have selected halos in this mass range at $z = 0.25$ (the median redshift of our sample) from the MDPL2 simulation, and in Fig. 3.3 we plot the logarithmic slope of the projected number density, $d\log n/d\log R$, for neighboring halos and subhalos in various bins of $M_{\rm acc}$, the mass at accretion. (For isolated halos, $M_{\rm acc} = M_{\rm vir}$.) As the figure shows, subhalos within these hosts show a range of $r_{\rm sp}$ spanning the range seen in the redMaPPer satellites. By matching splashback radii between observed satellite galaxies and simulated subhalos, we can estimate the typical infall masses of those satellites, and a comparison with their present-day lensing masses [66, 67] would be an interesting test of whether dynamical friction in real clusters proceeds similarly to the behavior found in simulations.

3.4 Discussion

In this paper, we have shown that the splashback radius may be used to detect the effects of dynamical friction in galaxy clusters. We showed that the friction observed in simulations may be understood quite simply using the 1-D model of [4]. We showed that SDSS redMaPPer clusters exhibit significant evidence for dynamical friction, and we argued that this result places interesting constraints on the subhalo occupation distribution of satellite galaxies in those clusters.

Besides probing the subhalo occupation distribution of cluster satellites, observations of dynamical friction can also help constrain more fundamental physics. We have estimated the amount of dynamical friction that occurs within cold dark matter (CDM) cosmologies, in which gravity follows Einstein's general relativity and dark matter consists of collisionless particles. Departures from the CDM model could produce significant deviations in the splashback radius of massive galaxies. For example, some previous works have found that dynamical friction can be significantly strengthened in MOND-like theories without particle dark matter [75], which may be interesting to explore in more recent variants of modified gravity models [76]. Similarly, certain self-interacting dark matter models can also predict an effective drag of satellites [77] that could be studied using the splashback feature. Given the detection of the splashback feature in SDSS clusters, and improvements from deeper imaging surveys like DES and HSC, splashback may provide a new window onto a variety of physics.

Chapter 4

Splashback as a probe for Cosmology

In light of the recent detection of the steepening of slope of the density profile of clusters near the virial radius, known as the splasback feature, we study how different cosmologies effect the location and shape of the feature. As the location of splashback depends on the accretion rate of a halo and the redshift at which it forms, limited sensitivity to background cosmology makes it a robust probe for the accretion history of halos.

4.1 Introduction

ΛCDM has been highly successful in explaining a vast array of observable properties of our universe and its evolution. However there still exist considerable discrepancies between simulations of ΛCDM cosmologies and observations. For example at small scales, the missing satellite problem, the core-cusp problem and the too big to fail problem are some of the known disagreements between simulations and observations. Solving these problems often requires introduction of non-gravitational interactions in the dark matter. Apart from these small scale issues, there are several alternate theoretical models that make the same predictions as ΛCDM on large scales, for example, it is well know that modifying gravity on large scales can reproduce the accelerated expansion of the universe. Therefore, a lot of motivation exists to explore cosmologies beyond ΛCDM, and find observable tests to disentangle these models from ech other.

The formation and evolution of dark matter halos gives us key insights into some of the fundamental questions of cosmology. The inner structure and assembly of these highly non-

linear, virialized objects are not only related to the individual density perturbations in the early universe that collapsed to form them but also to the environment in which they grow. In theory they have been studied extensively through pioneering works by [2], [21],[78] who dealt with the self-similar collapse of density perturbations, and also through increasingly advanced, high resolution N-Body simulations.

The density profile of dark matter halos in simulations are well fitted by NFW like power law profiles. However, recent work by [26] has shown that the profile deviates significantly from the NFW in regions at the outskirts of the halo. The slope of the density profile becomes much steeper than -3 in a narrow, localized region around the virial radius of the halo. [26] and [79] argue that this deviation is a density cautic, i.e. a narrow region of locally enhanced density, occuring at the first apocentric passage of matter that falls into the halo for the first time, known as the splashback radius. Diemer and Kravtsov and More 2015 provide empericial fitting functions for this feature as function of accretion rate and halo mass, while [79] and [80], characterize this feature using simple physical models. The location of this feature is fundamentally a function of the accretion rate of the halo and the background cosmological parameters, i.e. it depends also on the redshift at which the halo is formed. Therefore, the splashback radius is a scale within the halo which not only gives us the accretion history but also, owing to its dependence on cosmology, may serve as a cosmic ruler.

Recently [81] have observed this feature in the number density profiles of galaxies in redMapper clusters using the SDSS data. While the shape of the feature matches the data from N-body simulations of ΛCDM with collisionless dark matter, it is puzzling that the splashback feature occurs at a smaller radius than expected showing an offset of about 20% with simulations. As galaixes reside in massive subhalos within their host halos, it is not surprising that they might splashback at a smaller radius owing to the loss of orbital energy due to dynamical friction [82], however as the location of the feature does not show much dependence on galaxy magnitudes this possibility can be safely ruled out for high mass halos,

as dynamical friction only becomes important for subhalos with $M_{sub} > 0.01 M_{host}$. For other possible systematic error related explanations refer More et al. 2016. This discrepancy from simulations therefore leaves room for speculation as to how different cosmologies may affect the location of the splashback feature.

In this paper we have looked into how splashback behaves when we fold in deviations from the ΛCDM. In section 2.2 we explore how our model changes by varying the equation of state for dark energy, in section 4.3 we study splashback in modles of modified gravity and in section 6.2 we study the effects of introducing self-interactions of dark matter.

4.2 Splashback and the Dark energy equation of state

In Adhikari et al. 2014 [79] we described a simple model to predict the location of the splashback feature. The spherical collapse of a top hat density perturbation in an expanding universe has been used to study the formation of virialized halos. In general halos can be thought of being composed of collapsed shells of dark matter particles orbiting in a halo potential. The spherical collapse model assumes the mass within a shell remains constant until the shell is virialized. However, post turn around, as shells begin to orbit they cross each other and the mass within a shell does not remain constant.

In our paper we made a simple extension to the spherical collapse model, we continue to assume spherical symmetry but with the mass inside the shell changing with time and radius. The mass of the halo grows as $M_{\rm tot} \propto a^s$ and we assume an NFW profile for the mass interior to the radius r,

$$M(< r) = M_{\rm tot} \frac{f_{\rm NFW}(r/r_s)}{f_{\rm NFW}(R/r_s)}, \tag{4.1}$$

where R is the radius of the halo which grows like $R \propto a^{1+s/3}$, r_s is the NFW scale radius, and $f_{\rm NFW}(x) = \log(1+x) - x/(1+x)$. The NFW concentration $c \equiv R/r_s$ sets the slope of the mass profile at the halo boundary, and we choose c such that the outer slope is given by

$d\log M/d\log r = 3s/(3+s)$ at $r = R$ [2, 3, 8].

In Adhikari et al. 2014[79] we looked at the position of splashback in a λCDM universe, where the equation of motion of the shell is given by the Friedmann equation,

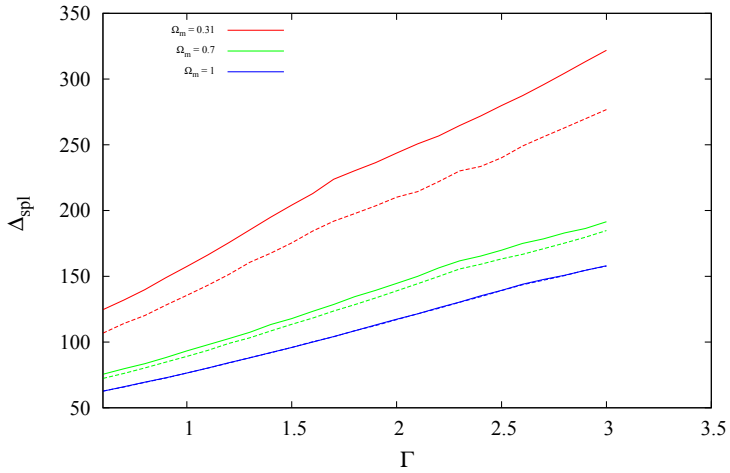

Figure 4.1: Overdensity enclosed within the splashback radius as a function of accretion rate $s = d\log M/d\log a$. Large Δ corresponds to small radius within the halo. The blue, green and red curves correspond to DE equation of state parameters w=-0.5, -1, -2 respectively.

$$\ddot{r} = -\frac{GM}{r^2} + \frac{\Lambda\, c^2}{3} r, \tag{4.2}$$

We evolve the orbits of the shell using spherical collapse until they reach $r_i = r_{ta}/2$ and thereon we assume that the shell is orbiting in a time changing mass profile. As in the spherical collapse model, we find the overdensity at splashback, Δ_s. In our model, Δ_s depends only on the halo's accretion rate s, along with the values of the background cosmological parameters Ω_M and Ω_Λ at the time the halo is observed.

The overdensity at splashback naturally depends on the expansion rate of the background universe. In the time elapsed between turn around and splashback, the background universe has expanded at a certain rate depending on the cosmology we assume. Previously we investigated the behavior of splashback in a universe with the cosmological constant. However, it is simple to modify our model to introduce a dark energy equation of state where the

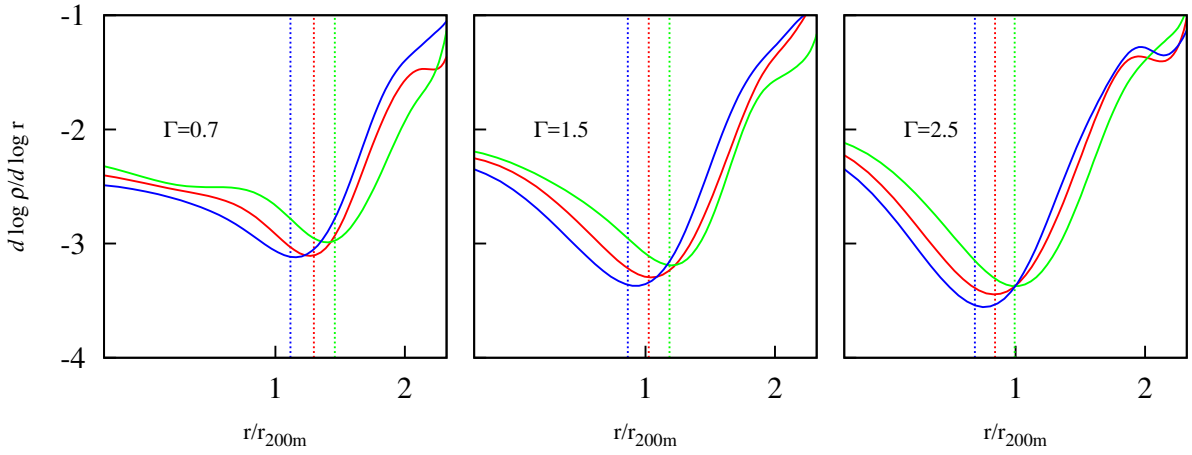

Figure 4.2: (Left) Local density slope as a function of r/r_{200} for stacked N-body halos at $z = 0$ with mass $M_{\rm vir} = 1-4\times10^{14}h^{-1}M_{\odot}$ for three different accretion rates. Different colors correspond to different values of the equation of state parameter, w. Blue, red and green correspond to $w = -0.5, -1, -2$ respectively. The vertical dashed lines shows the expected position of splashback from our toy model.

$P_{DE} = -w\rho$ and $w \neq 1$. The rate of expansion of the back ground universe is given by,

$$\frac{\ddot{a}}{a} = H_0\sqrt{\Omega_m a^{-3} + \Omega_{DE}a^{-3(1+w)}} \tag{4.3}$$

and the equation of motion of the shell is modified to

$$\ddot{r} = -\frac{GM}{r^2} + \frac{H_0^2}{2}(1+3w)r^{-2-3w}, \tag{4.4}$$

For comparison Fig 4.1 shows the dependence of splashback overdensity on the accretion rate for a ΛCDM universe and for a universe with $w = -0.7$. The difference in the enclosed overdensity at a given accretion rate between models of the universe with $w = -1.0$ and $w = -0.7$ becomes larger at low redshifts which is expected as Λ domination begins at late times. The overdensity at splashback is higher for higher $|w|$. This behavior can be understood by considering again the rate at which the universe expands between turnaround

and splashback. If we hold fixed the value of Ω_{DE} at 0.7 today, then for a universe where $-1/3 > w > -1$ dark energy dominates at an earlier epoch than it does for a $w = -1$ universe. However at the time of turn around Ω_{DE} is higher that what is was for a ΛCDM universe, and therefore the background universe dilutes faster than it would have for a universe with cosmological constant between the turnaround and splashback, making the overdensity larger at splashback. The opposite is true for $w < -1$.

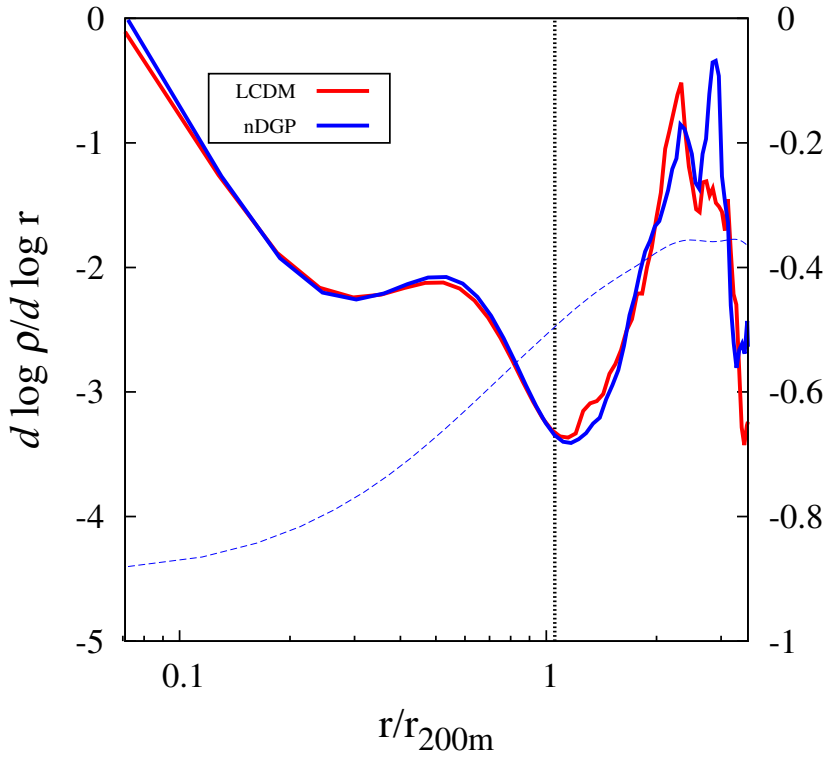

Figure 4.3: (Left y-axis) Local density slope as a function of r/r_{200m} for stacked N-body halos at $z = 0$ with mass $M_{\rm vir} = 1 - 4 \times 10^{14} h^{-1} M_\odot$ with average accretion rate $\Gamma = 1.5$. Different colors correspond to different cosmologies. The blue curve corresponds to nDGP with $H_0 r_c = 0.57$, and the red curve corresponds to ΛCDM. The vertical black dashed line shows the expected position of splashback for the accretion rate bin. The quantity ΔF shows the strength of the modfication as a function of distance from the centre of the halo.

To test the accuracy of our model we ran N-body simulations of cosmologies with different equation of state parameter for dark energy. For this purpose we modified the background evolution equations in Gadget2 to allow for varying w. We used 1024^3 particles in a 1 Gpc

h^{-1} box . The softening length was chosen to be a quarter of a scale radius for a halo with 1000 particles. [26], which is of the order of $1/30L/N$. We adopt the Planck cosmology for our simulations where $\Omega_m = 0.27$, $\Omega_L = 0.73$, $\Omega_b = 0.0469$, $h = 0.7$. Fig 4.2 shows the comparison of our predictions from the toy model to the N-body simulations. Our model correctly captures the movement of splashback with changing w. We use $w = -0.5$ and $w = -2$, to amplify the effect of changing the EoS.

Even though Fig 4.1 shows that the enclosed density changes by about 20% when w goes from -1 to -0.7, the change in the splashback radius is not as large, Δ_{encl} is a steeper function of the accretion rate, Γ than the splashback radius, r_{sp}. This shows that near the region of interest $w = -1$, the splashback radius is a weak function of w.

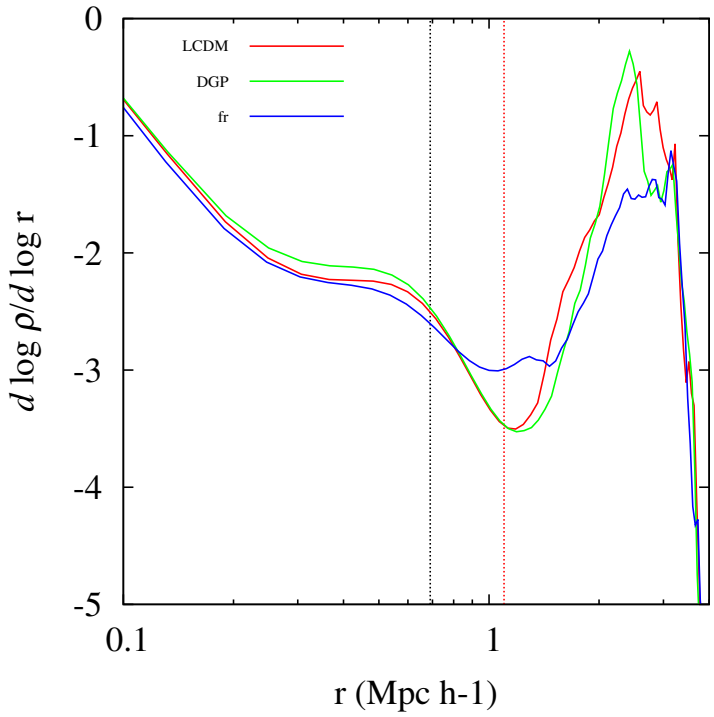

Figure 4.4: (Left) Local density slope as a function of r/r_{200m} for stacked N-body halos at $z = 0$ with mass $M_{\rm vir} = 1 - 4 \times 10^{14} h^{-1} M_\odot$. Different colors correspond to different cosmologies. The blue line corresponds to f(R) cosmology with $f_R = 5x10^{-4}$, the green line corresponds to Λ CDM and the blue line corresponds to nDGP with $H_0 r_c = 0.007$

4.3 Alternate models of Gravity

Modified gravity models have been invoked as an alternative to dark energy to understand the large scale accelerated expansion of the universe. In these models gravity is modified on large scales but on small scales, in higher density environments, general relativity must be restored to be consistent with stringent observational tests of GR from the solar system. Most theories therefore admit a nonlinear process or "screening mechanism" to suppress the modifications to gravity in high density regions. Therefore, transition regions between the two regimes, screened and unscreened are interesting for tests of modified gravity. Here we focus on the f(R) and the DvaliGabadadzePorrati(DGP) model that have two different classes of screening mechanisms, namely Chameleon screening and Vainshtein screening and see how they effect the splashback feature.

The modifications to gravity can be parametrized by an enhancement of the gravitational constant in the unscreened region by a factor of 4/3. If the transition region lies in the outskirts of a halo, during infall the particles are in a region of enhanced gravity, but during the course of their first orbit they are partly in the screened region of the halo. We might expect that the varying gravitational field during the orbit of a particle may induce significant displacement of the splashback radius. In the next section we briefly describe the gravity models and the simulations we use to test this effect.

4.3.1 nDGP-Vainshtein screening

DGP falls in the class of modified gravity theories that have an extra scalar degree of freedom, which mediates the modified gravitational force. The screening is achieved by non-linear self-couplings of the scalar field. Nonlinearity causes the gravitational fields of particles to interfere therefore in high density regions for collections of particles the deviation from GR are weakened compared to individual, isolated particles. This process is known as the Vainshtein mechanism. To study the effects to the outer density profile we choose

the nDGP model, i.e. the normal branch of the DGP theory. Unlike sDGP, which is the self-accelerating branch of DGP, this has the exact expansion history as ΛCDM, therefore we simulate this model to disentangle the effects of modified gravity. The Friedmann equation in the nDGP model is given by,

$$H^2 = -\frac{H_0}{r_c} + \frac{8\pi G\rho_m}{3} + \frac{8\pi G\rho_{dm}}{3} \tag{4.5}$$

where r_c is the scale at which gravity transitions from 5D on large scales to 4D on small scales. The background evolution is tuned to match the ΛCDM expansion. The Poisson equation and the scalar field equation are given by,

$$\nabla^2\Psi = \nabla^2\Psi_N + \frac{1}{2}\nabla^2\phi \tag{4.6}$$

$$\nabla^2\phi + \frac{r_c^2}{3\beta(a)a^2}\left[(\nabla^2\phi)^2 - (\nabla_i\nabla_j\phi)(\nabla^i\nabla^j\phi)\right] = \frac{8\pi G a^2}{3\beta(a)}\rho\delta \tag{4.7}$$

where ϕ is the scalar field Ψ is the Newtonian potential, $\Psi_N = 4\pi G\rho\delta$ is the Newtonian potential in GR, δ is the density contrast. And the parameter $\beta(a)$ is given by,

$$\beta(a) = 1 + 2Hr_c\left(1 + \frac{\dot{H}}{3H^2}\right) \tag{4.8}$$

As r_c becomes large the modifications to gravity become weaker and the Vainshtein screening mechanism becomes more efficient. In the spherically symmetric case, we can define a Vainshtein radius for a halo with an NFW profile. This is the radius the halo is screened and the Newtonian force is recovered. The Vainshtein radius depends on the mass of the halo and the cross-over scale r_c,

$$r_\star = \left(\frac{16Gm(r)r_c^2}{9\beta^2}\right)^{1/3} \tag{4.9}$$

The Poisson equation in modified gravity models become highly nonlinear with products

of the second-order derivatives of the scalar field, making them difficult and expensive to solve numerically. ECOSMOG-V [83] is the state of the art code to simulate cosmologies with modified gravity. It is an AMR code based on RAMSES that solves for the scalar field ϕ using the Newton-Gauss Siedel elimination method. For a detailed review of the code performance refer to [84, 83].

We have run N-body simulations with 512^3 particles on a 400 Mpch^{-1} starting with an initial redshift of $z = 49$, with initial conditions generated using N-GenIC [85]. We run these with the best-fit Plank cosmology parameters, $\Omega_m = 0.301$, $\Omega_\Lambda = 0.699$, $h = 0.677$, $n_s = 0.9611$. Of the three nDGP models simulated in [84], we simulate the one with the largest modification to gravity where, $H_0 r_c = 0.57$ to maximize it's effects on splashback. As the growth of structure in DGP is different from ΛCDM, we normalize the initial conditions of our simulations, such that σ_8 is the same for both the nDGP and the corresponding ΛCDM case. Fig.4.3 shows the comparison between the slopes of the density profile for cluster sized halos, stacked based on accretion rate, for halos in ΛCDM and nDGP with $H_0 r_c = 0.57$. This value for nDGP parameter was chosen such that the Vainshtein radius for cluster sized halos lies in the splashback region. The plot also shows strength of the modification to gravity in the halo, which is given by the ratio of the fifth force, $F_5 = 1/2\ d\phi/dr$ and the usual gravitational force, F_G. We plot,

$$\Delta F = \frac{F_5}{F_G \Delta_M} - 1 \tag{4.10}$$

Δ_M is the linear theory value of the ratio of the two forces, $1/3\beta$. ΔF approaches -1 in screened regions and 0 in unscreened regions. Fig 4.3 shows that the splashback is in the transition region. We find that there is no effect on the shape or location of the feature in the nDGP model. We also find that for group sized halos where the vainshtein radius is smaller than the splashback radius, there is no change in the splashback feature.

This result is somewhat surprising, given that the particles are transitioning from a region

of 4/3G to G in the course of their orbits. The halo potential should be growing differently in the modified gravity scenario,cha however one possible reason for the similarity of profiles may be the fact that comparing halos of similar accretion rates, negates the effect of the difference in the growth of halo potential. However, stacking simply on narrow mass bins does not create an effect either.

4.3.2 f(R)-Chameleon screening

Another commonly used modification to gravity is the $f(R)$ model. Here also the modification to gravity is mediated by a scalar field. Screening is achieved by nonlinear coupling between the scalar field and matter, making the mass of the scalar field very high in dense regions thus reducing its compton wavelength. This mechanism is known as Chameleon screening. In f(R) models the Einstein Hilbert action is modified by a general function of the scalar curvature R.

$$S = \int d^4x\sqrt{-g}\frac{R + f(R)}{16\pi G} \tag{4.11}$$

This introduces an additional degree of freedom as $f_R = df/dR$. The compton wavelength of the field is given by $\Lambda_c = \sqrt{3df_R/dR}$, and within the Compton wavelength gravity is modified by a factor of 4/3.

For our purposes we adopt the [86] f(R) model given by,

$$f(R) = -m^2\frac{c1(-R/m^2)^n}{c2(-R/m^2)^n + 1} \tag{4.12}$$

where n,c1,c2 are model parameters, $c_1/c_2 = 6\Omega_\Lambda/\Omega_m$ to match the ΛCDM background evolution, and $m = \Omega_m H_0^2$. The model is parametrized by the background value of the derivative of the the field, $|f_{R0}| = -nc_1/c_2^2[3(1 + 4\Omega_\Lambda/\Omega_m)]^{-(n+1)}$ [87].

The coupled Poisson equations in f(R) gravity are given by,

$$\nabla^2\phi = \frac{16\pi G a^2}{3}\delta\rho + \frac{a^2}{6}\delta R(f_R), \tag{4.13}$$

$$\nabla^2\delta f_R = -\frac{a^2}{3}[\delta R(f_R) + 8\pi G\delta\rho], \tag{4.14}$$

where ϕ is the potential, $\delta f_R = f_R(R) - f(\bar{R})$, R is the scalar curvature $\delta R = R - \bar{R}$ where the barred quantities are the background values.

As in the case for DGP, the coupled Poisson equations are much more difficult to solve than the linear Poisson equation in GR. We use ECOSMOG [83] to simulate f(R) universe. We run N-body simulations with 512^3 particles in a 400 Mpc h-1 from z=49 to z=0. We use $|f_{R0}| = 10^{-3}$, to maximize the effect. Much larger values of f_R will leave the entire halo unscreened and the dynamics will be similar to the GR case G enhanced by a factor of 4/3. The cosmological parameters are similar to the model adopted for the DGP model. $\sigma_8 = 0.94$ for $|f_{R0}| = 10^{-4}$, this is the value of σ_8 that all ΛCDM and DGP are adjusted to.

Observationally $|f_{R0}|$ is constrained to be less than 10^{-6}, we have run simulations with $|f_{R0}| = 10^{-4}$ and higher to enhance the effects of the modificiation to gravity gravity. Larger values of $|f_{R0}|$ leave cluster sized halos unscreened, and therefore there should be no effect on the dynamics of particle orbits barring an enhancement of gravity by a factor of 4/3. Fig 4.4 shows the slope of the density profile as a function of r for cluster sized halos stacked based on accretion rate. Again we do not see a significant effect on the location of the splashback radius in the case of $f(R)$ gravity.

4.3.3 Effect on subhalos

Apart from looking at dark matter particles we also looked at subhalos in different modified gravity simulations. The main motivation for this was the fact that in chameleon theories we may have small objects that are unscreened i.e the infalling galaxies may not be completely screened an therefore they may fall in at different velocities, therefore the dependence of

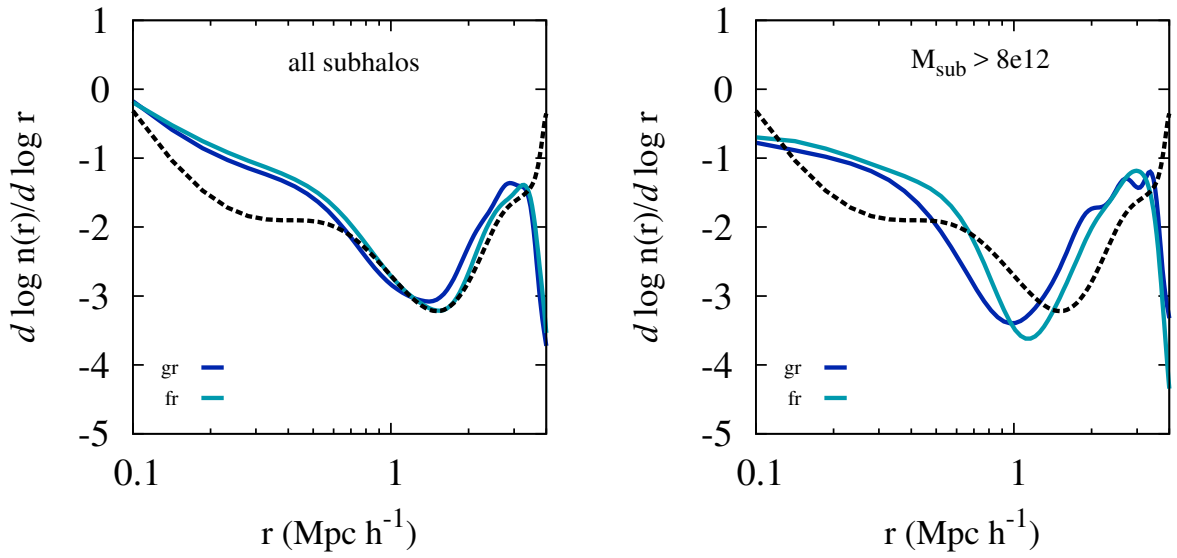

Figure 4.5: (Left) Local number density slope for subhalos as a function of r for stacked N-body halos at $z = 0$ with mass $M_{\rm vir} = 1 - 4 \times 10^{14} h^{-1} M_{\odot}$ in f(R) and GR. The black dashed line corresponds to splashback for DM particles.

splashback on the mass of the infalling subhalo may be different than in the Lambda CDM case. Attached is a plot made using data from Baojiu Li's simulations. These are for $f_R = 10^{-5}$, 1 Gpc h^{-1} boxes, I am looking at cluster sized host halos. For subhalos the resolution isn't great, we can only trust subhalos with masses greater that $8 \times 10^{12} M_{\odot} h^{-1}$ Fig 4.5 shows the comparison of splashback for subhalos in f(R) and GR.

4.4 Self-Interacting Dark matter

Dark matter self interactions have long been used to explain discrepancies between observations at small scales and CDM simulations. In general they naturally alter the structure of dark matter halos by producing cored density profiles and halos that are rounder in their

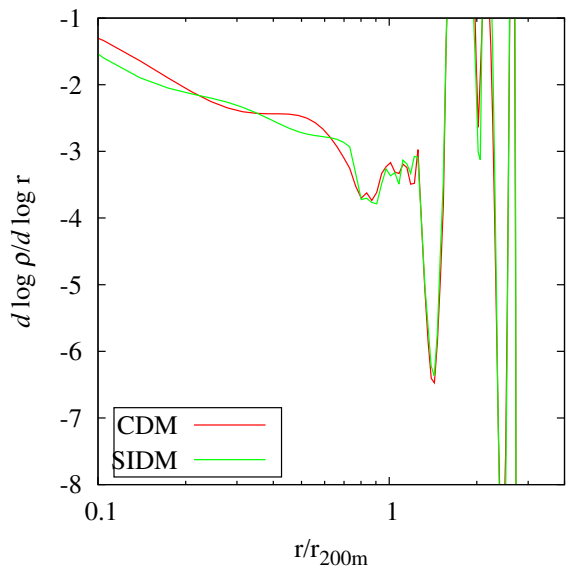

Figure 4.6: (Left) Local density slope as a function of r/r_{200m} at $z = 0$ for a halo with mass $M_{\rm vir} = 1.3 \times 10^{15} h^{-1} M_{\odot}$. The two colors show two different models for dark matter interactions, the two simulations begin from the same initial conditions.

central regions. Non-gravitational, self-interactions can cause particles to lose energy. Especially ones that have radial orbits and have traveled deep into the halo's potential. As a result of this loss of energy we may expect the particles may splashback at different locations after their first pericenter passage.

To begin with we consider hard-sphere isotropic, elastic scattering. We study simulations by James Bullock and Oliver Elbert, with interaction cross-sections of $\sigma = 1 cm^2/g$. These are zoom in cluster simulations with clusters of mass $M_{cluster} = 10^{15} M_{\odot} h^{-1}$ with a force resolution of 4kpc.. Fig.7.1 shows the slope as a function of radius for the cluster. The outer profile for the clusters look almost exactly similar to each other, the only differences arise in the central concentration of the halos. The location and shape of the splashback feature does not change. However this result is not surprising. In isotropic scattering at every interaction there is a large exchange of momentum, and particles are deviated off their original trajectory in some random direction. The particles with altered energy don't move coherently to create a density caustic. The only effect we might expect is a smearing

out of the splashback feature in SIDM halos for large enough cross sections. However, due to the large momentum exchange during interactions, the dark matter particles within subhalos often gain enough momentum to escape its potential causing subhalos to evaporate. The oberservation of subhalos in large clusters therefore has put stringent upper limits on isotropic scattering cross-section for self interactions, at these low cross sections no significant effect can be observed in the structure of the splashback feature in simulations.

The same momentum transfer cross-section can arise from having rare collisions with large momentum transfer or having frequent collisions with a small momentum transfer at each interaction. In the second scenario as particles have a high probability of interaction the effect of collisions can be described as a net drag force where the decceleration is given by,

$$\vec{f} = \frac{\sigma_T \rho v_{rel}^2}{2m_{DM}} \hat{v}_{rel} \tag{4.15}$$

where ρ is the ambient density of the medium through which the particle is moving, v_{rel} is the particle's relative velocity with the background and σ_T, is the integrated transfer cross-section given by,

$$\sigma_T = \int_0^1 d\theta_{cms}(1 - \cos\theta_{cms}) \frac{d\sigma}{d\Omega_{cms}} \tag{4.16}$$

where, θ_{cms} is the scattering angle in the centre of mass frame. The cross section is highly peaked in the forward direction. These are small angle scattering with low momentum transfer, therefore the particles in their orbit are not thrown out of their path in a random direction. A cumulative effect of many interactions leads to a net decceleration and a loss in energy, therefore the particles are expected to splashback at a smaller radius than they do in cold dark matter scenarios for such anisotropic self interactions.

Anisotropic interactions warrant a method of simulation different from the simulations of isotropic cross-sections in [88]. As preliminary tests we implement this interaction using

a momentum-conserving scheme on a grid-based PM N body code and run simulations for different values of σ_T/m_{DM}. As expected, we find that the splashback moves inwards as a function of the transfer cross-section. However, these are preliminary simulations that are of low resolution and are not converged. To this end we are currently implementing this interaction using L-Gadget to study the signatures of anisptropic scattering on halo structures.

4.5 Discussion

In this paper we have looked at the space of theoretical models beyond ΛCDM and seen it's effect on the splashback radius. It appears that the splashback radius is a scale in the halo that is surprisingly robust in different cosmological models as a probe for the accretion rate of a halo. It shows a weak dependence on the equation of state parameter. The equation of state parameter would have to vary dramatically to reproduce the 20% offset detected in More et al. 2016 [69]. The splashback feature in dark matter particles also does not show very strond dependence on the model for gravity. Both Chameleon and Vainshtein theories do not show a movement in the position by there may be some change in the shape of the feature which is a topic for further investigation.

Intriguingly the splashback radius for subhalos in $f(R)$ theories seems to effect the location of splashback. While the subhalos compared in the $f(R)$ and GR simulations have masses that are likely to experience dynamical friction the size of the effect seems significantly different in the two cases.

Isotropic self-interacting dark matter also does not effect splashback. The only mechanism that seems te be a plausible candidate to create differences in splashback positions are anisotropic dark matter self interactions a topic which is currently being investigated.

The splashback radius is emerging as a novel tool for understanding halo formation and growth of structure. More recently the splashback radius has also been detected in DES

data. In DES, this feature is not only detected in the galaxy distribution within clusters but also for the first time in its stacked lensing profile. We are also working closely with DES group helping in the interpretation and comparison of the data with theoretical predictions from simulations and simple toy models.

Chapter 5

Three point galaxy-galaxy lensing as a probe for dark matter halo shapes

We propose a method to measure the ellipticities of dark matter halos using the lens-shear-shear 3-point correlation function. This method is immune to effects of galaxy-halo misalignments that can potentially limit 2-point galaxy-galaxy lensing measurements of halo anisotropy. Using a simple model for the projected mass distributions of dark matter halos, we construct an ellipticity estimator that sums over all possible triangular configurations of the 3-point function. By applying our estimator to halos from N-body simulations, we find that systematic errors in the recovered ellipticity will be at the $\lesssim 5\%$ fractional level. We estimate that future imaging surveys like LSST will have sufficient statistics to detect halo ellipticities using 3-point lensing. [1]

5.1 Introduction

In the cold dark matter model of cosmological structure formation, galaxies are believed to form inside of virialized objects called dark matter halos. The properties of these halos, like their internal structure or abundance, are related to the background cosmology and to the physics of dark matter particles. One example of this is the ellipticity of dark matter halos. In CDM cosmologies, halos are found to be triaxial, with axis ratios of the order of 0.5:1, with a significant scatter from object to object [89, 90, 91, 92]. Alternative models, like self-interacting dark matter (SIDM) can produce significantly different shapes. Pure SIDM

[1] This chapter was previously published in the Journal of Cosmology and Astroparticle Physics as S. Adhikari, C. Y. R. Chue and N. Dalal, Three-point galaxy-galaxy lensing as a probe of dark matter halo shapes, JCAP 1501 (2015) 009, [1407.1128].This chapter matches the published version.

simulations generally produce halos with rounder shapes than CDM simulations [93, 94, 88], although the effects of baryons can modify these results [95].

Therefore, measurements of the shapes of dark matter halos may be used to probe the nature of dark matter. Accordingly, multiple groups have attempted to measure halo shapes using a variety of probes. In our own Galaxy, several groups have attempted to model the dynamics of the Sagittarius tidal stream in order to infer the underlying shape of the Milky Way's halo [96, 97, 98, 99, 100]. In other galaxies, halo shapes have been probed using strong lensing and stellar dynamics [101, 102] on small scales, and satellite dynamics on larger scales [103].

Another probe of dark matter halo properties is weak gravitational lensing. The average radial profiles of dark matter halos have been inferred with high precision through measurement of the two-point cross-correlation between galaxies and tangential shear, called galaxy-galaxy lensing [104, 105, 106]. Circularly averaged statistics are insensitive to halo ellipticity, but in principle, anisotropy could be constrained by measuring shear not only as a function of radius r, but position angle θ as well. Unfortunately, because dark matter halos are dark, we cannot determine the orientations of halos, making it impossible to measure shear profiles as a function of position angle relative to the halo principal axes. We can, however, measure shear as a function of the position angle relative to the lens galaxies' principal axes. If halos are perfectly aligned with their central galaxies, then such measurements may be used to determine the average halo ellipticity. This is the approach that has been used by most previous work [107, 108, 109, 110]. This previous work, however, has yielded inconclusive results. For example, [110] report an average projected ellipticity of $e = 0.38 \pm 0.26$, which is consistent both with CDM predictions and with completely isotropic halos. Currently, statistical errors are a principal limitation of this measurement, but with the vastly increased sample sizes provided by future imaging surveys like LSST, the statistical errors may be reduced sufficiently to detect the expected signal. More worryingly, this method is likely limited by potentially severe systematic effects. First, the assumption

that galaxies and their halos are perfectly aligned may be unrealistic [111]. [112] has argued that significant misalignments between galaxies and halos may be quite typical; the median misalignment angle in their simulations was $\sim 38°$. Random misalignments act to wash out the halo anisotropy signal from galaxy-galaxy lensing. Even worse, they complicate the interpretation of any measured anisotropy signal. Without knowledge of the misalignment distribution, we will not know how to translate stacked lensing signals into constraints on halo axis ratios. This effect is also not the only possible systematic. For example, if lens galaxies and background source galaxies are both lensed by foreground structures, this common lensing will tend to align their observed shapes, thereby contaminating the halo anisotropy signal [113]. Because of these systematic limitations, an alternative approach for measuring halo shapes with galaxy-galaxy lensing may be required – ideally, a method that does not require galaxies to align with their host halos. Such an approach is suggested by the recent work of [114], who find that halo ellipticities affect galaxy-galaxy lensing 3-point correlation functions. Although most previous work on galaxy-galaxy lensing has focused on 2-point statistics, higher order correlation functions are now becoming measurable in modern imaging surveys [115, 116]. In this paper, we explore how halo ellipticities may be determined from measurements of the galaxy-shear-shear 3-point function.

5.2 Mass model

The 3D density profiles of halos in dissipationless CDM simulations have axis ratios of order $q \approx 0.5$, slowly varying with radius [90, 91]. Similarly, the 2D projected surface density Σ is anisotropic, with axis ratios closer to $q \sim 0.7$, again slowly increasing with radius. Because q is nearly constant with radius, we can write $\Sigma \propto R^{-\eta}$, where $R = (x^2 + y^2/q^2)^{1/2}$ is an ellipsoidal radial coordinate, and η is the logarithmic slope of the projected surface density. We will find it convenient below to work with the multipole moments of the density profile.

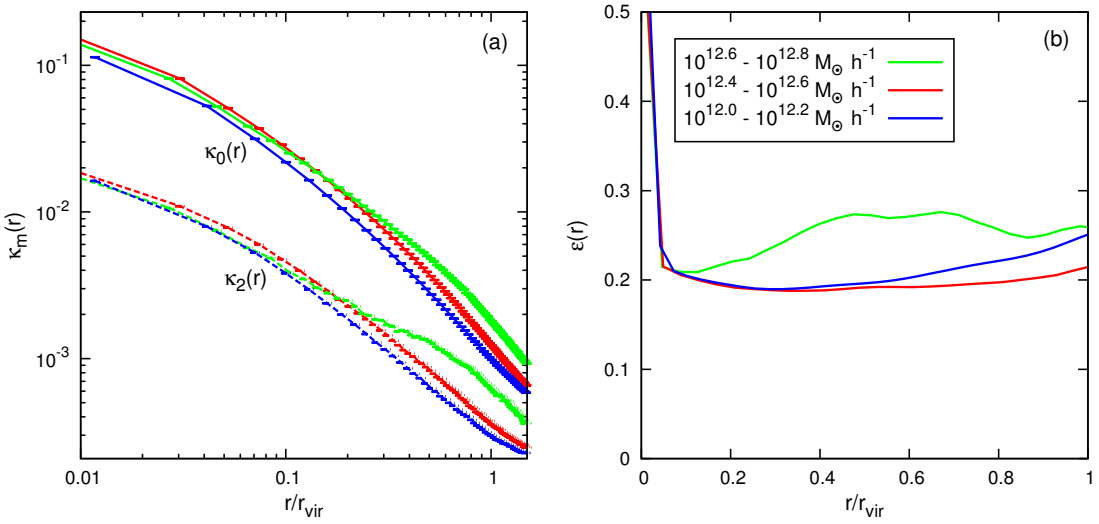

Figure 5.1: (a): Plot of the multipole moments of stacked halos. The solid curves show the isotropic component (monopole, κ_0) of the surface density profile and the dashed curves show the $\cos 2\theta$ component (quadrupole, κ_2). The convergence κ is proportional to surface density Σ. (b): Radial dependence of ellipticity, which we define as $\varepsilon(r) \equiv \kappa_2/(\eta\,\kappa_0)$, for three different mass bins. The blue, red and green colors correspond to three different mass bins. Note that, although the multipole moments vary by orders of magnitude, the ellipticity remains nearly constant across much of the range of interest.

In the limit of small ellipticity, we can write the multipole expansion of Σ in terms of q,

$$\begin{aligned}\Sigma(r,\theta) &\propto r^{-\eta}\left[1+\varepsilon\,\eta\cos 2\theta+\mathcal{O}(\varepsilon^2)\right] \\ &\equiv \Sigma_0(r)+\Sigma_2(r)\cos 2\theta+\ldots \end{aligned} \tag{5.1}$$

where the multipole $\Sigma_m(r)$ is the coefficient of the $e^{im\theta}$ component of the azimuthal behavior, and we use $\varepsilon = (1-q^2)/\left[2(1+q^2)\right]$ to parameterize the ellipticity. For the typical axis ratios found in simulated halos, $\varepsilon \sim 0.2$, so we neglect higher order terms in the expansion.

We therefore model the mass distributions of halos as the sum of a monopole and quadrupole, and further assume that

$$\varepsilon \approx \frac{\Sigma_2(r)}{\eta(r)\Sigma_0(r)} \tag{5.2}$$

where $\eta = d\log\Sigma_0/d\log r$. In Figure 5.1, we plot ε as defined in Eqn. (5.2), measured from stacked profiles of projected halos taken from the Bolshoi simulation [39]. We measure multipole moments from the particle positions, using

$$\Sigma_m(r) = \sum_i \frac{m_p\delta(r-r_i)\,e^{im\theta_i}}{2\pi r_i}, \tag{5.3}$$

where m_p is the particle mass, and r_i and θ_i are the radius and azimuthal angle for particle i. After computing $\Sigma_0(r)$ and $\Sigma_2(r)$ for each halo, we then stack the halos to compute $\langle\Sigma_0\rangle(r)$ and $\langle|\Sigma_2|\rangle(r)$, and then ε. As expected, the ellipticity is fairly constant with radius, except very near the halo center where $\eta = d\log\Sigma_0/d\log r \to 0$. Because ε is nearly constant with radius, then the radial dependence of the quadrupole may be predicted from the monopole, whose mean $\langle\Sigma_0(r)\rangle$ may be determined from real galaxy halos using galaxy-galaxy lensing 2-point statistics. Specifically, the mean tangential shear $\langle\gamma_+\rangle$ profile around halos is related

to the mean monopole via [117]

$$\langle \gamma_+ \rangle = \frac{\Delta\Sigma(r)}{\Sigma_{\rm crit}} = \frac{\bar{\Sigma}_0(<r) - \Sigma_0(r)}{\Sigma_{\rm crit}}, \tag{5.4}$$

where the lensing critical density $\Sigma_{\rm crit}$ is defined as

$$\Sigma_{\rm crit} = \frac{c^2}{4\pi G}\frac{D_s}{D_{ds}D_d}, \tag{5.5}$$

and D_d and D_s are the angular diameter distances to the lens and the source respectively, while D_{ds} is the angular diameter distance from the lens to the source. Eqn. (5.4) can be inverted (up to a mass-sheet degeneracy) to obtain the mean monopole profile $\Sigma_0(r)$ from the observed mean tangential shear profile $\langle\gamma_+\rangle(r)$ via

$$\begin{aligned} \frac{\Sigma_0(r) - \Sigma_0(r_{\rm max})}{\Sigma_{\rm crit}} &= 2\int_r^{r_{\rm max}} \langle\gamma_+\rangle(R)\frac{dR}{R} \\ &\quad - \left[\langle\gamma_+\rangle(r) - \langle\gamma_+\rangle(r_{\rm max})\right]. \end{aligned} \tag{5.6}$$

Here, $r_{\rm max}$ is the largest radius over which the stacked tangential shear profile $\langle\gamma_+\rangle$ has been measured.

For circularly symmetric lenses, the tangential shear is the only nonzero component of the shear. When the surface density is anisotropic, however, the other component ($\gamma_\times$) becomes nonzero. In the same way that we can decompose the surface density into angular multipoles $\Sigma_m(r)$, we can similarly decompose the shear into multipoles $\boldsymbol{\gamma}^{(m)}(r)$. The relation between the density and shear multipoles is straightforward. For convenience, we follow conventional notation and define the convergence as $\kappa = \Sigma/\Sigma_{\rm crit}$, and define a 2D lensing potential ψ via

$$\nabla^2\psi = 2\kappa \tag{5.7}$$

where the gradient is with respect to sky coordinates. In polar coordinates, this equation

becomes

$$\kappa(r,\theta) = \frac{1}{2}\left[\frac{\partial^2}{\partial r^2} + \frac{1}{r}\frac{\partial}{\partial r} + \frac{1}{r^2}\frac{\partial^2}{\partial\theta^2}\right]\psi. \tag{5.8}$$

The two components of the shear are given by

$$\gamma_+ = \left[-\frac{\partial^2}{\partial r^2} + \frac{1}{r}\frac{\partial}{\partial r} + \frac{1}{r^2}\frac{\partial^2}{\partial\theta^2}\right]\psi \tag{5.9}$$

$$\gamma_\times = \left[-\frac{2}{r}\frac{\partial^2}{\partial r\partial\theta} + \frac{2}{r^2}\frac{\partial}{\partial\theta}\right]\psi \tag{5.10}$$

Next, let us decompose these fields into angular multipoles

$$\begin{aligned}\psi(r,\theta) &= \sum_{m=-\infty}^{\infty}\psi_m(r)e^{im\theta} \\ \kappa(r,\theta) &= \sum_{m=-\infty}^{\infty}\kappa_m(r)e^{im\theta}.\end{aligned} \tag{5.11}$$

Explicitly,

$$\begin{aligned}m=0: \quad \kappa_0(r) &= \frac{1}{2\pi}\int_0^{2\pi}\kappa(r,\theta)d\theta \\ m\geq 1: \quad \kappa_m(r) &= \frac{1}{\pi}\int_0^{2\pi}\kappa(r,\theta)\cos m\theta\, d\theta.\end{aligned} \tag{5.12}$$

Solving the 2-d Poisson Eqn. (5.8), we obtain the multipole moments of ψ,

$$\begin{aligned}\psi_0(r) &= \ln r\int_0^r r'\kappa_0(r')dr' + \int_r^\infty r'\ln r'\kappa_0(r')dr' \\ \psi_m(r) &= -\frac{1}{2m}\left[r^{-m}\int_0^r r'^{(m+1)}\kappa_m(r')dr'\right. \\ &\qquad \left. + r^m\int_r^\infty r'^{(1-m)}\kappa_m(r')dr'\right].\end{aligned} \tag{5.13}$$

Then, using Eqns. (5.9) and (5.10), we may obtain the multipole moments of the two shear components. Because we keep only $m = 0$ and $m = 2$, and because we assume that

$\kappa_2(r) = \varepsilon\,\eta(r)\,\kappa_0(r)$, we have

$$\gamma_+^{(0)}(r) = \frac{2}{r^2}\int_0^r r'\kappa_0(r')dr' - \kappa_0(r) \tag{5.14}$$

$$g_+(r) = \left[-\kappa_0(r)\eta(r) + \frac{3}{r^4}\int_0^r r'^3\kappa_0(r')\eta(r')dr' + \int_r^\infty \frac{\kappa_0(r')\eta(r')}{r'}dr'\right] \tag{5.15}$$

$$g_\times(r) = \left[\frac{3}{r^4}\int_0^r r'^3\kappa_0(r')\eta(r')dr' - \int_r^\infty \frac{\kappa_0(r')\eta(r')}{r'}dr'\right], \tag{5.16}$$

where we have defined, for the purpose of convenience, the functions g_+ and $g_\times$ such that the quadrupole components of the shear are $\gamma_+^{(2)} = \varepsilon\,g_+(r)\cos 2\theta$ and $\gamma_\times^{(2)} = \varepsilon\,g_\times(r)\sin 2\theta$. Note that, by definition, $\gamma_\times^{(0)} = 0$.

Given this model for the mass distributions of lenses, we can predict the shear at all locations around the lenses. The one unknown parameter is the ellipticity ε, which defines the amplitude of the quadrupole moment κ_2 in terms of the monopole moment κ_0, which we assume may be determined using Eqn. (5.6). Because we have an expression for the shear at all locations, we can construct an estimator for the quantity ε.

5.2.1 Three-Point Estimator

As discussed in §6.1, [114] have shown that lensing 3-point functions are sensitive to halo ellipticities. However, they also show that lensing 3-point functions are also sensitive to many other terms, making it difficult to disentangle the signal in the bispectrum generated by halo ellipticity. Fortunately, given our model for halo mass distributions, it is straightforward for us to construct an estimator to measure halo ellipticity from lensing correlation functions. Following [114], we focus on the lens-shear-shear 3-point function. Measurement of this correlation function involves stacking the shear measured from pairs of source galaxies behind

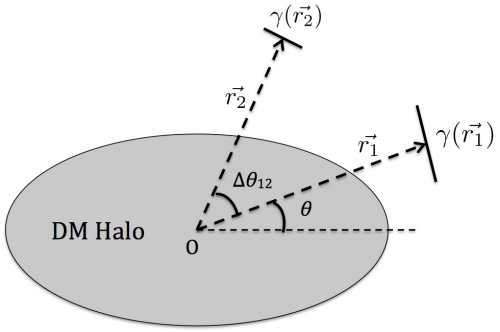

Figure 5.2: Lens-shear-shear three point correlation function. We correlate the shear at sky positions $\vec{r}_1$ and $\vec{r}_2$ relative to foreground lens galaxies, and construct an estimator summing all such triangular configurations in the sky.

foreground lens galaxies. Because the number density of source pairs is low, especially at the small radii of interest for measuring internal halo properties ($r < r_{\rm vir}$), we assume that shape noise in the source galaxies dominates measurement uncertainties. That is, we neglect the signal covariance compared to Poisson fluctuations in source counts. Because Poisson noise is white noise, the optimal estimator is then simply proportional to the expected signal from our model.

We therefore estimate the average lens ellipticity by summing over all lens-source-source triangles, weighting each triangle with a filter $\mathbf{F}$ that is given by the *predicted* model shear for each configuration of galaxies. Figure 5.2 illustrates the geometry on the sky. Suppose that we have measurements of the shear at positions $\vec{r}_1$ and $\vec{r}_2$ relative to the center of the lens halo. When we sum over all possible $\vec{r}_1$ and $\vec{r}_2$, the filter which weights each triangle is $\mathbf{F}(\vec{r}_1, \vec{r}_2) \propto \boldsymbol{\gamma}^{(2)}(\vec{r}_1) \otimes \boldsymbol{\gamma}^{(2)}(\vec{r}_2)$. Because the orientation angle of the lens halo is unknown, the filter must depend on the relative position angle of the sources, not their absolute position angles: $\mathbf{F}(\vec{r}_1, \vec{r}_2) = \mathbf{F}(|\vec{r}_1|, |\vec{r}_2|, \Delta\theta_{12})$. We compute $\mathbf{F}$ by averaging all possible triangles with one vertex at the center of the lens, and a constant opening angle, $\Delta\theta_{12}$, between position vectors to the lensed galaxies, of magnitude $|\vec{r}_1|$ and $|\vec{r}_2|$ (see Fig. 5.2). Since each shear has

2 components, the filter $\mathbf{F}$ is a 2×2 matrix, with components

$$\begin{aligned} F_{ij}\left(r_1, r_2, \Delta\theta_{12}\right) &= \langle g_i(\vec{r}_1) g_j(\vec{r}_2)\rangle \\ &= \frac{\int r_1' r_2' dr_1' dr_2' d\theta_1' d\theta_2' g_i(\vec{r}_1) g_j(\vec{r}_2) \delta_{r_1'} \delta_{r_2'} \delta_{\Delta\theta_{12}'}}{\int r_1' r_2' dr_1' dr_2' d\theta_1' d\theta_2' \ \delta_{r_1'} \delta_{r_2'} \delta_{\Delta\theta_{12}'}}, \end{aligned} \tag{5.17}$$

where indices i, j run over $+, \times$, and we define $\Delta\theta_{12} = \theta_2 - \theta_1 = \cos^{-1}(\vec{r}_1 \cdot \vec{r}_2 / r_1 r_2)$, along with $\delta_{r_\alpha'} \equiv \delta(r_\alpha' - r_\alpha)$ and $\delta_{\Delta\theta_{12}'} \equiv \delta(\Delta\theta_{12}' - \Delta\theta_{12})$. The integral in (5.17) covers the projected area in the sky, where r ranges from some $r_{\rm min}$ to $r_{\rm max}$, and θ ranges from 0 to 2π. Simplifying using the δ functions, we obtain

$$\begin{aligned} F_{++} &= \frac{1}{2} g_+(r_1) g_+(r_2) \cos 2\Delta\theta_{12} \\ F_{+\times} &= \frac{1}{2} g_+(r_1) g_\times(r_2) \sin 2\Delta\theta_{12} \\ F_{\times+} &= -\frac{1}{2} g_\times(r_1) g_+(r_2) \sin 2\Delta\theta_{12} \\ F_{\times\times} &= \frac{1}{2} g_\times(r_1) g_\times(r_2) \cos 2\Delta\theta_{12} \end{aligned} \tag{5.18}$$

Eqns. (5.18) specify the elements of the filter weighting each possible triangle in the 3-point correlation function. We then evaluate our estimator by summing over all triangles, weighting the shear by $\mathbf{F}$. Explicitly, we evaluate

$$f_{\rm obs} = \langle \boldsymbol{\gamma}(\vec{r}_1) \cdot \mathbf{F}(r_1, r_2, \Delta\theta_{12}) \cdot \boldsymbol{\gamma}(\vec{r}_2) \rangle \,, \tag{5.19}$$

where the expectation value implies averaging over all possible $\vec{r}_1$ and $\vec{r}_2$. Note that, because of the angular dependence of $\mathbf{F}$, Eqn. (5.19) is only sensitive to the quadrupolar component of the shear.

In order to translate $f_{\rm obs}$ into an estimate for the ellipticity ε, we need to know what result Eqn. (5.19) will give as a function of ε. We can compute this by inserting the predicted

model shear into the equation. Specifically, let us define

$$
\begin{aligned}
f_{\rm model} &= \langle \boldsymbol{g}(\vec{r}_1) \cdot \mathbf{F} \cdot \boldsymbol{g}(\vec{r}_2) \rangle \\
&= \frac{1}{2}\Big\langle g_+^2(r_1) g_+^2(r_2) \cos 2\theta_1 \cos 2\theta_2 \cos 2\Delta\theta_{12} \\
&\quad + g_+^2(r_1) g_\times^2(r_2) \cos 2\theta_1 \sin 2\theta_2 \sin 2\Delta\theta_{12} \\
&\quad - g_\times^2(r_1) g_+^2(r_2) \sin 2\theta_1 \cos 2\theta_2 \sin 2\Delta\theta_{12} \\
&\quad + g_\times^2(r_1) g_\times^2(r_2) \sin 2\theta_1 \sin 2\theta_2 \cos 2\Delta\theta_{12} \Big\rangle \\
&= \frac{1}{2}\left\{ \frac{\pi}{A} \int_{r_{\rm min}}^{r_{\rm max}} \left[g_+^2(r) + g_\times^2(r) \right] r dr \right\}^2 \\
&= \frac{1}{2}\left\{ \frac{\int_{r_{\rm min}}^{r_{\rm max}} \left[g_+^2(r) + g_\times^2(r) \right] r dr}{r_{\rm max}^2 - r_{\rm min}^2} \right\}^2 .
\end{aligned}
\tag{5.20}
$$

Then

$$
\varepsilon = \sqrt{\frac{f_{\rm obs}}{f_{\rm model}}} \tag{5.21}
$$

This defines our estimator for the ellipticity ε. To reiterate, the ingredient in our expression is the radial profile of the average monopole density profile $\langle \kappa_0 \rangle(r)$, which may be reconstructed from the stacked tangential shear profile $\langle \gamma_+ \rangle(r)$. Given $\kappa_0(r)$, we may then determine the functions g_+ and $g_\times$ which enter the estimator. In the next section, we apply this estimator to samples of halos from N-body simulations, to gauge how well we can measure halo ellipticities for realistic objects.

5.3 Results

In §5.2, we proposed a 3-point estimator for halo anisotropy. In this section, we assess how well this estimator measures average halo ellipticities. First, we use simulated halos from cosmological N-body simulations to quantify systematic errors caused by the fact that the structure of realistic halos will not be as simple as our monopole+quadrupole mass model.

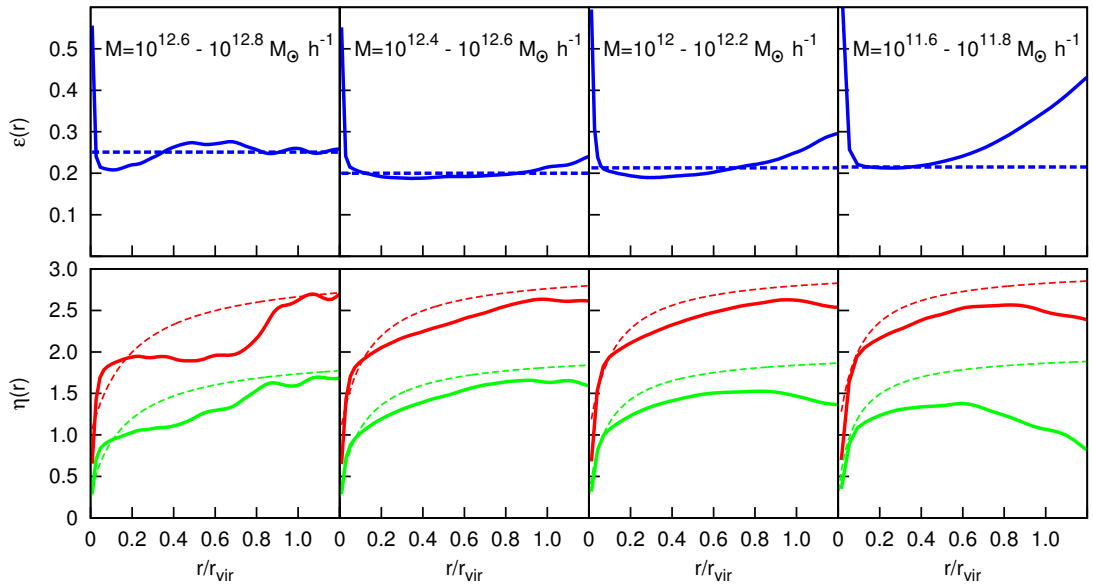

Figure 5.3: The top panels show the comparison between the average ellipticities of halos in various mass bins (solid curve), compared to the ellipticity determined from the 3-point estimator (dashed line). The bottom panel shows the local slope of the isotropic component (monopole) of the halos. The red curve corresponds to the smoothed slope of the 3D profile, and the green curve corresponds to the local slope of the projected 2D profile. The dashed curves show the slope of the NFW profile in 2D and 3D for reference. These slopes were measured from the stacked profiles after they were smoothed using a 6th order Savitzky-Golay filter over 17 nearest bins [5]. In the low mass bins, we observe significant departures from NFW slopes at large radii, possibly indicating the effects of nearby halos.

Secondly, we quantify the statistical error associated with the finite number of lens-source-source triples. Because each source galaxy provides an extremely noisy estimate of the shear, large numbers of triples are required to suppress this statistical shape noise.

5.3.1 Comparison with N-body simulations

We have applied our estimator (Eqn. 5.19) to halos from the publicly available Bolshoi simulation [39]. Using the BDMW catalog provided by the MultiDark database [2], we selected halos with virial masses in the range $10^{11.7} - 10^{12.7} M_{\odot} h^{-1}$. We downloaded particles within $5r_{\rm vir}$ of the halo center, to account for the mass within the halo as well as the nearby neighborhood. For each halo, we construct three projections, along the simulation box axes, to construct convergence and shear maps. From these shear maps, we then apply our estimator to measure the halo ellipticity ε. Figure 5.3 shows the results of our measurement across several mass bins. For comparison, the figure also plots the ellipticity directly measured from the projected mass profiles. In all cases, we find good agreement, despite several potential systematics discussed below.

First, our mass model assumes that ellipticity ε is constant with radius, meaning that the shape of the quadrupole $\kappa_2(r)$ of the mass distribution may be determined from the shape of the monopole profile $\kappa_0(r)$. For individual galaxies, the mass distributions are unknown. Galaxy-galaxy lensing can be used to reconstruct the mean monopole profile $\langle\kappa_0\rangle(r)$, but individual halos will have radial profiles that vary from the mean. Because our estimator is not linear in the shear, this scatter in radial profiles can bias our measurement. To estimate the size of this potential bias, we generated artificial halos with radial profiles consistent with the Bolshoi halos (i.e. same $M_{\rm vir}$ and $c_{\rm vir}$) but with specified values of ε. For the range of concentrations found in the mass range we have considered, we find a *fractional* bias in the reconstructed ε of $\sim 3 - 6\%$.

A second potential source of systematic errors arises from projections of other halos. Our

[2] http://hipacc.ucsc.edu/Bolshoi/MergerTrees.html

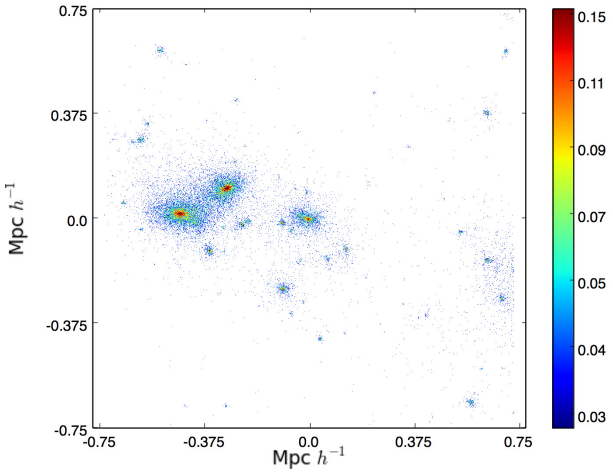

Figure 5.4: Example of line of sight projection effects. The halo at the origin has massive neighbors projecting nearby, which generate a large quadrupole moment that is unrelated to the halo's own ellipticity. Colors correspond to convergence κ, for a lens redshift of $z_l = 0.3$ and source redshift of $z_s = 0.5$.

mass model assumes that all shear is generated by the halos hosting the stacked galaxies. In reality, however, not all halos are isolated: other objects can project near the objects we are stacking and contaminate our measurement. Figure 5.4 shows one such example. Such projections can produce very large quadrupoles (and other multipoles) near certain halos, and because our estimator is not linear in the shear, this contamination can bias our results.

In general, there are two types of projections relevant to our measurement: galaxies that are correlated with the foreground lenses, and uncorrelated galaxies that randomly project into the line of sight. It is straightforward to correct for the uncorrelated projections. We could, for example, simply stack on random sky points instead of lens galaxies, and subtract this from our estimator. Mitigating the effects of correlated structures is not as easy. Perhaps the simplest approach would be to stack only galaxies that are relatively isolated, i.e. galaxies that are clearly central galaxies (not satellites), and that have no comparably bright galaxies nearby the line of sight. Such an approach should remove much of the contamination from nearby, correlated structures, but may not remove the contamination completely. Therefore, we need to estimate the effects of such contamination.

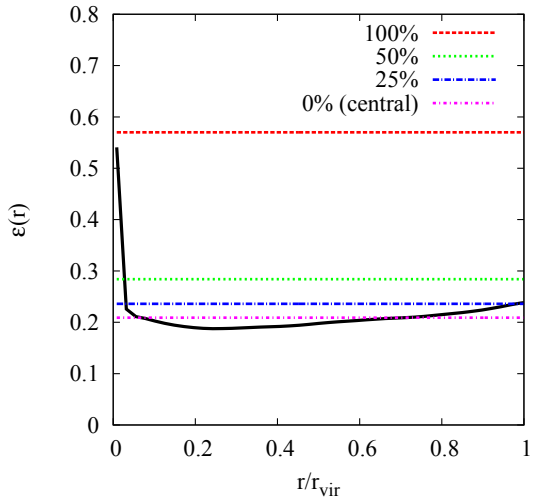

Figure 5.5: Effect of including satellites (subhalos) in our sample. The black solid curve shows the average ellipticity of halos estimated from N-body simulations in the mass bin $10^{12.4} - 10^{12.6} M_{\odot} h^{-1}$ using central galaxies only. The dashed lines show the ellipticity determined by the three-point estimator, applied to samples with various degrees of contamination by satellites. If satellites are not excluded (red line), the estimated ellipticity is significantly biased. Removing the satellites in the most dense environments eliminates much of the bias.

The largest source of contamination from correlated structures comes from satellite galaxies. Our estimator assumes that the lens galaxies are central galaxies within their halos, however a large fraction of galaxies ($\sim 20\%$) will be satellites living in massive hosts like clusters or groups. The quadrupole moments around satellite galaxies are much larger than those near central galaxies. To estimate this effect, we use subhalo abundance matching to find subhalos which could host galaxies that are similar to the central galaxies in our sample. We use the Rockstar catalog from MDR1 and find all halos and subhalos with similar $V_{\rm acc}$, the circular velocity at time of accretion. For objects with $V_{\rm acc} \approx 245$km/s, about 20% were subhalos rather than isolated halos. When we apply our estimator to the full sample of halos and subhalos, we find a large bias in the recovered ellipticity, $\varepsilon \approx 0.6$ instead of 0.2, as shown in Figure 5.5. Therefore if uncorrected, satellite contamination would significantly compromise our ability to measure halo ellipticity.

However, most of the contamination arises from satellites in the most massive hosts, and those satellites are the easiest to identify as satellites, since their local neighborhoods

have a large galaxy overdensity. Removing those objects should therefore be relatively straightforward. Figure 5.5 shows how the contamination is reduced if we are able to remove various fractions of the satellite population. Here, we have ranked the satellites based on local overdensity. Removing 50% of the satellites removes the vast majority of the contamination, while removing 75% of the satellites gives a recovered ellipticity very close to the ellipticity for no satellites at all. Therefore, even a crude identification of satellite galaxies should suffice to eliminate most of the potential contamination.

The other type of contamination to consider is that from nearby halos. Fortunately, it appears that any bias due to projections of nearby correlated halos may not be large. In our calculations, we have not corrected for projections of nearby halos in any way. Our measurement is therefore contaminated by projections of other halos within 5 $r_{\rm vir}$ (as in Figure 5.4). Arguably, this should account for most of the correlated objects. The galaxy auto-correlation function behaves close to $\xi(r) \propto r^{-2}$ in 3D [118], so the number of galaxies with 3D radius $r > 5r_{\rm vir}$ that project onto small radius should be about $\sim 1/5$ of the number of galaxies with 3D radius $r > r_{\rm vir}$ projecting onto small radius. Because we have extracted particles out to $5r_{\rm vir}$, we should account for about $\sim 80\%$ of the correlated projections.

Our calculations should therefore include most of the effect of projections of correlated structure, and as Figure 5.3 illustrates, the effect of those projections on the stacked profiles of central galaxies is likely to be small. Only in the lowest mass bin ($M \approx 10^{11.7} M_{\odot} h^{-1}$) do we observe any effects of the 2-halo term, and even there the recovered ε from the 3-point estimator is consistent with the halo ellipticity measured over the radial range where the 1-halo term is dominant. Nevertheless, when measuring halo ellipticity for real lenses, it will be important to restrict the analysis to the regime where the 1-halo term dominates, which may be determined by modeling the stacked tangential shear profile $\langle \gamma_+ \rangle$.

Another potential source of systematic error can arise due to the 'twisting' of halos. It is known that the principal axes of the isodensity surfaces in N-body halos are not constant with radius, but instead twist in orientation between small radii and large radii. Our simplistic

mass model does not account for twisting of the principal axes, so a significant twisting could bias our results. To quantify how much twist we can tolerate, we created artificial halos in which we rotate the direction of the principal axes following a logarithmic spiral in radius. We found that twist biases the estimated ellipticity by 10% when the halo axes rotate by more than π radians within one virial radius of the halo. In N-body simulations, halos do not show such high degrees of twist within their virial radius. Typically the rotation of the major axis is $\lesssim \pi/6$ within one virial radius [92], and for such low twist angles, the bias generated by twist is negligible. Therefore, it is safe to conclude that the twisting of halos does not significantly affect the measurement of ellipticity with the 3-point correlator based on our simple mass model, as we might have guessed based on the good agreement between the estimated ellipticity and true ellipticity of our N-body halos. Overall, our analysis of N-body halos suggests that systematic errors due to our simplistic mass model will not significantly bias our measurement of halo anisotropy.

5.3.2 Shape noise

In most regimes of weak lensing, the shear signal due to weak gravitational lensing is orders of magnitude weaker than the noise introduced by the intrinsic distribution of galaxy shapes and orientations. To estimate the magnitude of the errors induced by shape noise, let us first define the shape noise per galaxy $\vec{\mathcal{N}} = \{\mathcal{N}_+, \mathcal{N}_\times\}$. Each component of $\vec{\mathcal{N}}$ is assumed to be a Gaussian random variable with covariance

$$\langle \mathcal{N}_i \mathcal{N}_j \rangle = \sigma_\varepsilon^2 \delta_{ij} \tag{5.22}$$

where the indices i and j correspond to the tangential and cross components of the noise, and $\sigma_\varepsilon = 0.25$ [119]. The number density of source galaxies is $n(\vec{x}) = \sum_i \delta(\vec{x} - \vec{x}_i)$, with

mean number density $\bar{n}$. Then the 2-point correlation of the shape noise is

$$\langle \mathcal{N}_i(\vec{x}_1)\mathcal{N}_j(\vec{x}_2)\rangle = \sigma_\varepsilon^2 \delta_{ij} \frac{\delta(\vec{x}_1 - \vec{x}_2)}{\bar{n}} \tag{5.23}$$

Within an area A, where the number of galaxies is approximately $N = \bar{n}A$, the signal expectation value derived in Eqn. (5.20) is

$$S = \langle \boldsymbol{\gamma} \cdot \mathbf{F} \cdot \boldsymbol{\gamma} \rangle = \frac{\pi^2 \varepsilon^2}{2A^2} \left\{ \int \left[g_+^2(r) + g_\times^2(r) \right] r \, dr \right\}^2 \tag{5.24}$$

In comparison, the noise variance is

$$\begin{aligned} \sigma_N^2 &= \langle (\mathcal{N} \cdot \mathbf{F} \cdot \mathcal{N})^2 \rangle - (\langle \mathcal{N} \cdot \mathbf{F} \cdot \mathcal{N} \rangle)^2 \\ &= \frac{\sigma_\varepsilon^4 \pi^2}{\bar{n}^2 A^4} \left\{ \int \left[g_+^2(r) + g_\times^2(r) \right] r \, dr \right\}^2 \end{aligned} \tag{5.25}$$

where the expectation value is computed by both summing over all possible triangles in the sky and also by taking the ensemble average of the Gaussian noise field. In the second equality, we have used Eqn. (5.23) and Wick's theorem. Therefore the expected signal to noise per lens galaxy for the constructed estimator is

$$\frac{S}{\sigma_N} = \frac{\pi \varepsilon^2 \bar{n}}{2\sigma_\varepsilon^2} \int \left[g_+^2(r) + g_\times^2(r) \right] r \, dr. \tag{5.26}$$

As we might expect, the signal to noise ratio (SNR) per lens scales quadratically in the shear. Therefore the signal should be easiest to detect for more massive galaxies that produce stronger shear, as long as the abundance of galaxies does not fall steeply with mass. To get a sense of the expected SNR, we can perform a rough estimate by approximating the halo profile as isothermal ($\Sigma_0 \propto r^{-1}$), which Figure 5.3 shows is not a terrible approximation over the radial range of interest. To be concrete, suppose that the monopole profile is $\kappa_0(r) = b/(2r)$. Plugging this into Eqn. (5.26), we find that $S/\sigma_N \approx [\pi b^2 \bar{n} \varepsilon^2/(8\sigma_\varepsilon^2)] \log(r_{\max}/r_{\min})$

per lens. Taking $\varepsilon = 0.2$, $\sigma_\varepsilon = 0.25$, $\bar{n} = 12\,\mathrm{arcmin}^{-2}$ as appropriate for DES, $b = 1$ arcsecond, and $r_{\max}/r_{\min} = 20$ gives $S/\sigma_N \approx 0.0025$, meaning that with 10^6 such lenses, we could detect the expected ellipticity at $\sim 2.5\sigma$. LSST will have more than twice the effective number density of sources [119], more than doubling the signal to noise of the 3-point estimator. At this point, it is perhaps worth comparing this estimate with the corresponding signal/noise ratio for a 2-point estimator. Repeating the argument of §5.2 for the analogous 2-point estimator, we find that per lens, $(S/\sigma_N)_{\mathrm{2pt}} = \sqrt{2(S/\sigma_N)_{\mathrm{3pt}}}$, for halos that are perfectly aligned with their galaxies on the sky. Since the SNR per lens is much less than 1, this illustrates that 2-point estimates of halo anisotropy will have much greater statistical sensitivity than 3-point estimators. As noted above, however, this superior statistical power may be irrelevant if systematic effects due to halo misalignments remain uncertain.

5.3.3 Other systematics

Above, we discussed potential systematic errors which could arise if our simple mass model failed to describe actual halos adequately, due to effects such as twisting or satellite contamination. Besides these systematics in the mass model, our proposed measurement will also be liable to possible observational systematics associated with the lensing measurement. One obvious observational source of systematic error is point spread function (PSF) anisotropy. The PSF determines how the actual shape of a galaxy on the sky is related to the observed shape of a galaxy, measured by a camera on a telescope possibly beneath the distorting effects of the Earth's atmosphere. Our ability to measure the PSF is frequently a limiting factor in our ability to measure the true shapes of weakly lensed galaxies, which degrades our ability to measure shear. In principle, this could be disastrous for the halo ellipticity measurement we have proposed. For example, if the PSF were uniformly anisotropic across the virial radius of a lens halo, leading to a spurious, uniform shear, this would exactly mimic the ellipticity signal we are seeking to detect. In practice, however, mitigating such effects in

galaxy-galaxy lensing measurements should be straightforward, as long as the shape of the PSF is not strongly correlated with the number of foreground lens galaxies. For example, we can assess the extent of such PSF anisotropies by stacking on random sky points instead of lens galaxies. Even if PSF anisotropies are present, the ellipticity signal should appear as an excess correlation with lens galaxies, above what is seen around random sky points. As discussed in §5.3, the same test would also help remove the effects of masses uncorrelated with the lens galaxies.

Another potential astrophysical contamination of the signal arises from intrinsic alignment between galaxies [120, 121, 122, 123, 124, 125, 126]. Galaxies that form and evolve in the same local environment may be systematically aligned with each other due to long range tidal effects [127], consequently replicating the correlation that is produced by gravitational lensing. This effect can manifest itself in two ways, (i) nearby source galaxies can be preferentially aligned with each other, and (ii) lens-source pairs can be physically associated with each other, if (for example) a fraction of source galaxies are satellites of the lensing, foreground galaxy. Both these problems can be mitigated using redshift information, for example by excluding galaxy pairs with similar redshifts. Observationally, the contamination of galaxy-galaxy lensing due to alignments from lens-source correlations produced by photometric redshift errors has been shown to be exceedingly small in SDSS [128]. Stacking on random points, as discussed above, would also help to quantify and remove the effect of alignments of pairs of source galaxies.

Magnification of lenses could also produce a systematic effect on the signal. Our estimator correlates the number density of foreground galaxies, n_g, to the shear at two positions in the sky, γ_1 and γ_2. The foreground galaxies (lenses) are lensed by matter distribution between the observer and the lens along the line of sight. This causes a modification of the clustering of lenses due to cosmic magification along the line of sight. The variation from the unlensed number density is, to lowest order, linear in the lensing convergence, $\kappa_<$ [115]. In addition the shear itself has a contribution from the matter density, integrated along the line of

sight to the redshift of the source. The combined effect therefore contributes to the 3-point correlator, $\langle n'_g \gamma'_1 \gamma'_2 \rangle$, terms like $\langle \kappa_< \, \gamma_{1<} \, \gamma_{2<} \rangle$. These third order shear correlations have been measured to be less than 10^{-7} [129, 130] for aperture scales of $\theta \sim 1'$ and source redshift $z_s \sim 1$, while [115] predict an upper bound to the effect of magnification of lenses on three point statistics of 10^{-8} for sources at $z_s \sim 0.4$. Therefore, it appears that this effect will not significantly contaminate the measurement of halo ellipticity.

Photometric redshifts can also lead to systematic errors for our estimator. Redshift errors produce errors in $\Sigma_{\rm crit}$, which become density errors when converting from shear γ to $\Delta\Sigma$. Because our ellipticity estimator is nonlinear, this can bias the inferred ellipticity. Assuming that photometric redshift errors of source galaxies do not correlate with projected separation to the lens galaxies, then a fractional systematic error in $\Sigma_{\rm crit}$ of size $\delta = \delta\Sigma_{\rm crit}/\Sigma_{\rm crit}$ produces a fractional error in the ellipticity of order δ. For modern surveys, systematic errors in photometric redshifts are expected to be at the level of $\lesssim 1\%$ [131, 132, 133], indicating that this source of bias will likely be subdominant compared to other systematics.

Another potential systematic is the effect of baryons, which can act to modify the halo axis ratios on small scales $\lesssim 0.25 r_{\rm vir}$ [134, 135]. Judging from Figure 5.3, our estimator is most sensitive to the ellipticity at somewhat larger radii, suggesting that baryonic effects will be limited. In principle, we can suppress any baryonic effects on our estimator by restricting the range of integration ($r_{\rm min}$ and $r_{\rm max}$ in Eqns. (5.17)-(5.19)) to exclude small-scale regions that may be contaminated [136]. Alternatively, given sufficient signal to noise, one could try to measure the ellipticity as a function of radius by subdividing the sample, for example by comparing triangles at large vs. small separation. Besides constraining any radial variation in ellipticity, 3-point lensing could also probe any twist, i.e. misalignments between the principal axes at small radii vs. large radii. We defer such possibilities to future work.

5.4 Discussion

We have shown that the lens-shear-shear three-point correlation function can be used to extract the ellipticity of dark matter halos, without the need to align the light profiles of galaxies that are being stacked. Using a simple model of the projected surface density profiles of dark matter halos, we constructed an estimator for halo ellipticity that sums over all triangular configurations of the 3-point function. We validated our estimator using simulated halos from the Bolshoi cosmological simulation, showing that the shear-derived estimator yields results consistent with the ellipticity measured directly from the particle data. We investigated potential sources of systematic error, and argued that they should be small, at the $\sim 5\%$ level, well below theoretical uncertainties. We also estimated the signal to noise ratios expected for imaging surveys, and found that deep imaging surveys should be able to detect halo ellipticities. The total signal to noise scales with the number of lens-source-source triplets as $N_t^{1/2} \propto n_l^{1/2} n_s$, meaning that deep imaging surveys with large effective number densities of sources will be most sensitive. Ongoing surveys like PanSTARRS, DES, and HSC may be able to detect halo ellipticities at the $\sim 2\sigma$ level, while future surveys like Euclid or LSST should have sufficient sensitivity for a significant ($> 3\sigma$) detection. The same surveys will, of course, be able to measure 2-point galaxy-galaxy lensing with far greater signal to noise than 3-point lensing. However, if 2-point estimators are limited by systematic uncertainties, as suggested by theoretical work on galaxy-halo misalignments [112], then 3-point lensing could prove to be a useful probe of halo anisotropy. Indeed, a comparison of the ellipticity determined by the 2-point estimator vs. the 3-point estimator could be used to determine the typical misalignments between galaxies and their halos. If a galaxy is misaligned with its halo by angle $\theta_{\rm mis}$, then the ellipticity determined from the 2-point estimator is lowered by a factor $\cos(2\theta_{\rm mis})$. Therefore, the average misalignment angle may be inferred as $\varepsilon_{\rm 2pt}/\varepsilon_{\rm 3pt} = \langle \cos(2\theta_{\rm mis}) \rangle$.

In this paper, we have investigated one particular application of the measurement of

3-point correlation functions. As theoretical work has shown [115], high-order correlation functions contain significant amounts of information above and beyond that encoded in better studied 2-point functions. The advent of deep, wide-area imaging surveys is now making the measurement of these high-order correlations practical across a range of spatial scales, suggesting that this will be a fruitful area of research for years to come.

Chapter 6

The curious incident of the blue galaxy that crossed splashback at night time

The fraction of quenched or red galaxies in clustered environments is much higher than its average value in the field. Two competing theories of galaxy evolution both claim to reproduce the observed spatial distribution of red galaxies, the first through invoking quenching by intracluster processes and the second by age matching galaxies to older subhalos. In this paper we use the kinematic properties of galaxies in clusters to probe new signatures of the underlying mechanism that sets this behavior. We study the line of sight velocity distribution of subhalos in Nbody simulations and compare the dynamics of populations separated based on the duration of their lifetime in the halo and their overall age since formation. We find that the galaxy populations separated by their age in the host halo most closely resemble the kinematical behavior of red and blue galaxies around RedMaPPer clusters in SDSS. Red galaxies are consistent with having fallen in early while blue galaxies have been accreted later.

6.1 Introduction

In hierarchical structure formation galaxies form by condensation of baryons inside dark matter halos. These halos are often accreted onto larger structures where they reside as subhalos and orbit in the potential of the host. Galaxy overdensities in the sky are therefore associated with massive clusters or groups that have accreted substructure that host these galaxies. One striking characteristics of these massive structures is that the galaxies that compose them appear to be mostly early type, elliptical galaxies that are red and have little

or no active star formation. The red fraction in these galaxy clusters is much higher than the average in the field and increases towards decreasing cluster centric radius. It is a long standing puzzle as to how large overdensities in the dark matter field lead to a supression of star formation which is a baryonic processs. Fig 6.1 shows the projected number density of galaxies around RedMaPPer clusters in the SDSS galaxy catalog DR7. The redfraction rises steeply as a function of radius and is much higher than the density of blue galaxies.

There are primarily two broad classes of theories that attempt to explain the high red fraction around massive dark matter halos. The first class of theories claim that the quenching of star formation occurs due to astriphysical processes in the potential of the cluster. A cluster halo is a fairly inhospitable environment for a galaxy, as it enters the strong gravtiational field of the host halo the accretion shock at infall [137, 138] and processes like strangulation[139], harassment, ram-pressure stripping [140, 21], tidal disruption all tend t,o strip gas from galaxies, quenching star formation. Therefore longer a galaxy resides inside a cluster, lesser is the amount of cold gas available to condense into stars. The galaxy eventually ceases to form stars and begins to appear red. Additionally the probability of galaxy mergers within a clustered environment is also higher, which also leads to heating of the gas in galaxies creating aother possible avenue for blue galaxies to turn red. Suppression of star formation by intra cluster process reproduces the observed statistics of quenched galaxies. [141]. Comparing the quiescent fraction from the COSMOS survey around groups selected in the SDSS DR7 catalog with N-body simulation that follow the star formation histories of satellites at z=0 [141] find that the observed queiscent fraction can be reproduced if satellites remain actively star forming 2-4 Gyrs after infall and followed by an exponential decay in star formation.

Apart from quenching of star formation inside galaxy clusters due to astrophysical processes Hearin et al. [142] showed that the statistics of red and blue galaxies around dark matter halos can also be constructed simply from age matching models. The underlying idea here is that if we assume that all galaxies internally shut off star formation at a certain time

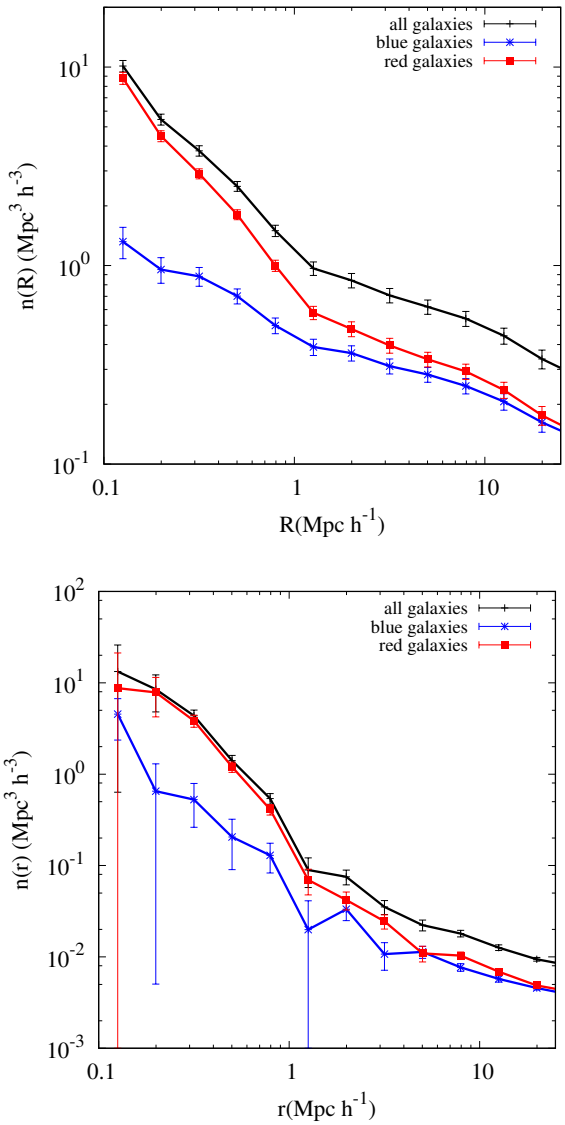

Figure 6.1: The top panel shows the projected number density of spectroscopic galaxies around RedMaPPer clusters between $0.1 < z < 0.2$.(Bottom) The deprojected, 3d number density of galaxies.

in their lifetime and turn red, older galaxies will appear redder. As galaxies evolve with their host halo older galaxies therefore tend to live in older halos. From the statistics of density perturbations in the early universe it is known that older subhalos tend to live in clustered regions. Density perturbations that collapse to form subhalos in clusters are initially lying on a background longer wavelength pertrubation that will ulitimately form the cluster and therefore collapse earlier. In Hearin et al. the observed distribution of red and blue galaxies was reproduced using age-matched mock subhalo catalogs. This scenario therefore does not require any intracluster processes to quench star formation at all it naturally predicts an abundance of red galaxies in clustered environments.

Given the existence of evidence for conflicting models there exits enough motivation exists to look for new signatures that will help distinguish between the two scenarios.The recent detection of the splashback radius [69, 143] also adds a new dimension to this picture. The splashback radius is associated with a sharp drop off in density in the outskirts of a halo. Theoretically this drop off occurs at the first apocentric passage of a particles or subhalos after it begins to orbit inside the halo [4, 26, 144]. This radius forms the boundary between the "virialized" or multi streaming region and the infall region of the halo. In the spherical approximation, there are no objects that have completed an orbit in the halo potential. Baxter et al. [143] use the cross correlation between the SDSS galaxy catalog and RedMaPPer cluster and measure the red fraction around galaxy clusters. they find that the red fraction changes sharply at the splashback radius of the halo approaching the background value almost immediately beyind splashback. This seems to indicate that the quenching of galaxies closely follows the cluster boundary. While this may hint at the fact that cluster physics is responsible for galaxy quenching, it is not clearly ruled out that age matching can not produce similar sharp transitions in red fraction.

Chamberlain et al. [145] propose an alternative method to probe the ages of satellites in their host. Based on N-body simulations they show that spatial correlations of subhalos beyond their tidal radius persist for subhalos that have recently been accreted on to the host.

These correlations only disappear after a subhalo has been orbiting inside a halo for several dynamical times and can therefore act as a clock indicating the time after infall into the halo. Fang et al. [146] measured this signal in edMagic galaxies around RedMapper clusters. They find that signicant fraction of the reddest galaxies have fallen in recently making an argument in favor of galaxies being quenched even prior to their infall into the host.

Studies so far however have concentrated mostly on the spatial distribution quenched galaxies to make conjectures about the physics that sets their behaviour. In this paper we study the merits of using kinematics as a probe to distinguish between the two scenarios. In particular we use the line of sight distribution of galaxies to distinguish between the different evolution models. The simple argument is that if the environment of clusters, i.e. intracluster physics is responsible for galaxy quenching the effect will be much stronger for objetcs which are on plunging orbits, that reach far inside the halo, as compared to objects which are on orbits with higher angular momentum. Objects that is on such tangential or grazing orbits may therefore be less effected by tidal stripping, ram pressure-stripping, harrassment which are all stronger near the cluster center. Therefore we may expect that galaxies that are on such radial orbits switch of star formation and create the population of red galaxies, where as galaxies that avoid such orbits still appear blue and star forming. If this were the distribution of velocities of blue and red galaxies would be different.

In observations we can measure the line of sight velocity distribution. In an annulus in projected distance from the cluster center objects that are on tangential or high angular momentum orbit have a higher velocity dispersion with a deficit of galaxies with 0 line of sight velocities. The distribution of velocities for such galaxies should appear doubly peaked or bimodal with peaks corresponding to objects redshifted and blue shifted with respect to the observer. Where as radial orbits should for a distribution peaked at $v_{los} = 0\ km/s$.

As galaxies reside inside subhalos we begin by analyzing N-body simulations of cold dark matter to study the kinematics of subhalos inside clusters for different populations of subhalos in section I. In section II & III we use the spectroscopic galaxy catalog of SDSS DR7

to measure the line of sight velocity distribution of galaxies around RedMaPPer clusters.

6.2 Simulation results

To understand the dynamics of galaxies we study subhalos in N-Body simulations. We compare them to mock galaxy catalogs created from the MDPL2 simulations. These simulations have 3840^3 particles in a $1Gpch^{-1}$ with a mass resolution of $1.51 \times 10^9 M_{\odot} h^{-1}$. The associated halo catalogs were made using the phase space halo finding algorithm Rockstar. We look at orbits of subhalos inside host halos with masses greater than $10^14 M_{\odot} h^{-1}$ at z=0. This mass was chosen to match the mass from the RedMaPPer cluster with richness, $20 < \Lambda < 100$ which was callibrated using lensing. We only consider subhalos with peak velocities $v_{peak} > 200\ km/s$

Mainly we make two separate kinds of subhalo catalogs. One where we associate a subhalo with blue or red color based on a the age or formation time of the subhalo. This is in keeping with the idea that simple age matching catalogs can reproduce the behavior of red and blue galaxies in observations. And the other kind where subhalos are characterized as blue or red based on how long they have been inside the cluster cluster or how small their impact parameter to the host halo center is. For age matching we choose parameters like the concentration of the halo at accretion, c_{ac}. This is evaluated from the Rockstar merger history of subhalos. For age inside a halo we use a_{acc}, the time at which a subhalo is accreted into the host halo, current concentration today, c_{tod}.

Our ultimate goal is to find an observable signature that will help distinguish between the two models. Therefore we must keep in mind that an observer only has access to the projected distribution of galaxies and velocities in the sky. To isolate the effect of the cluster we would ideally like to remove the contamination of our measurements by randomly projected structure along the line of sight to the cluster. Assuming that the halo is isotropic one powerful method to deproject and get the complete distribution function of objects

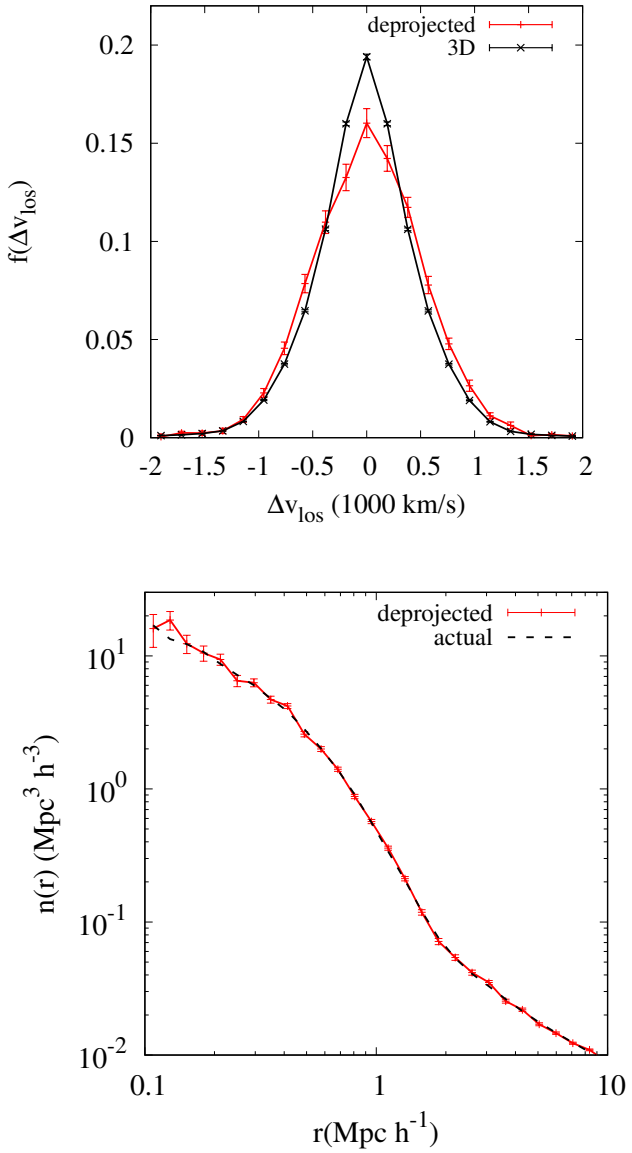

Figure 6.2: Comparison between deprojected histogram and actual 3D distribution of subhalos between 0.6 and 0.9 $Mpc\,h^{-1}$ around cluster mass halos of $1-2\times10^{1}4M_{\odot}h^{-1}$. The top panel shows the LOS velocity histograms and the bottom panel shows the number density profiles.

associated with the true three dimensional radius at the projected radius R is to use the Abel integral transform. Given a the projected distribution function of subhalos, $\Sigma(R, v_{los})$ we can obtain the 3D, deprojected distribution function as,

$$\rho(r, v_{los}) = -\frac{1}{\pi}\int_r^\infty \frac{d\Sigma(R, v_{los})}{dR}\frac{1}{\sqrt{R^2 - r^2}}dR \tag{6.1}$$

where r is the 3 dimensional cluster centric radius. The 2D projected function is obtained as a sum of delta functions at the position of each galaxy.

$$\Sigma(R, v_{los}) = \sum_i \frac{\delta(R - R_i)\delta(v_i - v_{los})}{2\pi R_i}; \tag{6.2}$$

Therefore the total number of objects in a 3D radial bin extending from of $r = a$ to $r = b$ with velocity v_{los} is given by $4\pi\int_a^b \rho(r, v_{los})r^2 dr$. Substituting 6.2 into this expression,

$$\Delta N(v_{los}) = \sum_i \frac{-2}{\pi R_i}\int_a^b dr \int_r^\infty \frac{d\delta(R - R_i)}{dR}\frac{r^2}{\sqrt{R^2 - r^2}}dR \tag{6.3}$$

Doing the integration over r first followed by integration by parts we obtain,

$$\Delta N(v_{los}) = \begin{cases} g(R_i/a) - g(R_i/b) & R_i/a > 1, R_i/b > 1 \\ g(R_i/a) + 1 & R_i/a > 1, R_i/b < 1 \\ 0 & R_i/a < 1 \end{cases}$$

where

$$g(x) = \tan^{-1}\frac{1}{\sqrt{x^2 - 1}} - \frac{1}{\sqrt{x^2 - 1}} \tag{6.4}$$

Using this expression we can evaluate the weighted sum to obtain the actual distribution of LOS velocities in the 3D radial bin.

It must be noted that in general the Abel transform works for scalar quantities. The line of sight velocity, however is a component of a vector. Our deprojection scheme is only valid if we consider that the velocity dispersion around the halo is isotropic While this is

not in general true for halos as they are usually triaxial, stacking over a group of halos, all randomly oriented, can somewhat alleviate this problem.

Fig 6.2 illustrates the validity of the method of deprojection. In the top panel of Fig 6.2, the red curve shows the deprojected velocity histogram of subhalos within hosts of mass $10^{14} - 2 \times 10^{14} M_{\odot} h^{-1}$at $0.6 < R < 0.9$ Mpch^{-1} obtained from the 2D, projected distribution of subhalos using eqn 5.

The deprojected LOS velocity histogram at a given R corresponds to subhalos at the 3D radius $r = R$. For these subhaloes the line of sight lies in a plane tangential to the radius vector connecting them to the centre of the halo. Therefore the LOS velocity histogram is the distribution of the component of the tangential velocities along directions in the tangent plane to the radius vector.

To check how well our scheme works we evaluate the quantity obtained by deprojection directly using the 3D position of the subhalos. We extract all subhalos that are in the 3D radial bin $0.6 < r < 0.9$ Mpc h^{-1}. Suppose a subhalo has a tangential velocity magnitude v_t. Along any given line of sight in the tangent plane to the radius vector it can only contribute to LOS velocity bins, v^i_{los}, when $v^i_{los} < v_t$. Let us say we have a velocity bin extending from v^i_{min} to v^i_{max} . The line of sight on the plane that will measure an LOS velocity of v^i_{min} makes an angle of $\theta_{min} = cos^{-1}(v^i_{min}/v_t)$ with the direction of $\vec{v_t}$ and the line of sight along which the observer measures v^i_{max} makes an angle of $\theta_{max} = \cos^{-1}(v^i_{max}/v_t)$. Therefore all line of sights between θ_{max} and θ_{min} will contribute to the i^{th} velocity bin. Integrating over all directions in the plane the probability of finding a line of sight between the θ interval is given by $\Delta\theta/\pi$, where $\Delta\theta = \theta_{min} - \theta_{max}$. Therefore every subhalo contributes a weight of $\Delta\theta/\pi$ to the velocity bins where $v^i_{min} < v_t$ and $v^i_{max} < v_t$. Following the same arguments the weights for bins with $v^i_{min} < v_t$ and $v^i_{max} > v_t$ can be worked out simply. We evaluate this weighted sum over all subhalos in the 3D radial bin to obtain the black curve in the top panel of Fig 6.2. We find that the deprojected curves mostly agrees with the actual 3D curve with some differences due to anisotropy. The bottom panel of Fig 6.2 shows comparison bewteen the

deprojected number density profile obtained from the 2D profile and the actual 3D number density measured from the simulation. Evidently for scalar quantities the reconstruction is almost an exact fit. Given we now have a fairly good method to extract information about the deprojected distributions we now proceed to measure the line of sight velocity distribution for our different subhalo populations.

In top row of Fig 6.3 we show the stacked line of sight velocity histograms for subhalos around clusters of mass $10^{14}M_{\odot}h^{-1} - 2 \times 10^{14}M_{\odot}h^{-1}$. The subhalos have been divided into blue and red based on the time at which they were accreted on to the host halo. The crossing time for a subhalo falling in with $\sim 1000km/s$ is about 1.2 Gyrs for these halos. The halos that have been accreted late or after $a = 0.85$ are called blue while those accreted early, or before $a = 0.85$ are called red. Since the time gone by since $a = 0.85$ is abot 2.2 Gyrs, most of these halos have made a pericentric passage. It must be noted that halos that are within the splashback radius of the halo, i.e. 1.2 Mpc h^{-1} have been assigned red and blue colors based on their accretion time, however those that are ouotside this radius have been assigned a random color based on a background red fraction of 0.5. Splitting on accretion time shows that the two sets of subhalos show very different kinematics. Halos that have been accreted late show a LOS velocity distribution that is much broader than halos accreted early. Their velocity distribution also shows a double peaked feature that is consistent with halos that are on tangential orbits and therefore in the line of sight projection in a radial annulus they show a blue shifted and a redshifted feature. This shows that halos that have spent more time inside the cluster are on radial orbits. As the halo grows substructure accreted late tend to have larger impact parameters and therefore angular momentum.

In the second row of Fig 6.3 we divide the subhalos based on the concentration measured from the rockstar merger tree at the time when they were accreted into the halo. For halos that are entering a host for the first time, the concentration of their density profile is related to their age or formation time. Halos that have high concentrations, are slow accreting and hence for a given mass today halos with high concentration have assembled their mass

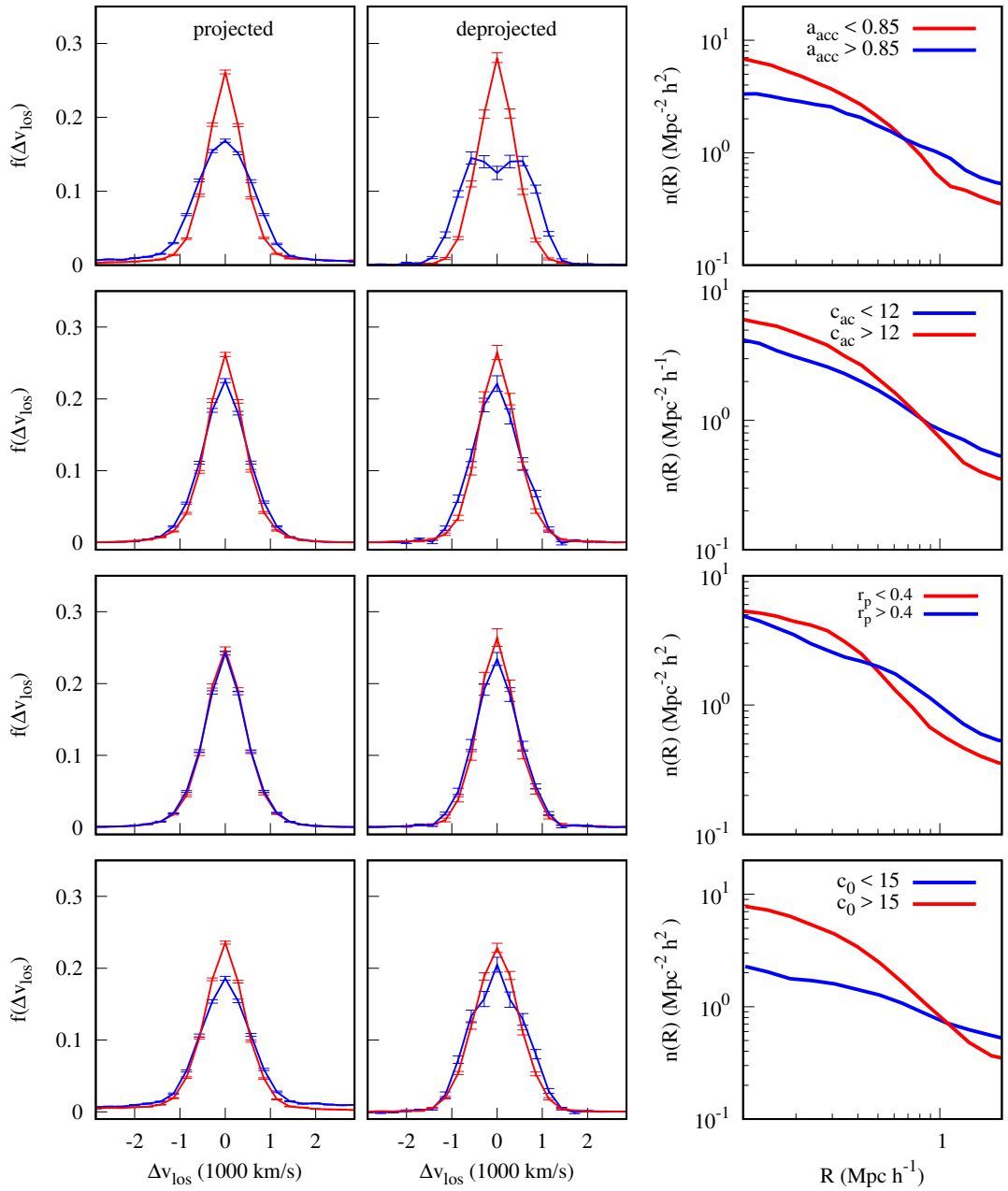

Figure 6.3: The left two panels show the LOS velocity histograms at $0.6 Mpch^{-1} < R < 0.9$ Mpch^{-1} of subhalos with $Vpeak > 200km/s$ around host halos with mass $10^{14} M_{\odot} h^{-1} < M < 2 \times 10^{14} M_{\odot} h^{-1}$. The first column shows the projected and the second column shows the deprojected histograms. The last column shows the projected number density of the subhalos around their host halos. The different rows each correspond to a different criteria of splitting the subhalos into red and blue. In the top panel suhalos have been split into red and blue based on the time at which they were accreted into the host halo. In the second row they have been split based on their concentration at accretion, in third based on their pericenters and in the last column they have been split based on their present day concentration.

earlier and are older, while halos with low concentration are fast accreting and younger. The second row of Fig 6.3 shows that the kinematics of young and old halos once they have been accreted on to the cluster are not significantly different from each other even though the differences in their average radial number profile is consistent with observed blue and red galaxies.

The two examples demonstrate that the kinematics of subhalos can be used to distinguish between two separate conjectures about the evolution of galaxies inside clusters. Assigning colors to subhalos based on their accretion time corresponds to the idea that the cluster environment alters the behavior of substructure that falls into it where as assignment on colors based on their concent density ration at infall is similar to the idea of age-matching reproducing the difference in the number density profile of blue and red galaxies around halos. Apart from c_{ac} and $a_a c$ we divide subhalos into different populations based on their current concentration, c_0 (Fig 6.3 third row)and distance of closest approach or pericenter, r_p (Fig 6.3 last row). The concentration was obtaied from the rockstar catalog. For the pericenters we used the merger history of the subhalos to measure its orbit inside the host. Subhalos that are on orbit with large pericenters also show evidence of kinematics different from the those with smaller pericenters. However it must be noted that the publicly available MDPL2 snapshots do not have a very high time resolution.

It is known that for a spherical system in equilibrium the density profile and the velocity dispersion profile is determined completely by the Jeans equation if the anisotropy parameter β is known. Therefore it is worth asking if the velocity dispersion profile in the line of sight direction is giving us new information. It is important to note that if physical processes within the cluster strip gas off of orbiting galaxies that lead to a cessation of star formation making blue galaxies red, in this case the number of galaxies is not conserved and therefore it is not obvious if the density profile and the velocity dispersion is related in a straight forward way. This us evident when we compare the last two panels of Fig 6.3. In both cases the prjected number density profile of blue and red galaxies different slopes between 0.6 and

0.9 Mpc h^{-1} however the line of sight velocity distributions of the two populations is nearly identical when subhalos are subdivided based on their present day concentration, c_0, where as that is not the case when they are subdivided based on their time of acceretion on to the host.

6.3 Data

To use the kinematic information of galaxies in clusters to distinguish between different scenarios we require very precise measurements of the line of sight velocity. For this purpose we use the spectroscopic galaxy sample from the eighth data release of Sloan Digital Sky Survey(SDSS). We use the SDSS derived RedMaPPer cluster catalog [70, 71]. Again as we are primarily interested in relative velocities of galaxies inside clusters we only use the RedMaPPer clusters that have spectroscopic redshifts. Our sample has a total of 1498 clusters with spectroscopic redshifts $0.1 < z < 0.2$ and richness $20 < \Lambda < 100$. Additionally we choose a lower threshold in the miscentering probability of the central galaxies, $P_cen > 0.8$, this leaves us with 860 clusters. The cross-correlation of galaxies and clusters was measured by stacking the number of spectroscopic galaxies as a function of radius around cluster centers identified using the RedMapper algorithm [70]. The galaxy sample consists of 1200160 galaxies. We select red and blue galaxies based on their galaxy colors $(g - r)$. The magnitudes of the galaxies have been k-corrected using the technique defined in [147, 148]. Apart from the division of galaxies into quenched and active based on the galaxy colors we also look at a catalog of galaxy morphologies in SDSS. We use the to Meert et al. [149] catalog to characterize a galaxy as a disky or elliptical.

6.4 Observation results

Our main goal is to measure the distribution of line of sight velocities around the sample of clusters selected using RedMaPPer clusters. The pairwise velocity of galaxy and cluster was calculated using their spectroscopic redshifts. For the cluster the redshift is measured from the spectra of its central galaxy. The pairwise line of sight velocity is given by,

$$\Delta v_{los} = \frac{z_g - z_c}{1 + z_c} \tag{6.5}$$

A galaxy is classified as red if $(g - r) > 0.8 - 0.03(M_r + 20)$ where M_r is the absolute magnitude in the r band, the rest of the galaxies are classified as blue.

Fig 6.1 shows the projected number density of different population of galaxies around our cluster sample. The bottom panel shows the deprojected, 3D number density profile of galaxies. The deprojection was done in the method described above for the simulation. the splashback radius for this sample of clusters measured using spectroscopic galaxies only is at 0.67 Mpch^{-1}. The splashback radius acts as the boundary between the virialized and infall regions of the halo. Theoretically this separates a population into objects that have completed atleast one entire orbit in the halo potential vs. those that have never had a pericentric passage and are still in infall. This distinction is important in our context given it serves as an approximate boundary to the cluster's influence.

Fig 6.4 shows the normalized LOS velocity histograms of blue and red galaxies in three different radial bins from the halo center. The first bin extends from $0.4 < R < 0.8$ where R is the projected distance from the halo center. This bin has subhalos that are immediately inside the splashback radius. The splashback feature has a finite width which is why it extends to radii slightly beyond it. The second bin between $0.8 < R < 1.2$ must correspond to subhalos mostly in the infall region. We also show the velocity histogram far outside the halo out to 2Mpc h^{-1}. The red and blue curves correspond to red and blue galaxies as defined in the previously. The top panel shows the projected LOS histogram. To remove

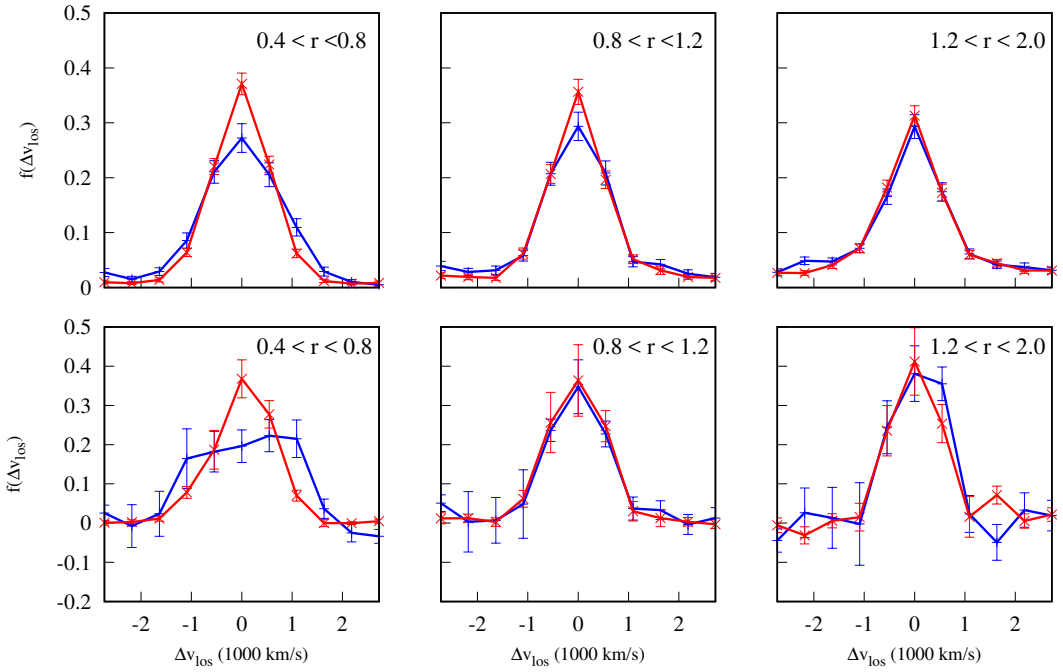

Figure 6.4: Velocity histograms around redMaPPer clusters of blue and red galaxies. Top panel shows the projected velocity histograms. The bottom panel shows the deprojected profiles.

the contribution from galaxies that are projected in the line of sight along the radial shell extending from 0.3 to 0.6 we deproject our the histograms as was done in the case of the simulations.

We note that the velocity ditribution for the two galaxy populations are remarkably similar in the outskirts of the galaxy clusters. At smallest radial bin inside of splashback there is a distinct difference between the blue and red population. The blue galaxies are clearly exhibiting a separate dynamical behavior as compared to the red ones. The dispersion in their velocity distribution is larger than that in the red population consistent with being on orbits with large angular momentum.

To quantify the conjecture that the two populations have been drawn from different distribution functions we use a procedure similar to the Kolmogorov-Smirnov test. This is a model independent or non-parametric test the null hypothesis that two populations have been drawn from the same underlining distribution functions. We construct a test similar to

the KS test for our binned sample. We evaluate the cumulative distribution function(CDF) for the two samples and measure the maximum difference between the CDF of the blue and red galaxies. We also construct catalogs of galaxies with randomly assigned blue and red colors each with a different red fraction corresponding to the radial bins in the actual data. We reevaluate the velocity histograms in the different radial bins using the random catalog with the appropriate red fraction and reconstruct the CDFs to get the maximum difference between the red and blue distributions. We generate monte carlo realizations of the catalog or randoms to measure the ditribution of the value of the maximum difference. This is our test sample where the red and blue galaxies are being drawn from the same population. We find how often the difference computed in the test sample is as large as the real data. We find that for the innermost radial bin between $0.4 < R < 0.8$ the deprojected distribution of red and blue galaxies are different from each other at greater than 99% confidence. Our method of estimating the significance level of the data from relative measurements of the maximum difference is independent of the number of line of sight velocity bins used.

6.5 Discussion

The kinematic behavior of blue and red galaxies are significantly different from each other in the inner regions of a cluster, i.e within the splashback radius. In the infall region of a cluster the red and blue galaxies fall in with a velocity distribution which is indistinguishable. Infalling galaxies have a distribution which is consistent with radial motion. However inside the boundary the blue galaxies appear to be on orbits with higher angular momentum. For the blue galaxies in the bin $0.3 < R < 0.7$ we can arguably also measure the bimodality in the histogram which implies galaxies on tangential orbits.

The difference in the red and blue is most closely imitated in simulations when subhalos are classified into different colors based on their accretion time a_c. HIn the simulations we find no difference in kinematic behavior of two population of subhalos that have different

concentrations at accretion that is related to their formation time. This seems to imply that longer a subhalos that fall into the cluster early are mostly on radial orbits. To draw an analogy with observations we can infer that the population of galaxies that are on radial orbits have fallen into the halo earlier than ones that are on tangential orbits. Implying that red galaxies were accreted earlier than blue galaxies. The red galaxies have presumably existed in the cluster for multiple dynamical timescales. These results therefore seem to provide evidence in favor of models of galaxy evolution inside clusters that claim satellite quenching occurs due to intra cluster processes. Although age matching models of Hearin et al. reproduce the observed spatial distribution of blue and red galaxies based on the simulations it appears that the velocity ditribution cannot be reproduced by simply age-matching of old halos to red and young ones to blue. This result also seems to be in apparent tension with [146] who measure the infall time of satellites SDSS cluster from the correlations between satellites in that persisting on angular scales beyond the tidal radius of the satellites. They find a significant amount of correlation even for the reddest galaxies implying they weren't quenched inside the cluster. It will be interesting to extend the treatment in [146] to include blue galaxies and compare their relative ages to the red population.

Chapter 7

Conclusions and Future work

7.1 Self interacting dark matter (SIDM)

Collisionless or cold dark matter has been highly successful in explaining the large scale structure of the universe. However, non-gravitational interactions of dark matter particles are often invoked to explain discrepancies between N-body simulations of CDM and observations on non-linear scales within dark matter halos. Scattering of dark matter by itself is one such form of interaction.

i) Spatial offsets in mass and light

If we allow for self-interactions in hierarchical structure formation, particles in subhalos that orbit within their host halos experience a force from interactions with the host particles. The stars within the galaxies that reside in these subhalos, on the other hand, are truly collisionless. This gives rise to a spatial separation in the centroids of the light and mass in the direction of the relative motion of the subhalo and its host. This effect was measured by [**?** 150] using HST data to obtain constraints on cross-section of self-interaction. These offsets, however, are not produced by isotropic scattering of dark matter. They require interactions where the probability for scattering is peaked in the forward direction and there is low probability for large-angle scattering.

ii) Shrinking of splashback radius

Apart from creating spatial offsets, another interesting effect of anisotropic scattering is the shrinking of the so-called, splashback radius for dark matter halos. Recently [69] detected the splashback radius in clusters with SDSS data. Intriguingly, they find that the splash-

back radius measured in observations is smaller than what was predicted from simulations of ΛCDM by nearly 20%. Self-interaction causes dark matter particles to lose energy and splashback at a smaller radius than in the absence of dissipative forces, providing a likely explanation for this discrepancy.

iii) Simulations

Simulations of SIDM have mostly concentrated on isotropic scattering. Given the multiple evidence for new physics, I am interested in simulating cosmologies with self-interacting dark matter with anisotropic scattering. The cumulative effect of a large number of interactions, with low momentum transfer, leads to a net decceleration which depends on the density at the location of the particle and its net relative velocity with the surrounding. Estimation of local densities are most easily modelled in grid based codes or codes with smooth particle hydrodynamics. I am currently modifying Gadget-2, an SPH code to study signatures of anisotropic self-interactions in halos. Having high resolution N-body simualations of SIDM will help us better interpret these intriguing departures from the cold dark matter paradigm. As preliminary tests Fig.2 shows the shrinking of the splashback radius with increasing cross-section of interaction, σ/m.

7.2 Mass accretion history of dark matter halos

It is well known that the assembly history of halos is closely related to its density profile. For example halos that have low concentrations, have higher accretion rates and assemble their mass at late times, whereas it is the exact opposite for halos with high concentration. The mass accretion history of halos is also fundamental to understand some of the most robust predictions of ΛCDM like assembly bias- the fact that clustering of halos depends their mass accretion histories(MAH) and formation times. Further, the recently observed splashback radius is also a strong function of the accretion rate of a halo and the redshift at which it forms. Constraining the accretion history can therefore make the splashback radius

a potential probe for the background cosmic evolution.

Recently we have reconstructed the MAH of halos using their cross-correlations with the present day mass profiles. Fig.1 shows such an example for $10^{14} M_{\odot} h^{-1}$ halos from the Multidark siulations. This illustrates that the present day density profiles of halos contains information about its accretion history. The accretion history of a halo can be determined from the shape of the initial density perturbation and its linear evolution. Therefore, if we can somehow reconstruct the profile of the initial density perturbation from the present day mass profile, we can predict its mass evolution.

The final, collapsed mass profile of a halo can be fairly well estimated from its initial density profile [8]. The simple physics setting the shape of the mass profile is determined by the adiabatic contraction of dark matter shells, where the adiabatic invariants, are specified by the linear density profile of the initial peak. As one of my proposed projects during my postdoctoral studies, I will be interested to reverse this method, i.e. investigate how to reconstruct the initial density profile, and therefore the MAH of a halo using only its final mass profile with simple arguments about the distribution of the adiabatic invariants with time and the mass deposition of shells with a distribution of pericenters.

Given the vast volume of observational data available today from large scale galaxy surveys like DES and LSST, it is the perfect time to study and test our understanding of the structure of dark matter halos. HST observations capable of weak lensing measurements will also be greatly useful to study individual systems, Hubble frontier fields and CLASH are two such notable examples. Another powerful way to probe the inner structure of clusters is through X-ray studies, therefore such methods will add value to projects like XMM and Chandra.

During my graduate studies I have mostly concentrated on dynamics of halo formation and its implications for cosmology. This has given me the opportunity to familiarize myself with a variety of tools to approach a problem. I have enjoyed understanding complicated, non-linear processes by simple analytical models that give us valuable physical insight. Fur-

ther, I have also learnt to write and manipulate different types of structure formation codes like, Gadget, Ramses and ECOSMOG- a cosmological code for modified gravity. I have thoroughly enjoyed being a part of these exciting times for cosmology and look forward to be able to contribute to the field in years to come.

References

[1] V. Springel, J. Wang, M. Vogelsberger, A. Ludlow, A. Jenkins, A. Helmi et al., *The Aquarius Project: the subhaloes of galactic haloes*, *MNRAS* **391** (Dec., 2008) 1685–1711, [0809.0898].

[2] J. A. Fillmore and P. Goldreich, *Self-similar gravitational collapse in an expanding universe*, **281** (June, 1984) 1–8.

[3] Y. Lithwick and N. Dalal, *Self-similar Solutions of Triaxial Dark Matter Halos*, **734** (June, 2011) 100, [1010.3723].

[4] S. Adhikari, N. Dalal and R. T. Chamberlain, *Splashback in accreting dark matter halos*, *JCAP* **11** (Nov., 2014) 19, [1409.4482].

[5] B. Diemer and A. V. Kravtsov, *Dependence of the outer density profiles of halos on their mass accretion rate*, *arXiv preprint arXiv:1401.1216* (2014) .

[6] M. Vogelsberger, R. Mohayaee and S. D. M. White, *Nonspherical similarity solutions for dark halo formation*, *Mon. Not. Roy. Astron. Soc.* **414** (2011) 3044, [1007.4195].

[7] A. J. Cuesta, F. Prada, A. Klypin and M. Moles, *The virialized mass of dark matter haloes*, *Mon. Not. Roy. Astron. Soc.* **389** (2008) 385, [0710.5520].

[8] N. Dalal, Y. Lithwick and M. Kuhlen, *The Origin of Dark Matter Halo Profiles*, *ArXiv e-prints* (Oct., 2010) , [1010.2539].

[9] A. Dekel, I. Arad, J. Devor and Y. Birnboim, *Dark halo cusp: asymptotic convergence*, *The Astrophysical Journal* **588** (2003) 680.

[10] E. Salvador-Solé, J. Viñas, A. Manrique and S. Serra, *Theoretical dark matter halo density profile*, *Monthly Notices of the Royal Astronomical Society* **423** (2012) 2190–2202.

[11] A. A. El-Zant, Y. Hoffman, J. Primack, F. Combes and I. Shlosman, *Flat-cored dark matter in cuspy clusters of galaxies*, *The Astrophysical Journal Letters* **607** (2004) L75.

[12] A. Manrique, A. Raig, E. Salvador-Solé, T. Sanchis and J. M. Solanes, *On the origin of the inner structure of halos*, *The Astrophysical Journal* **593** (2003) 26.

[13] D. Syer and S. D. White, *Dark halo mergers and the formation of a universal profile*, *Monthly Notices of the Royal Astronomical Society* **293** (1998) 337–342.

[14] A. Huss, B. Jain and M. Steinmetz, *How universal are the density profiles of dark halos?*, *The Astrophysical Journal* **517** (1999) 64.

[15] J. Wang and S. D. M. White, *Are mergers responsible for universal halo properties?*, *MNRAS* **396** (June, 2009) 709–717, [arXiv:0809.1322].

[16] B. S. Ryden, *Self-similar collapse of axisymmetric systems*, *The Astrophysical Journal* **418** (1993) 4.

[17] B. Allgood, R. A. Flores, J. R. Primack, A. V. Kravtsov, R. H. Wechsler, A. Faltenbacher et al., *The shape of dark matter halos: dependence on mass, redshift, radius, and formation*, *Mon. Not. Roy. Astron. Soc.* **367** (2006) 1781–1796, [astro-ph/0508497].

[18] J. C. Munoz-Cuartas, A. V. Maccio, S. Gottlober and A. A. Dutton, *The Redshift Evolution of LCDM Halo Parameters: Concentration, Spin, and Shape*, *Mon. Not. Roy. Astron. Soc.* **411** (2011) 584, [1007.0438].

[19] S. Adhikari, C. Y. R. Chue and N. Dalal, *Three-point galaxy-galaxy lensing as a probe of dark matter halo shapes*, *JCAP* **1501** (2015) 009, [1407.1128].

[20] S. Adhikari, N. Dalal and J. Clampitt, *Observing dynamical friction in galaxy clusters*, *JCAP* **1607** (2016) 022, [1605.06688].

[21] J. E. Gunn and J. R. I. Gott, *On the Infall of Matter Into Clusters of Galaxies and Some Effects on Their Evolution*, **176** (Aug., 1972) 1–+.

[22] J. Diemand, M. Kuhlen and P. Madau, *Formation and Evolution of Galaxy Dark Matter Halos and Their Substructure*, **667** (Oct., 2007) 859–877, [astro-ph/0703337].

[23] J. Diemand, M. Kuhlen, P. Madau, M. Zemp, B. Moore, D. Potter et al., *Clumps and streams in the local dark matter distribution*, **454** (Aug., 2008) 735–738, [0805.1244].

[24] J. Stadel, D. Potter, B. Moore, J. Diemand, P. Madau, M. Zemp et al., *Quantifying the heart of darkness with GHALO - a multibillion particle simulation of a galactic halo*, *MNRAS* **398** (Sept., 2009) L21–L25, [0808.2981].

[25] J. F. Navarro, A. Ludlow, V. Springel, J. Wang, M. Vogelsberger, S. D. M. White et al., *The diversity and similarity of simulated cold dark matter haloes*, *MNRAS* **402** (Feb., 2010) 21–34, [0810.1522].

[26] B. Diemer and A. V. Kravtsov, *Dependence of the Outer Density Profiles of Halos on Their Mass Accretion Rate*, **789** (July, 2014) 1, [1401.1216].

[27] J. F. Navarro, C. S. Frenk and S. D. M. White, *The Structure of Cold Dark Matter Halos*, **462** (May, 1996) 563, [astro-ph/9508025].

[28] J. F. Navarro, C. S. Frenk and S. D. M. White, *A Universal Density Profile from Hierarchical Clustering*, **490** (Dec., 1997) 493–508, [astro-ph/9611107].

[29] D. Merritt, J. F. Navarro, A. Ludlow and A. Jenkins, *A Universal Density Profile for Dark and Luminous Matter?*, *Lett.* **624** (May, 2005) L85–L88, [astro-ph/0502515].

[30] D. Merritt, A. W. Graham, B. Moore, J. Diemand and B. Terzić, *Empirical Models for Dark Matter Halos. I. Nonparametric Construction of Density Profiles and Comparison with Parametric Models*, *Astron. J.* **132** (Dec., 2006) 2685–2700, [astro-ph/0509417].

[31] J. Diemand and M. Kuhlen, *Infall Caustics in Dark Matter Halos?*, *Lett.* **680** (June, 2008) L25–L28, [0804.4185].

[32] M. Vogelsberger, R. Mohayaee and S. D. M. White, *Non-spherical similarity solutions for dark halo formation*, *MNRAS* **414** (July, 2011) 3044–3051, [1007.4195].

[33] A. P. Cooper, D. Martínez-Delgado, J. Helly, C. Frenk, S. Cole, K. Crawford et al., *The Formation of Shell Galaxies Similar to NGC 7600 in the Cold Dark Matter Cosmogony*, *Lett.* **743** (Dec., 2011) L21, [1111.2864].

[34] V. R. Eke, S. Cole and C. S. Frenk, *Cluster evolution as a diagnostic for Omega*, *MNRAS* **282** (Sept., 1996) 263–280, [astro-ph/9601088].

[35] R. N. Henriksen and L. M. Widrow, *Self-Similar Relaxation of Self-Gravitating Collisionless Particles*, *Physical Review Letters* **78** (May, 1997) 3426–3429.

[36] R. N. Henriksen and L. M. Widrow, *Relaxing and virializing a dark matter halo*, *MNRAS* **302** (Jan., 1999) 321–336, [astro-ph/9805277].

[37] K. Riebe, A. M. Partl, H. Enke, J. Forero-Romero, S. Gottlöber, A. Klypin et al., *The MultiDark Database: Release of the Bolshoi and MultiDark cosmological simulations*, *Astronomische Nachrichten* **334** (Aug., 2013) 691–708.

[38] F. Prada, A. A. Klypin, A. J. Cuesta, J. E. Betancort-Rijo and J. Primack, *Halo concentrations in the standard* Λ *cold dark matter cosmology*, *MNRAS* **423** (July, 2012) 3018–3030, [1104.5130].

[39] A. A. Klypin, S. Trujillo-Gomez and J. Primack, *Dark Matter Halos in the Standard Cosmological Model: Results from the Bolshoi Simulation*, **740** (Oct., 2011) 102, [1002.3660].

[40] P. S. Behroozi, R. H. Wechsler and H.-Y. Wu, *The ROCKSTAR Phase-space Temporal Halo Finder and the Velocity Offsets of Cluster Cores*, **762** (Jan., 2013) 109, [1110.4372].

[41] P. S. Behroozi, R. H. Wechsler, H.-Y. Wu, M. T. Busha, A. A. Klypin and J. R. Primack, *Gravitationally Consistent Halo Catalogs and Merger Trees for Precision Cosmology*, **763** (Jan., 2013) 18, [1110.4370].

[42] R. H. Wechsler, J. S. Bullock, J. R. Primack, A. V. Kravtsov and A. Dekel, *Concentrations of Dark Halos from Their Assembly Histories*, **568** (Mar., 2002) 52–70, [astro-ph/0108151].

[43] B. Diemer, S. More and A. V. Kravtsov, *The Pseudo-evolution of Halo Mass*, **766** (Mar., 2013) 25, [1207.0816].

[44] J. M. Bardeen, J. R. Bond, N. Kaiser and A. S. Szalay, *The statistics of peaks of Gaussian random fields*, **304** (May, 1986) 15–61.

[45] S. P. D. Gill, A. Knebe and B. K. Gibson, *The evolution of substructure - III. The outskirts of clusters*, *MNRAS* **356** (Feb., 2005) 1327–1332, [astro-ph/0404427].

[46] A. D. Ludlow, J. F. Navarro, V. Springel, A. Jenkins, C. S. Frenk and A. Helmi, *The Unorthodox Orbits of Substructure Halos*, **692** (Feb., 2009) 931–941, [0801.1127].

[47] D. Anderhalden and J. Diemand, *The total mass of dark matter haloes*, *MNRAS* **414** (July, 2011) 3166–3172, [1102.5736].

[48] A. R. Wetzel, J. L. Tinker, C. Conroy and F. C. v. d. Bosch, *Galaxy evolution near groups and clusters: ejected satellites and the spatial extent of environmental quenching*, *MNRAS* **439** (Apr., 2014) 2687–2700, [1303.7231].

[49] S. Garrison-Kimmel, M. Boylan-Kolchin, J. S. Bullock and K. Lee, *ELVIS: Exploring the Local Volume in Simulations*, *MNRAS* **438** (Mar., 2014) 2578–2596, [1310.6746].

[50] M. Oguri and T. Hamana, *Detailed cluster lensing profiles at large radii and the impact on cluster weak lensing studies*, *MNRAS* **414** (July, 2011) 1851–1861, [1101.0650].

[51] N. Dalal, M. White, J. R. Bond and A. Shirokov, *Halo Assembly Bias in Hierarchical Structure Formation*, **687** (Nov., 2008) 12–21, [arXiv:0803.3453].

[52] E. Lau, D. Nagai and K. Nelson, *On the self-similarity of gas profiles in the outskirts of galaxy clusters*, *in preparation* (2014) .

[53] S. Chandrasekhar, *Brownian Motion, Dynamical Friction, and Stellar Dynamics*, *Reviews of Modern Physics* **21** (July, 1949) 383–388.

[54] J. Binney and S. Tremaine, *Galactic Dynamics: Second Edition*. Princeton University Press, 2008.

[55] H.-Y. Wu, O. Hahn, R. H. Wechsler, P. S. Behroozi and Y.-Y. Mao, *Rhapsody. II. Subhalo Properties and the Impact of Tidal Stripping From a Statistical Sample of Cluster-size Halos*, **767** (Apr., 2013) 23, [1210.6358].

[56] F. C. van den Bosch, F. Jiang, D. Campbell and P. Behroozi, *On the segregation of dark matter substructure*, *MNRAS* **455** (Jan., 2016) 158–177, [1510.01586].

[57] S. More, B. Diemer and A. V. Kravtsov, *The Splashback Radius as a Physical Halo Boundary and the Growth of Halo Mass*, **810** (Sept., 2015) 36, [1504.05591].

[58] U. Seljak, *Analytic model for galaxy and dark matter clustering*, *MNRAS* **318** (Oct., 2000) 203–213, [astro-ph/0001493].

[59] W. Hu and B. Jain, *Joint galaxy-lensing observables and the dark energy*, **70** (Aug., 2004) 043009, [astro-ph/0312395].

[60] A. Klypin, G. Yepes, S. Gottlöber, F. Prada and S. Heß, *MultiDark simulations: the story of dark matter halo concentrations and density profiles*, *MNRAS* **457** (Apr., 2016) 4340–4359.

[61] P. S. Behroozi, R. H. Wechsler and H.-Y. Wu, *The ROCKSTAR Phase-space Temporal Halo Finder and the Velocity Offsets of Cluster Cores*, **762** (Jan., 2013) 109, [1110.4372].

[62] P. S. Behroozi, R. H. Wechsler, H.-Y. Wu, M. T. Busha, A. A. Klypin and J. R. Primack, *Gravitationally Consistent Halo Catalogs and Merger Trees for Precision Cosmology*, **763** (Jan., 2013) 18, [1110.4370].

[63] L. Gao, S. D. M. White, A. Jenkins, F. Stoehr and V. Springel, *The subhalo populations of ΛCDM dark haloes*, *MNRAS* **355** (Dec., 2004) 819–834, [astro-ph/0404589].

[64] A. Faltenbacher and J. Diemand, *Velocity distributions in clusters of galaxies*, *MNRAS* **369** (July, 2006) 1698–1702, [astro-ph/0602197].

[65] E. Contini, G. De Lucia and S. Borgani, *Statistics of substructures in dark matter haloes*, *MNRAS* **420** (Mar., 2012) 2978–2989, [1111.1911].

[66] C. Sifón, M. Cacciato, H. Hoekstra, M. Brouwer, E. van Uitert, M. Viola et al., *The masses of satellites in GAMA galaxy groups from 100 square degrees of KiDS weak lensing data*, *MNRAS* **454** (Dec., 2015) 3938–3951, [1507.00737].

[67] R. Li, H. Shan, J.-P. Kneib, H. Mo, E. Rozo, A. Leauthaud et al., *Measuring subhalo mass in redMaPPer clusters with CFHT Stripe 82 Survey*, *MNRAS* **458** (May, 2016) 2573–2583, [1507.01464].

[68] C. Conroy, R. H. Wechsler and A. V. Kravtsov, *Modeling Luminosity-dependent Galaxy Clustering through Cosmic Time*, **647** (Aug., 2006) 201–214, [astro-ph/0512234].

[69] S. More, H. Miyatake, M. Takada, B. Diemer, A. V. Kravtsov, N. K. Dalal et al., *Detection of the Splashback Radius and Halo Assembly bias of Massive Galaxy Clusters*, *ArXiv e-prints* (Jan., 2016) , [1601.06063].

[70] E. S. Rykoff, E. Rozo, M. T. Busha, C. E. Cunha, A. Finoguenov, A. Evrard et al., *redMaPPer. I. Algorithm and SDSS DR8 Catalog*, **785** (Apr., 2014) 104, [1303.3562].

[71] E. Rozo, E. S. Rykoff, M. Becker, R. M. Reddick and R. H. Wechsler, *redMaPPer - IV. Photometric membership identification of red cluster galaxies with 1 per cent precision*, *MNRAS* **453** (Oct., 2015) 38–52, [1410.1193].

[72] A. Savitzky and M. J. E. Golay, *Smoothing and differentiation of data by simplified least squares procedures*, *Analytical Chemistry* **36** (1964) 1627–1639.

[73] M. Simet, T. McClintock, R. Mandelbaum, E. Rozo, E. Rykoff, E. Sheldon et al., *Weak Lensing Measurement of the Mass–Richness Relation of SDSS redMaPPer Clusters*, *ArXiv e-prints* (Mar., 2016) , [1603.06953].

[74] A. Farahi, A. E. Evrard, E. Rozo, E. S. Rykoff and R. H. Wechsler, *Galaxy Cluster Mass Estimation from Stacked Spectroscopic Analysis*, *ArXiv e-prints* (Jan., 2016) , [1601.05773].

[75] C. Nipoti, L. Ciotti, J. Binney and P. Londrillo, *Dynamical friction in modified Newtonian dynamics*, *MNRAS* **386** (June, 2008) 2194–2198, [0802.1122].

[76] L. Berezhiani and J. Khoury, *A Theory of Dark Matter Superfluidity*, *ArXiv e-prints* (July, 2015) , [1507.01019].

[77] F. Kahlhoefer, K. Schmidt-Hoberg, M. T. Frandsen and S. Sarkar, *Colliding clusters and dark matter self-interactions*, *MNRAS* **437** (Jan., 2014) 2865–2881, [1308.3419].

[78] E. Bertschinger, *Self-similar secondary infall and accretion in an Einstein-de Sitter universe*, **58** (May, 1985) 39–65.

[79] S. Adhikari, N. Dalal and R. T. Chamberlain, *Splashback in accreting dark matter halos*, *Journal of Cosmology and Astroparticle Physics* **11** (Nov., 2014) 019, [1409.4482].

[80] X. Shi, *The outer profile of dark matter haloes: an analytical approach*, *MNRAS* **459** (July, 2016) 3711–3720, [1603.01742].

[81] S. More, H. Miyatake, M. Takada, B. Diemer, A. V. Kravtsov, N. K. Dalal et al., *Detection of the Splashback Radius and Halo Assembly Bias of Massive Galaxy Clusters*, **825** (July, 2016) 39, [1601.06063].

[82] S. Adhikari, N. Dalal and J. Clampitt, *Observing dynamical friction in galaxy clusters*, *Journal of Cosmology and Astroparticle Physics* **7** (July, 2016) 022, [1605.06688].

[83] B. Li, G.-B. Zhao, R. Teyssier and K. Koyama, *ECOSMOG: an Efficient COde for Simulating MOdified Gravity*, *Journal of Cosmology and Astroparticle Physics* **1** (Jan., 2012) 051, [1110.1379].

[84] B. Li, G.-B. Zhao and K. Koyama, *Exploring Vainshtein mechanism on adaptively refined meshes*, *Journal of Cosmology and Astroparticle Physics* **5** (May, 2013) 023, [1303.0008].

[85] V. Springel, *The cosmological simulation code GADGET-2*, *MNRAS* **364** (Dec., 2005) 1105–1134, [astro-ph/0505010].

[86] W. Hu and I. Sawicki, *Models of f(R) cosmic acceleration that evade solar system tests*, **76** (Sept., 2007) 064004, [0705.1158].

[87] G.-B. Zhao, B. Li and K. Koyama, *N-body simulations for f(R) gravity using a self-adaptive particle-mesh code*, **83** (Feb., 2011) 044007, [1011.1257].

[88] M. Rocha, A. Peter, J. Bullock, M. Kaplinghat, S. Garrison-Kimmel, J. Onorbe et al., *Cosmological simulations with self-interacting dark matter*, in *Probes of Dark Matter on Galaxy Scales*, vol. 1, July, 2013.

[89] J. Dubinski and R. G. Carlberg, *The structure of cold dark matter halos*, **378** (Sept., 1991) 496–503.

[90] Y. P. Jing and Y. Suto, *Triaxial Modeling of Halo Density Profiles with High-Resolution N-Body Simulations*, **574** (Aug., 2002) 538–553, [astro-ph/0202064].

[91] B. Allgood, R. A. Flores, J. R. Primack, A. V. Kravtsov, R. H. Wechsler, A. Faltenbacher et al., *The shape of dark matter haloes: dependence on mass, redshift, radius and formation*, *MNRAS* **367** (Apr., 2006) 1781–1796, [astro-ph/0508497].

[92] M. D. Schneider, C. S. Frenk and S. Cole, *The shapes and alignments of dark matter halos*, *Journal of Cosmology and Astroparticle Physics* **5** (May, 2012) 30, [1111.5616].

[93] R. Davé, D. N. Spergel, P. J. Steinhardt and B. D. Wandelt, *Halo Properties in Cosmological Simulations of Self-interacting Cold Dark Matter* , **547** (2001) 574–589.

[94] A. H. G. Peter, M. Rocha, J. S. Bullock and M. Kaplinghat, *Cosmological simulations with self-interacting dark matter - II. Halo shapes versus observations*, *MNRAS* **430** (Mar., 2013) 105–120, [1208.3026].

[95] M. Kaplinghat, R. E. Keeley, T. Linden and H.-B. Yu, *Tying Dark Matter to Baryons with Self-interactions*, *ArXiv e-prints* (Nov., 2013) , [1311.6524].

[96] A. Helmi, *Velocity Trends in the Debris of Sagittarius and the Shape of the Dark Matter Halo of Our Galaxy*, **610** (2004) L97–L100.

[97] D. R. Law and S. R. Majewski, *The Sagittarius Dwarf Galaxy: A Model for Evolution in a Triaxial Milky Way Halo* , **714** (2010) 229–254.

[98] N. Deg and L. Widrow, *The Sagittarius stream and halo triaxiality*, *Monthly Notices of the Royal Astronomical Society* **428** (2013) 912–922.

[99] R. Ibata, G. F. Lewis, N. F. Martin, M. Bellazzini and M. Correnti, *Does the Sagittarius Stream Constrain the Milky Way Halo to be Triaxial?*, *Lett.* **765** (2013) L15.

[100] C. Vera-Ciro and A. Helmi, *Constraints on the Shape of the Milky Way Dark Matter Halo from the Sagittarius Stream* , *Lett.* **773** (2013) L4.

[101] G. van de Ven, J. Falcón-Barroso, R. M. McDermid, M. Cappellari, B. W. Miller and P. T. de Zeeuw, *The Einstein Cross: Constraint on Dark Matter from Stellar Dynamics and Gravitational Lensing*, **719** (Aug., 2010) 1481–1496, [0807.4175].

[102] S. H. Suyu, S. W. Hensel, J. P. McKean, C. D. Fassnacht, T. Treu, A. Halkola et al., *Disentangling Baryons and Dark Matter in the Spiral Gravitational Lens B1933+503*, **750** (May, 2012) 10, [1110.2536].

[103] J. Bailin, C. Power, P. Norberg, D. Zaritsky and B. K. Gibson, *The anisotropic distribution of satellite galaxies*, *MNRAS* **390** (Nov., 2008) 1133–1156, [0706.1350].

[104] E. S. Sheldon, D. E. Johnston, J. A. Frieman, R. Scranton, T. A. McKay, A. J. Connolly et al., *The Galaxy-Mass Correlation Function Measured from Weak Lensing in the Sloan Digital Sky Survey*, *The Astronomical Journal* **127** (May, 2004) 2544–2564, [astro-ph/0312036].

[105] R. Mandelbaum, U. Seljak, R. J. Cool, M. Blanton, C. M. Hirata and J. Brinkmann, *Density profiles of galaxy groups and clusters from SDSS galaxy-galaxy weak lensing*, *MNRAS* **372** (Oct., 2006) 758–776, [astro-ph/0605476].

[106] D. E. Johnston, E. S. Sheldon, R. H. Wechsler, E. Rozo, B. P. Koester, J. A. Frieman et al., *Cross-correlation Weak Lensing of SDSS galaxy Clusters II: Cluster Density Profiles and the Mass–Richness Relation*, *ArXiv e-prints* (Sept., 2007) , [0709.1159].

[107] H. Hoekstra, H. K. C. Yee and M. D. Gladders, *Properties of Galaxy Dark Matter Halos from Weak Lensing* , **606** (2004) 67–77.

[108] R. Mandelbaum, C. M. Hirata, T. Broderick, U. Seljak and J. Brinkmann, *Ellipticity of dark matter haloes with galaxy-galaxy weak lensing*, *Monthly Notices of the Royal Astronomical Society* **370** (2006) 1008–1024.

[109] L. C. Parker, H. Hoekstra, M. J. Hudson, L. van Waerbeke and Y. Mellier, *The Masses and Shapes of Dark Matter Halos from Galaxy-Galaxy Lensing in the CFHT Legacy Survey* , **669** (2007) 21–31.

[110] E. van Uitert, H. Hoekstra, T. Schrabback, D. G. Gilbank, M. D. Gladders and H. K. C. Yee, *Constraints on the shapes of galaxy dark matter haloes from weak gravitational lensing*, *Astronomy and Astrophysics* **545** (2012) .

[111] A. Tenneti, R. Mandelbaum, T. Di Matteo, Y. Feng and N. Khandai, *Galaxy shapes and intrinsic alignments in the MassiveBlack-II simulation*, *MNRAS* **441** (June, 2014) 470–485, [1403.4215].

[112] P. Bett, *Halo shapes from weak lensing: the impact of galaxy-halo misalignment*, *MNRAS* **420** (Mar., 2012) 3303–3323, [1108.3717].

[113] P. J. Howell and T. G. Brainerd, *Galaxy-galaxy lensing by non-spherical haloes - I. Theoretical considerations*, *MNRAS* **407** (Sept., 2010) 891–909, [1004.2491].

[114] P. Simon, P. Schneider and D. Kübler, *Towards an understanding of third-order galaxy-galaxy lensing.*, *Astronomy & Astrophysics/Astronomie et Astrophysique* **548** (2012) .

[115] P. Simon, T. Erben, P. Schneider, C. Heymans, H. Hildebrandt, H. Hoekstra et al., *CFHTLenS: higher order galaxy-mass correlations probed by galaxy-galaxy-galaxy lensing*, *MNRAS* **430** (Apr., 2013) 2476–2498, [1301.1863].

[116] L. Fu, M. Kilbinger, T. Erben, C. Heymans, H. Hildebrandt, H. Hoekstra et al., *CFHTLenS: cosmological constraints from a combination of cosmic shear two-point and three-point correlations*, *MNRAS* **441** (July, 2014) 2725–2743, [1404.5469].

[117] M. Bartelmann and P. Schneider, *Weak gravitational lensing*, *Physics Reports* **340** (2001) 291–472.

[118] P. J. E. Peebles, *Principles of physical cosmology*. Princeton University Press, 1993.

[119] C. Chang, M. Jarvis, B. Jain, S. Kahn, D. Kirkby, A. Connolly et al., *The effective number density of galaxies for weak lensing measurements in the lsst project*, *Monthly Notices of the Royal Astronomical Society* **434** (2013) 2121–2135.

[120] R. A. C. Croft and C. A. Metzler, *Weak-Lensing Surveys and the Intrinsic Correlation of Galaxy Ellipticities*, **545** (Dec., 2000) 561–571, [astro-ph/0005384].

[121] A. Heavens, A. Refregier and C. Heymans, *Intrinsic correlation of galaxy shapes: implications for weak lensing measurements*, *MNRAS* **319** (Dec., 2000) 649–656, [astro-ph/0005269].

[122] R. G. Crittenden, P. Natarajan, U.-L. Pen and T. Theuns, *Spin-induced Galaxy Alignments and Their Implications for Weak-Lensing Measurements*, **559** (Oct., 2001) 552–571, [astro-ph/0009052].

[123] C. M. Hirata and U. Seljak, *Intrinsic alignment-lensing interference as a contaminant of cosmic shear*, **70** (Sept., 2004) 063526, [astro-ph/0406275].

[124] C. M. Hirata, R. Mandelbaum, U. Seljak, J. Guzik, N. Padmanabhan, C. Blake et al., *Galaxy-galaxy weak lensing in the Sloan Digital Sky Survey: intrinsic alignments and shear calibration errors*, *MNRAS* **353** (Sept., 2004) 529–549, [astro-ph/0403255].

[125] R. Mandelbaum, C. M. Hirata, M. Ishak, U. Seljak and J. Brinkmann, *Detection of large-scale intrinsic ellipticity-density correlation from the Sloan Digital Sky Survey and implications for weak lensing surveys*, *MNRAS* **367** (Apr., 2006) 611–626, [astro-ph/0509026].

[126] C. M. Hirata, R. Mandelbaum, M. Ishak, U. Seljak, R. Nichol, K. A. Pimbblet et al., *Intrinsic galaxy alignments from the 2SLAQ and SDSS surveys: luminosity and redshift scalings and implications for weak lensing surveys*, *MNRAS* **381** (Nov., 2007) 1197–1218, [astro-ph/0701671].

[127] J. Blazek, M. McQuinn and U. Seljak, *Testing the tidal alignment model of galaxy intrinsic alignment*, *Journal of Cosmology and Astroparticle Physics* **5** (May, 2011) 10, [1101.4017].

[128] J. Blazek, R. Mandelbaum, U. Seljak and R. Nakajima, *Separating intrinsic alignment and galaxy-galaxy lensing*, *Journal of Cosmology and Astroparticle Physics* **5** (May, 2012) 41, [1204.2264].

[129] M. Jarvis, M. Takada, B. Jain and G. Bernstein, *Weak Lensing Cosmology with LSST: Three-Point Shear Correlations*, in *American Astronomical Society Meeting Abstracts*, vol. 36 of *Bulletin of the American Astronomical Society*, p. 108.17, Dec., 2004.

[130] E. Semboloni, T. Schrabback, L. van Waerbeke, S. Vafaei, J. Hartlap and S. Hilbert, *Weak lensing from space: first cosmological constraints from three-point shear statistics*, *MNRAS* **410** (Jan., 2011) 143–160, [1005.4941].

[131] C. Sánchez, M. C. Kind, H. Lin, R. Miquel, F. Abdalla, A. Amara et al., *Photometric redshift analysis in the dark energy survey science verification data*, *MNRAS* **445** (2014) 1482–1506.

[132] H. Hildebrandt, T. Erben, K. Kuijken, L. van Waerbeke, C. Heymans, J. Coupon et al., *CFHTLenS: improving the quality of photometric redshifts with precision photometry*, *MNRAS* **421** (Apr., 2012) 2355–2367, [1111.4434].

[133] J. Benjamin, L. van Waerbeke, B. Ménard and M. Kilbinger, *Photometric redshifts: estimating their contamination and distribution using clustering information*, *MNRAS* **408** (Oct., 2010) 1168–1180, [1002.2266].

[134] S. Kazantzidis, A. V. Kravtsov, A. R. Zentner, B. Allgood, D. Nagai and B. Moore, *The Effect of Gas Cooling on the Shapes of Dark Matter Halos*, *Lett.* **611** (Aug., 2004) L73–L76, [astro-ph/0405189].

[135] S. E. Bryan, S. T. Kay, A. R. Duffy, J. Schaye, C. Dalla Vecchia and C. M. Booth, *The impact of baryons on the spins and shapes of dark matter haloes*, *MNRAS* **429** (Mar., 2013) 3316–3329, [1207.4555].

[136] T. Baldauf, R. E. Smith, U. Seljak and R. Mandelbaum, *Algorithm for the direct reconstruction of the dark matter correlation function from weak lensing and galaxy clustering*, **81** (Mar., 2010) 063531, [0911.4973].

[137] M. L. Balogh, J. F. Navarro and S. L. Morris, *The origin of star formation gradients in rich galaxy clusters*, *Astrophys. J.* **540** (2000) 113–121, [astro-ph/0004078].

[138] A. Dekel and Y. Birnboim, *Galaxy bimodality due to cold flows and shock heating*, *Monthly Notices of the Royal Astronomical Society* **368** (2006) 2–20.

[139] R. B. Larson, B. M. Tinsley and C. N. Caldwell, *The evolution of disk galaxies and the origin of S0 galaxies*, *Astrophys. J.* **237** (1980) 692–707.

[140] M. G. Abadi, B. Moore and R. G. Bower, *Ram pressure stripping of spiral galaxies in clusters*, *Mon. Not. Roy. Astron. Soc.* **308** (1999) 947–954, [astro-ph/9903436].

[141] A. R. Wetzel, J. L. Tinker, C. Conroy and F. C. van den Bosch, *Galaxy evolution near groups and clusters: ejected satellites and the spatial extent of environmental quenching*, *Mon. Not. Roy. Astron. Soc.* **439** (2014) 2687–2700, [1303.7231].

[142] A. P. Hearin, D. F. Watson, M. R. Becker, R. Reyes, A. A. Berlind and A. R. Zentner, *The dark side of galaxy colour: evidence from new SDSS measurements of galaxy clustering and lensing*, *Mon. Not. Roy. Astron. Soc.* **444** (2014) 729–743, [1310.6747].

[143] E. Baxter, C. Chang, B. Jain, S. Adhikari, N. Dalal, A. Kravtsov et al., *The Halo Boundary of Galaxy Clusters in the SDSS*, 1702.01722.

[144] X. Shi, *The outer profile of dark matter haloes: an analytical approach*, *Mon. Not. Roy. Astron. Soc.* **459** (2016) 3711–3720, [1603.01742].

[145] R. T. Chamberlain, N. Dalal, A. Hearin and P. Ricker, *Probing satellite quenching with galaxy clustering*, *MNRAS* **451** (Aug., 2015) 1496–1501, [1407.2648].

[146] Y. Fang, J. Clampitt, N. Dalal, B. Jain, E. Rozo, J. Moustakas et al., *Tidal stripping as a test of satellite quenching in redMaPPer clusters*, *MNRAS* **463** (Dec., 2016) 1907–1915, [1604.08611].

[147] SDSS collaboration, M. R. Blanton et al., *The Galaxy luminosity function and luminosity density at redshift z = 0.1*, *Astrophys. J.* **592** (2003) 819–838, [astro-ph/0210215].

[148] M. R. Blanton, J. Brinkmann, I. Csabai, M. Doi, D. Eisenstein, M. Fukugita et al., *Estimating fixed frame galaxy magnitudes in the SDSS*, *Astron. J.* **125** (2003) 2348, [astro-ph/0205243].

[149] A. Meert, V. Vikram and M. Bernardi, *Simulations of single and two-component galaxy decompositions for spectroscopically selected galaxies from the Sloan Digital Sky Survey*, *Mon. Not. Roy. Astron. Soc.* **433** (2013) 1344, [1211.6123].

[150] R. Massey et al., *The behaviour of dark matter associated with four bright cluster galaxies in the 10 kpc core of Abell 3827*, *Mon. Not. Roy. Astron. Soc.* **449** (2015) 3393–3406, [1504.03388].